Wide Band Gap Chalcogenide Semiconductors

Rachel Woods-Robinson,[#] Yanbing Han,[#] Hanyu Zhang, Tursun Ablekim, Imran Khan, Kristin A. Persson, and Andriy Zakutayev*

Read Online
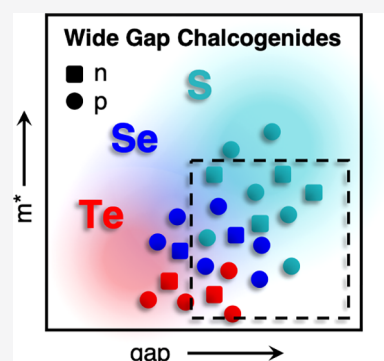
ACCESS | Metrics & More | Article Recommendations | Supporting Information

ABSTRACT: Wide band gap semiconductors are essential for today's electronic devices and energy applications because of their high optical transparency, controllable carrier concentration, and tunable electrical conductivity. The most intensively investigated wide band gap semiconductors are transparent conductive oxides (TCOs), such as tin-doped indium oxide (ITO) and amorphous In−Ga−Zn−O (IGZO), used in displays and solar cells, carbides (e.g., SiC) and nitrides (e.g., GaN) used in power electronics, and emerging halides (e.g., γ-CuI) and 2D electronic materials (e.g., graphene) used in various optoelectronic devices. Compared to these prominent materials families, chalcogen-based (Ch = S, Se, Te) wide band gap semiconductors are less heavily investigated but stand out because of their propensity for p-type doping, high mobilities, high valence band positions (i.e., low ionization potentials), and broad applications in electronic devices such as CdTe solar cells. This manuscript provides a review of wide band gap chalcogenide semiconductors. First, we outline general materials design parameters of high performing transparent semiconductors, as well as the theoretical and experimental underpinnings of the corresponding research methods. We proceed to summarize progress in wide band gap (E_G > 2 eV) chalcogenide materials—namely, II−VI MCh binaries, CuMCh$_2$ chalcopyrites, Cu$_3$MCh$_4$ sulvanites, mixed-anion layered CuMCh(O,F), and 2D materials—and discuss computational predictions of potential new candidates in this family, highlighting their optical and electrical properties. We finally review applications—for example, photovoltaic and photoelectrochemical solar cells, transistors, and light emitting diodes—that employ wide band gap chalcogenides as either an active or passive layer. By examining, categorizing, and discussing prospective directions in wide band gap chalcogenides, this Review aims to inspire continued research on this emerging class of transparent semiconductors and thereby enable future innovations for optoelectronic devices.

CONTENTS

1. INTRODUCTION

Wide band gap (WBG or "wide-gap") semiconductors are critical to various electronic devices, such as transparent contacts, p−n junctions, and thin film transistors.[1] Since the 1950s, oxide wide band gap semiconductors have been intensively investigated, in particular for their contradicting properties of high transparency and high conductivity. The transparent conducting oxide (TCO) Sn-doped In$_2$O$_3$, known as ITO, has been paramount to a variety of commercial devices in the past decades.[2] Possible alternatives, such as F-doped SnO$_2$ (FTO)[3] and Al-doped ZnO (AZO),[4] have been explored in-depth and implemented into commercial devices. In the 21st century, multinary transparent amorphous oxide semiconductors (TAOS), such as indium gallium zinc oxide (IGZO), have also been heavily investigated as channel layers in thin film transistors (TFT) because of their high transparency, high mobility, and good uniformity,[5] leading to their commercial use in liquid crystal displays (LCDs). Although these n-type TCOs show excellent performance, p-type doping and high hole mobilities in oxides has proven much more difficult to achieve in practice. This is due primarily to (1) intrinsic limitations in dispersion that localize the valence band holes and (2) challenges in introducing the holes by p-type doping and minimizing compensating defects. A breakthrough was achieved with the proposed strategy of "chemical modulation of the valence band" (CMVB), using delafossite CuAlO$_2$ as a preliminary example.[6] This approach uses hybridization of O

2p states with metal 3d states at the valence band maximum (VBM), increasing dispersion. Subsequently, the use of this strategy and other approaches has led to a variety of Cu-based p-type TCOs, though optoelectronic properties of p-type TCOs still do not compare with n-type TCOs. Because of these challenges, only a narrow subset of p-type TCO materials have been incorporated into commercial device applications, for example, Cu$_2$O and SnO, which are mainly used in thin film transistors.[7]

Despite the focus of research and device integration on wide-gap oxide materials, transparent semiconductors are not limited to oxides. To date (2020), there are several classes of nonoxide semiconductors that have been experimentally demonstrated to be transparent and conducting. Of interest to this Review, the following group VI chalcogenide (Ch) semiconductors have been investigated: (1) binary II−VI MCh semiconductors (e.g., ZnS,[8] CdS,[9] Zn$_x$Cd$_{1−x}$S[10]), as well as other binary M$_x$Ch$_y$ semiconductors (e.g., SnS$_2$, In$_2$S$_3$, where M = metal); (2) ternary chalcopyrite I−III-Ch$_2$ semiconductors (mostly Cu-based), represented by CuAlS$_2$,[11] and other ternaries (e.g., α-BaCu$_2$S$_2$[12] and Cu$_3$TaS$_4$[13]); (3) multinary layered mixed-anion compounds, such as LaCuOCh,[14] BaCuSF, and CuSCN;[15] and (4) 2D chalcogenides, such as MoS$_2$, including both binary and ternary materials. Additionally, significant research has been done on wide band gap semiconductors (also called WBG semiconductors or WBGSs) with anions from groups IV (e.g., graphene,[16] and carbon nanotubes,[17] SiC[18]), V (e.g., GaN,[19,20] zinc nitrides[21]), and VII (e.g., CuI[22]), which are not discussed here. A network diagram schematic of these material classes is depicted in Figure 1, with chalcogenides highlighted in red. Many review papers and book chapters address various aspects of this broad field of WBG semiconductors. Some examine oxide TCOs, focusing on intrinsic material properties,[23,24] while others highlight applications, such as transparent electronics,[1] TFTs,[7] and photovoltaics.[25] Others summarize nitrides,[26] halides,[22] and carbides,[27] including graphene.[28] A few reviews have briefly mentioned wide-gap chalcogenide semiconductors, but limit their focus to oxides or a narrow subset of chalcogenides.[29] Thus, here we focus on these wide band gap chalcogenides, referring to chalcogen anions as Ch (with Ch = S, Se, Te) and not including O for the purposes of this Review.

As is evident from the literature, wide band gap chalcogenide semiconductors present several distinctions in comparison to oxide counterparts, with particular advantages for optoelectronic applications and as p-type semiconductors. The covalency of a metal−VI (M−VI) bond tends to increase going down group VI, leading to larger orbital overlaps and lower hole effective masses. Thus, heavier chalcogenides have higher-lying p orbitals (S 3p, Se 4p, Te 5p) that can hybridize with M (e.g., Cu 3d) to form more disperse, delocalized valence bands than in oxides.[6] This can result in higher achievable mobilities in p-type chalcogenides, for example, up to 20 cm^2 V$^{−1}$ s$^{−1}$ for Cu-based compounds,[12,30,31] compared to <1 cm^2 V$^{−1}$ s$^{−1}$ for Cu-based p-type wide-gap oxides (with some exceptions,[32] up to 10 cm^2 V$^{−1}$ s$^{−1}$ in single crystal CuAlO$_2$). However, the band gap E_G (and optical transparency window) tends to be smaller for chalcogenides than for oxides, though this is not always the case (e.g., ZnS has a wider gap than ZnO, see section 3). There is also evidence that chalcogenides are easier to be doped p-type than oxides because of their higher-lying p-derived valence bands and smaller ionization energies, a postulated design principle for high p-type doping.[33] Additionally, weaker M−Ch bonds compared to M−O bonds in these materials allow for ease
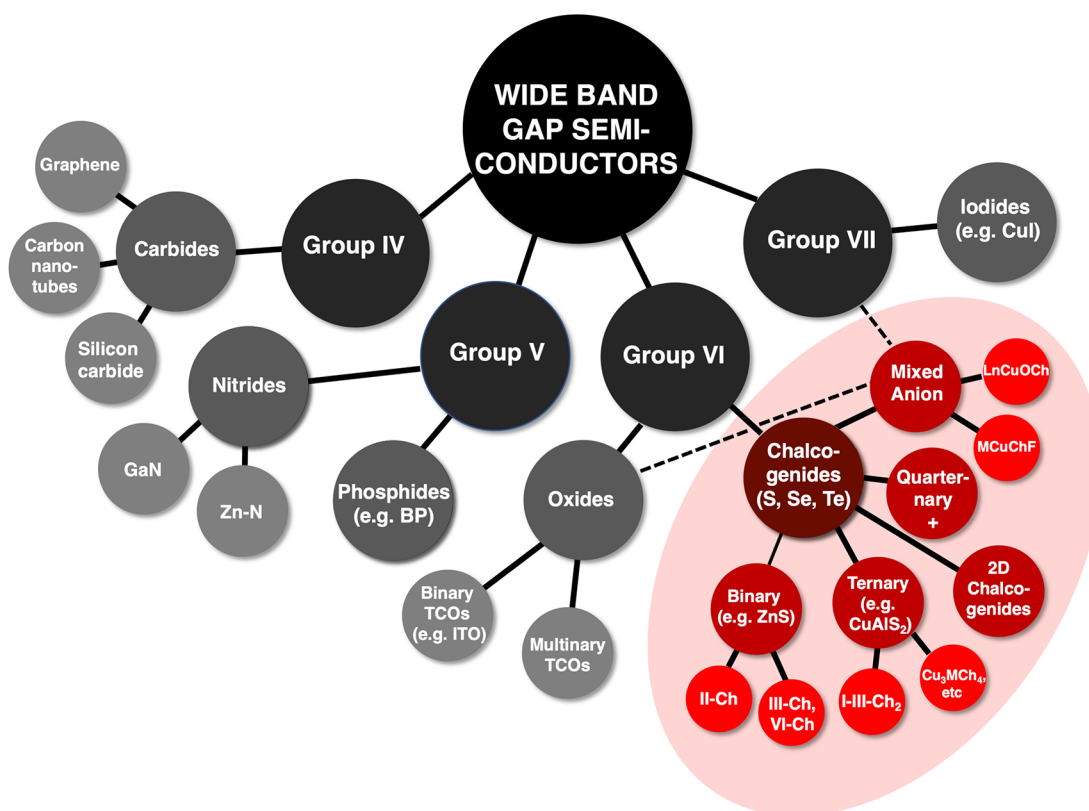
Figure 1. Schematic network diagram depicting various material classes of wide band gap semiconductors. Classes are sorted by anion group. Chalcogenide wide-gap semiconductors, which are the focus of this review article, are highlighted in red (with Ch = S, Se, Te).

of synthesis but may lead to increased degradation and stability concerns in chalcogenides. We note fewer stable chalcogenides exist in nature and in the experimental literature than oxides (see below), partially due to decomposition tendencies in air and water, but this implies that there are likely many unexplored chalcogenides. Considering these factors, it is of value to review wide-gap chalcogenide semiconductors.

To further demonstrate the need for this investigation, Figure 2a displays the extent to which the material space of wide band gap chalcogenides is underexplored by plotting the distribution of computed band gaps for all known thermodynamically stable oxides and chalcogenides in the Materials Project database.[34] Most of these materials correspond to experimentally synthesized compounds from the Inorganic Crystal Structure Database (ICSD).[35,36] We show all compounds with predicted gaps greater than 1 eV to represent wide-gap semiconductors, because density functional theory (DFT) tends to *underestimate* band gap by a factor of 1−2 with GGA and GGA+U functionals,[37] unless U is empirically fit to recreate the experimental gap (see section 2.2.1).[38] The resulting plot shows a similar statistical distribution, but for about 1.5 times more oxides (∼15 456) than chalcogenides (∼10 611), which are further subdivide into 3367 sulfides, 2330 selenides, and 1767 tellurides (see Figure 2b). This can be, in part, attributed to the generally tendency of oxides to be more stable and earth abundant, which is why so many have been discovered in nature or realized synthetically. However, recent research confirms synthesis of many new computationally predicted compounds unlikely to occur in nature, for example, in the space of ternary nitrides,[39,40] suggesting possible realization of many new chalcogenides with chemical compositions and stoichiometries that have never been synthesized (and thus are missing from

Figure 2). Moreover, many computationally "metastable" structures can be stabilized through techniques, such as heterostructural alloying.[41] Thus, exciting and challenging research lies ahead to uncover new wide band gap chalcogenide materials with potential uses in energy applications and beyond.

In this Review, following the introduction (section 1), we highlight the functional materials properties of interest in wide band gap chalcogenide semiconductors (section 2) and discuss computational and experimental methods to calculate, synthesize, characterize, and optimize such materials. Next, we discuss the prominent classes of chalcogenide semiconductors classified by cations, stoichiometry, and crystal structure (section 3), as shown in red in Figure 1. We highlight materials that have been realized experimentally (Tables 1−3) and identify promising theoretical predictions (Table 4) to inform and inspire continued research in this field. Lastly, we summarize the most prominent applications of wide-gap chalcogenide semiconductors in electronic devices (section 4), and discuss new potential device architectures. Since there is no clear boundary between transparent and nontransparent, we define "wide band gap semiconductors" for the purposes of this Review as semiconductors whose band-to-band absorption edge appears larger than 2 eV (wavelengths less than 620 nm). Among wide band gap chalcogenide semiconductors, we focus on electronic n- or p-type dopable materials, which excludes highly insulating and amorphous chalcogenides, as well as energy storage and nanogenerator applications of chalcogenides from this review, referring the reader elsewhere.[42,43] Because of the multidisciplinary nature of these materials, this Review is intended for a wide audience, from computational scientists to experimental materials scientists to engineers focusing on particular optoelectronic technologies. Thus, we have tailored
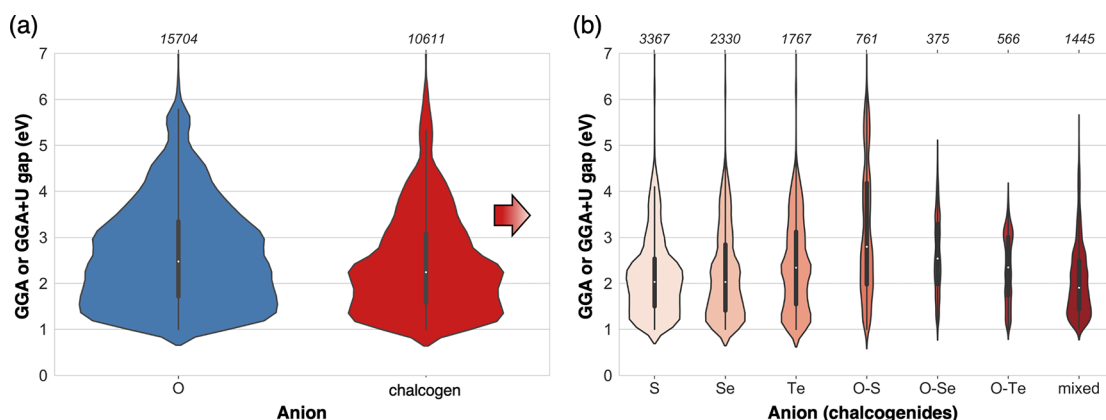
Figure 2. (a) Violin plot of the smoothed distribution of computed GGA or GGA+U band gaps within all known oxide materials (blue) and within all chalcogenide and mixed chalcogenides (red). (b) Chalcogenides and mixed chalcogenides are further categorized by anion type, with "mixed" referring to any mixed-anion chalcogenide. Data is only plotted for materials with band gaps greater than 1 eV. Note that the GGA+U functional significantly underestimates the band gap, so this is a reasonable cutoff for materials screening of wide-gap chalcogenides ($E_G > 2$ eV in this Review). Violin plots are binned by count, and all data is from the open source Materials Project database.[34] We note that some of the mixed-anion compounds listed may in fact have a chalcogenide *cation* rather than anion (e.g., sulfates).

each section to be either read independently or together as a comprehensive review.

2. MATERIALS PROPERTIES AND RESEARCH METHODS

The primary requirements of functional wide band gap chalcogenide semiconductors discussed in this text differ by application, but most share four basic criteria: (1) synthesizability and thermochemical stability, (2) a wide enough band gap to ensure transparency to light of a particular wavelength range, (3) high enough mobility to enable optoelectronic device integration, and (4) n- or p-dopability to ensure a sufficient concentration of charge carriers. Here, we discuss both the theoretical and experimental considerations of each of these properties, which are pertinent to designing high performance wide-gap chalcogenide materials. We will focus on properties relevant to photovoltaics and transparent electronics, since they are desirable and rare, though we also mention properties important in other applications such as photocathodes for solar water splitting and light emitting diodes (LEDs) (see section 4). We also provide evidence why chalcogenides in particular could be an important, underexplored chemical space to look for materials with these properties, and we highlight some unique challenges of chalcogenide materials.

Up until recently, material candidates were selected for synthesis based primarily on chemical intuition and theoretical approximations. Historically, it was easier to grow materials one-by-one and measure their conductivities and transparencies than to perform expensive ab initio computation to estimate such properties, so most experimental materials in section 3 were developed in this manner. Recent advances in high-performance computing and efforts, such as the Materials Genome Initiative (MGI), have driven development of computational platforms, such as the Materials Project,[34] AFLOWLIB,[44] NREL-MatDB,[45−47] and Open Quantum Materials Database,[48] that compile data from density functional theory (DFT) calculations and allow facile exploration and screening of material candidates for desired properties. This accessibility of data has fundamentally changed how experimental materials scientists select candidate materials for synthesis. In section 3, we will discuss some key findings from ab initio computational screenings of

wide-gap chalcogenides using the properties and descriptors discussed here.

Computational materials screenings often make use of a "funnel" approach to filter out materials of particular interest, depicted by Figure 3a. Usually the more computationally "inexpensive" steps are performed first and are followed by more in-depth steps that require more computer resources. In some studies "inputs" are drawn from materials property databases, while others calculate novel classes of compounds that have never been synthesized (e.g., via substitutions, random structure searches, or machine learning). As shown, a screening methodology typically requires (1) an initially data subset in a selected range of stoichiometries or structures (e.g., inorganic metal chalcogenides), (2) a proxy for thermodynamic stability, and then (3) a series of descriptors calculated from the electronic band structure or other methods to estimate a property of interest (e.g., effective mass to estimate mobility). Experimental materials discovery is illustrated by an analogous "experimental funnel" in Figure 3b. This process starts with synthesis of material candidates sometimes from the computational funnel (Figure 3a), and then, a series of characterization experiments are performed to measure composition, structure, and various properties, with an end goal often to incorporate the characterized material into a device. We will discuss the "rungs" of the computational and experimental funnels next, some outputs in section 3, and possible device applications in section 4.

2.1. Synthesizability and Stability

2.1.1. Thermodynamic Stability Calculations. A wide-gap chalcogenide material must be both synthesizable and stable to be useful for device applications. A first-order computational descriptor for synthesizability is estimated by comparing formation energies of compounds within the same compositional space and by investigating their degradation pathways. Shown in Figure 4a, a first-order computational descriptor for synthesizability, "energy above the convex hull" (E_{hull}). For a given compound, for example, AB$_2$ polymorph β_4, E_{hull} measures how far β_4's formation energy (ΔG_f) is from a convex hull described by the thermodynamic ground states within compositional space, for example, A−B. An E_{hull} of 0 meV/atom indicates a ground state, and correlates strongly with a high probability of
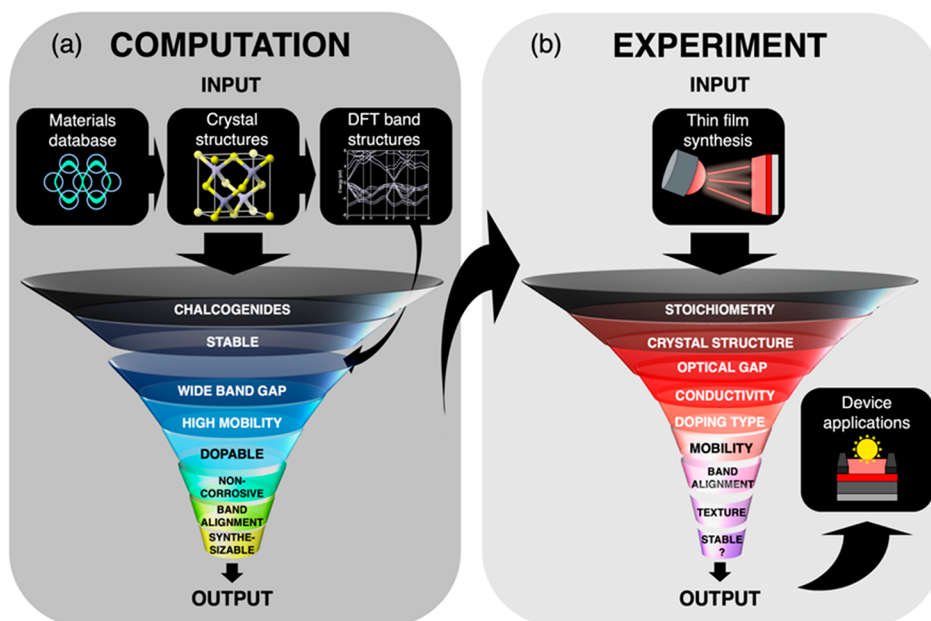
Figure 3. (a) Computational and (b) experimental screening funnels to search for desirable properties of wide-gap semiconductors within a computational materials database and using experimental methods. The computational figure in panel a is adapted with permission from ref 49. Copyright 2018 American Chemical Society.

synthesizability. An E_{hull} < 0.03 eV/atom is usually considered "stable" for oxides (within thermal energy kT), and "metastable" compounds tend to lie in the range E_{hull} < 0.1 eV/atom,[49] though it is not established whether chalcogenides conform to these limits.[50] An upper E_{hull} limit of synthesizability has recently been hypothesized by an amorphous "synthesizability skyline", and the skyline of chalcogenides was found to be significantly higher than that of oxides.[51] This suggests that thermodynamically metastable polymorphs may be more achievable for chalcogenides than for oxides, which is a significant advantage for the number of possible materials that can be studied.

The E_{hull} assessment can be applied early in a screening because it is usually computationally inexpensive. It does not require band structure calculations, only a DFT structure relaxation and cross comparison to other structures within a database. However, assessing stability and synthesizability by thermodynamics alone does not tell the full story. One issue chalcogenides face more than oxides is their stability in air and aqueous environments. Sulfides and selenides in general are more likely to oxidize and decompose under standard conditions than oxides, due to low energy reaction pathways with water or water vapor to form H_2S or H_2Se, though this is not universally true and can be studied computationally for particular compounds of interest. For example, screenings for photoelectrochemical materials have used calculations of Pourbaix diagrams to assess the stability of a compound.[52,53] Additionally, p-type dopants must be stable within a host compound. For example, there have been several attempts of doping ZnO p-type with N and In/Ni, but these materials have later been shown to be unstable over time due to compensating donor defects.[54,55] It is also important to note that computationally promising "synthesizable" and "stable" materials still may not be possible to achieve in practice due to competing reactions, various decomposition pathways, degassing, or uncertainties in calculations, among other reasons.

2.1.2. Experimental Synthesis, Phase Analysis. One of the best ways to determine synthesizability and stability of a

given material system is to *synthesize* it, but this is not necessarily straightforward. There is a huge variety of bulk and thin film growth techniques and numerous interconnected parameters to optimize in synthesis and postprocessing, as covered in many texts.[56−60] Wide band gap semiconductors can be made in forms of bulk, thin film, 2D, or even quantum dots. Thin films are usually the most useful form for electronic device applications, and will be the focus in this Review. Thin film transparent chalcogenides have been synthesized by (1) physical vapor deposition (PVD),[61] including sputtering,[62] pulsed laser deposition (PLD),[63] and thermal or electron-beam evaporation,[64,65] molecular beam epitaxy (MBE),[66,67] by (2) chemical vapor deposition, usually involving some reactions between precursors, such as atomic layer deposition (ALD),[68,69] metal organic chemical vapor deposition (MOCVD),[70] and plasma-enhanced chemical vapor deposition (PECVD),[71] or by (3) solution processes, including spray pyrolysis,[72] sol−gel,[73,74] and chemical bath deposition (CBD).[75] Postdeposition treatments can be applied to enhance crystallinity or introduce dopants, such as exposure to gas (e.g., sulfurization and selenization, common in chalcopyrite materials)[76] and rapid thermal annealing,[77] and films can be doped via ion implantation or diffusion. Synthesis methods for bulk semiconductors varies, spanning a wide range of material quality, including solid-state reactions, spark plasma sintering,[11] floating zone synthesis,[78] growth from melt techniques, for example, Czochralski and Bridgman growth,[79,80] etc. To achieve semiconducting materials in layer-controlled 2D forms, the two major directions are top-down methods, that is, exfoliating materials from their bulk counterparts and bottom-up methods, that is, direct synthesis of 2D materials from constituent elements or precursors (see section 3.6 for examples).[81] After synthesis, stoichiometry and elemental uniformity can be determined by X-ray fluorescence (XRF), Rutherford backscattering spectroscopy (RBS), X-ray photoelectron spectroscopy (XPS, limited to surface stoichiometry), energy dispersive X-ray spectroscopy (EDS or EDX), among other techniques. Sometimes off-stoichiometric syn-
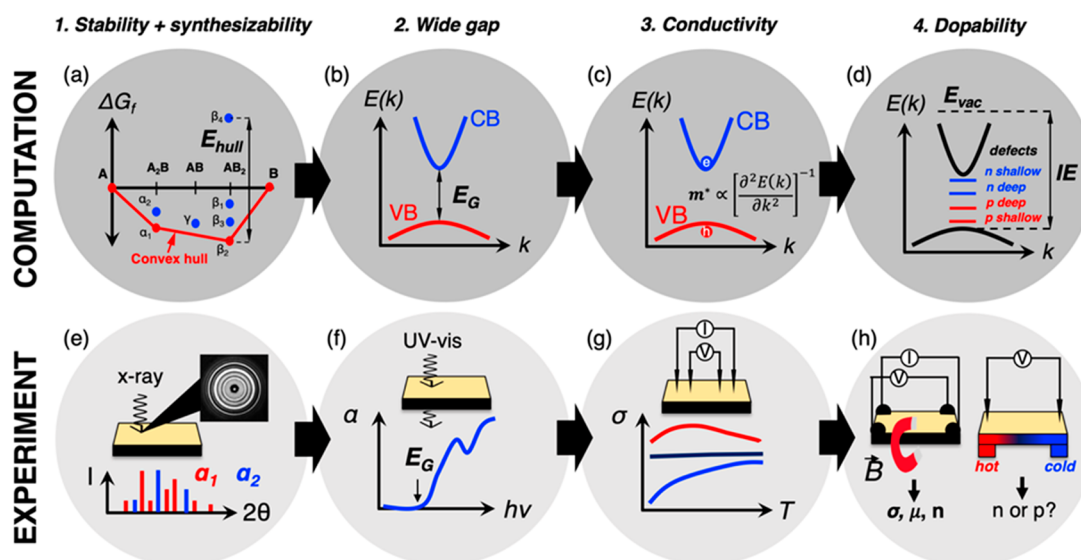
Figure 4. Schematic representations of the four computational descriptors highlighted in the text: (a) energy above the convex hull E_{hull} as a descriptor for thermodynamic stability, (b) band gap E_G as a descriptor for transparency, (c) effective mass m^* as a descriptor for mobility, and (d) defect levels and ionization energy (IE) as descriptors for dopability. The corresponding experimental properties and tools are (e) crystal structure and phase stability measured by X-ray diffraction, (f) absorption and optical band gap using UV−vis spectrophotometry, (g) conductivity σ (temperature-dependent σ shown here) using a four-point probe, and (h) quantification of mobility μ, carrier concentration n, and carrier type using the Hall measurement (left) and a Seebeck measurement (right). Details are described in the text.

thesis is useful for achieving targeting properties and high conductivity.

Achieving the right stoichiometry of chemical elements does not guarantee that a crystal phase of interest has been made. Many of the low temperature growth techniques result in amorphous or nanocrystalline material, which has to be treated for crystallization. X-ray diffraction (XRD) techniques are often used to confirm whether a targeted crystal phase has been synthesized.[82] Measured diffraction peaks can be compared to standard reference patterns, which can be experimentally or computationally generated. Secondary phases may be present, but not visible with diffraction. Sometimes nanocrystalline phases can be detected by electron diffraction or Raman spectroscopy, among other methods, but Raman reference patterns for new materials are not as easily accessible. A cartoon schematic of XRD experiments is shown in Figure 4e.

Additional constraints exist when synthesizing chalcogenide materials for device applications, as discussed earlier. Most importantly, materials need to be stable in air and at the interface of relevant chemicals they are grown upon or below in a device stack or exposed to during their lifecycle. To this end, it is useful to measure material properties after exposure in the air for a given time interval. Additional constraints include temperature stability (most devices have a "thermal budget"), stability to UV irradiation (for devices that will operate in the sun), Pourbaix stability (e.g., in PEC device applications, where materials are often exposed to extremely acidic or basic conditions), etc. It is also important to consider the lifetime of the device when designing materials to be incorporated, that is, whether migration of dopants or segregation into secondary phases will occur over time. End-of-life decomposition and recyclability of materials is also becoming increasingly important in rational materials design, as researchers strive to implement principles of the circular economy.[83]

2.2. Band Gap

2.2.1. Computational Optical Properties. A material with a band gap E_G higher than approximately 3.1 eV (corresponding to a band absorption onset at 400 nm), is typically considered "transparent" so long as other effects are negligible (e.g., free carrier absorption and defect absorption; see below). In this Review, we will also be discussing semitransparent materials with band gaps greater than 2 eV (band absorption onset at 620 nm); hence, the term "wide band gap semiconductors". Band gap and dominant band-to-band absorption can be estimated from electronic structure calculations from ground state density functional theory (DFT), as shown schematically in Figure 4b as the lowest energy difference between the conduction band minimum (CBM) and the valence band maximum (VBM). Different DFT functionals trade off band gap accuracy for computational efficiency. Fast, "cheap" DFT calculations using, for example, GGA and GGA+U have been performed and compiled for tens of thousands of experimentally known materials in computational databases (e.g., Materials Project[34]) but have been shown to significantly underestimate band gaps unless the U value is empirically fit to band gap. More expensive calculations such as hybrid functionals (e.g., HSE06) and GW can also be applied in a lower-throughput manner at a greater computational cost. These computational methods have been benchmarked to predict band gaps on a case-by-case basis within 25% uncertainty[84] and are available in limited quantities (∼1000) in some computational databases (e.g., NRELMatDB[45−47]). In general oxides tend to exhibit a wider gap than counterpart chalcogenides (see section 1), but as shown in Figure 3, there are still many chalcogenides with wide band gaps. We note that a wide band gap alone does not necessarily guarantee optical transparency. Dominant transitions tend to occur at direct gaps, rather than indirect gaps that require phonon assistance for absorption. At high carrier doping, intraband scattering and free carrier absorption can cause loss of transparency within the near-
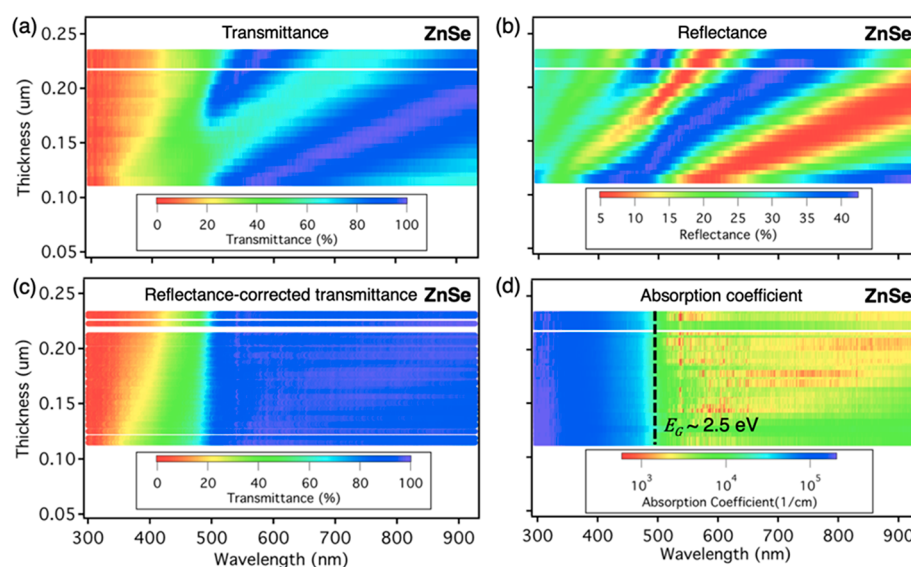
Figure 5. Optical properties of sputtered ZnSe thin films as a function of thickness: (a) transmittance, (b) reflectance, (c) reflectance-corrected transmittance, and (d) absorption coefficient, indicating how optical band gap E_G is estimated experimentally.

infrared and visible spectrum that increases with doping concentration. Additionally, dopants can introduce defect levels within the gap that reduce optical transparency, and in some materials, excitonic absorption may also become significant.[85] These effects are trickier to predict computationally.

2.2.2. Experimental Optical Properties. Optical properties of transmittance, reflectance and absorption are typically measured for thin films with UV−vis−IR spectrophotometry as a function of wavelength, as depicted in Figure 4f. Transmittance and reflectance measurements can be used to calculate the absorption coefficient, $\alpha = -\ln\left(\frac{T}{1-R}\right)/d$, as a function of wavelength. From the absorption spectrum, the low-frequency cutoff is typically fit to estimate the band gap using the Tauc relation $(\alpha h\nu)^{1/r}$, where $r = 1/2$ is assumed for allowed direct transitions and $r = 2$ is assumed for allowed indirect transitions. Such fits are often ambiguous depending on the selected energy range, which is not standardized and depends on the discretion of the researcher. Band-to-band transitions typically occur in semiconductors for absorption coefficients of approximately 10^4 cm^{-1}, so the cutoff is usually drawn around this value as an alternative method to estimate the optical absorption threshold without asserting the band gap. Thus, it can be very difficult to conclusively determine from Tauc plots whether a material has a direct or indirect band gap and to accurately estimate indirect band gap for which the optical transition probability is usually low. In addition, researchers should be aware that transmittance and reflectance are *thickness dependent* measurements, leading to different accessible dynamic ranges of absorption coefficient measurements. It is important to keep this in mind when interpreting Tauc-derived experimental band gaps and comparing reported values for samples with very different thicknesses.

To illustrate some of these discrepancies, Figure 5 shows the optical properties of sputtered zincblende ZnSe thin films, plotted as a function of film thickness. As evidenced from Figure 5a and b, transmittance values are a function of wavelength and are heavily influenced by Fabry−Perot interference fringes related to light scattering from the front and back of the film. Thus, it is ambiguous to report transmittance from a single wavelength number, yet this is still done routinely in the

literature. One way to solve this issue is to use the reflectance-corrected transmittance, $T_{corr} = \frac{T}{1-R}$, as shown in Figure 5c. For a given thickness, this mathematical transformation results in a monotonically increasing T_{corr} with wavelength, and thus a more reliable value. However, even T_{corr} still depends somewhat on film thickness (Figure 5c), so thin films will appear "transparent" if thin enough. Considering these two factors, transmittance can be useful as a reference but is not an appropriate metric to compare various materials systems. Instead, it is recommended to report the α to avoid thickness and wavelength dependence. Figure 5d shows the absorption coefficients as a function of wavelength and thickness. In this case there is a fixed onset at ∼490 nm where absorption reaches 10^4 cm^{-1} regardless of thickness, so we can interpret this value as a band gap of ∼2.5 eV (compared to the literature reported gap of ∼2.7 eV).[120]

Spectrophotometers can also be equipped with an integrating sphere to measure diffuse reflectance for rough samples. Other useful optical characterization techniques include Fourier transform infrared spectroscopy (FTIR) to probe the infrared and ellipsometry to extract optical constants (i.e., refractive index n and extinction coefficient k), and there are many in-depth reviews and textbooks on these methods.[86−88] In this Review, we will focus on reporting optical band gap because it is the standard value reported consistently in the literature, yet we will often use the "∼" symbol to emphasize aforementioned experimental and analytical uncertainties. We also provide references that report absorption coefficient, transmittance, roughness, and other optical properties.

2.3. Mobility and Conductivity

The carrier mobility μ of a material is set by the intrinsic dispersion of the electronic bands as quantified by effective mass m^* and is limited by the mean free path of carriers with charge q (or the inverse of mean free path, scattering time τ), such that

$$\mu = \frac{q\tau}{m^*} \tag{1}$$

while electrical conductivity is proportional to both the carrier mobility and the carrier concentration n

$$\sigma = qn\mu = \frac{q^2 n\tau}{m^*} \tag{2}$$

2.3.1. Effective Mass and Scattering Time. Conductivity can be estimated from DFT electronic band structures by first considering effective mass m^* (electron effective mass m_e^* for n-type conductivity and hole effective mass m_h^* for p-type conductivity). There are generally two types of effective mass reported in the literature. The first, density of states effective mass m_{DOS}^*, is estimated by integrating the entire density of states near the band edge and assuming nondegenerate doping. The second, band effective mass (or inertial effective mass) m_b^* is band structure dependent and accounts for band anisotropy and degeneracies. This value is generally used for transport calculations, so we will refer to it herein. From band theory, the band effective mass is defined as the second partial derivative of band energy with respect to crystal momentum and is represented by the effective mass tensor m_{ij}^*

$$m_{ij}^* = \left[\frac{1}{\hbar^2} \frac{\partial^2 E}{\partial k_i \partial k_j} \right]^{-1} \tag{3}$$

Diagonalizing and inverting this tensor results in an effective mass for three perpendicular directions in the crystal, and in an isotropic crystal it is a scalar value, m^*.[89] Effective mass has units of electron mass m_0 but is often simplified as m^*/m_0, such that it is unitless, a convention that is adopted in this Review. This value depends on the orbitals present at the band edges and their degree of splitting and hybridization. It usually ranges from 0.1−10 for electrons and holes in semiconductors, though the exact value of m^* differs by application, how it is defined (e.g., number of bands included in the calculation, and Fermi level position), and particular calculation method. Computational codes, such as BoltzTraP[90] and EMC,[91] are available for calculation of m^* for large data sets. Because of the tighter binding of valence band states compared to conduction band states, wide-gap materials tend to have much lower m_e^* than m_h^*, allowing for higher n-type conductivity to be achieved.[92] This is depicted in Figure 4c, where the CBM is far more disperse than the VBM. In most wide-gap oxides, low valence state dispersion is due to highly localized O 2p orbitals lying at or near the VBM and introduces a fundamental limitation to achieving high p-type mobility. This limitation is one reason for exploring chalcogenides, which exhibit more delocalized VBM orbitals and hence may be advantageous over oxides in achieving wide-gap semiconductors with low hole effective mass and high mobility (see section 1).

Scattering time τ is much more difficult to calculate from ab initio methods, and differs drastically by material. It is typically decomposed into various scattering components

$$\frac{1}{\tau} = \frac{1}{\tau_i} + \frac{1}{\tau_g} + \frac{1}{\tau_l} + \frac{1}{\tau_n} \tag{4}$$

where τ_i is ionized impurity scattering (i.e., off of charged dopant ions), τ_g is grain boundary scattering (i.e., off of crystal grains or dislocation defects), τ_l is lattice vibration scattering (i.e., off of phonons or polarons), and τ_n is neutral impurity scattering (i.e., off of uncharged dopants or defects). These carrier scattering mechanisms depend not just on crystal structure but on processing conditions, crystal purity, doping levels, among other conditions, and are covered in detail elsewhere.[93−95] When transparent semiconductors are degenerately doped to concentrations approximately $>10^{20}$ cm^{-3}, it is typical for

temperature-independent ionized impurity scattering to dominate.[96,97] Most computational screening studies assume ionized impurity scattering dominates in wide-gap chalcogenides, such that the constant relaxation time approximation (cRTA) holds. However, computational methods and associated software packages, such as the aMoBT code,[98] to consider other scattering effects in the calculation of mobility are advancing, as well as semiempirical methods, such as the β_{SE} descriptor.[99] We note that the thresholds for "high" mobility and conductivity are arbitrary and requirements will differ by application.

2.3.2. Mobility or Conductivity Measurements. Figure 4g and 4h demonstrate the two most common ways to measure electrical conductivity in thin film materials. In the first configuration in Figure 4g, a four-point probe is used to measure sheet resistance of bulk or thin film semiconductors, and in-plane conductivity can be calculated if film thickness known. The basic concept is to source current through two terminals while generating and measuring voltage from the other two terminals. Vertical or out-of-plane resistivity can be measured by preparing a sandwich structure with conductive materials as top/bottom electrodes and target material in the middle, and measuring its electrical resistance, also requiring independent thickness measurements to extract electrical conductivity.

Hall effect measurements shown on the left of Figure 4h are often used to obtain Hall mobilities and carrier concentrations (as well as carrier type). When a source current flows through two terminals, carriers deviate under a vertical magnetic field and accumulate at the edges, generating a Hall voltage proportional to carrier concentrations. Mobility can then be back-calculated from conductivity and carrier concentrations, and carrier type is indicated from the sign of the Hall voltage. The measured mobility typically consists of multiple scattering mechanisms, and τ can be back-calculated using eq 1 if m^* is known. To reveal the particular scattering mechanism for a thin film, the Hall mobility can be measured as a function of temperature. For example, a temperature-dependent mobility suggests phonon scattering, whereas temperature independent mobility is usually indicative that ionized impurity scattering dominates. This latter case is a typical dominant scattering mechanism in highly conductive n-type transparent conducting oxides and is also present in several transparent conducting sulfides.

Conductivity can also be measured optically, using light to excite free carriers. This is particularly useful to evaluate intragrain mobility and for bulk powder samples which cannot be analyzed with four-point probe or Hall setups due to their granularity. This method relies on the optical absorption at photon energies below the energy gap, which is related to the free electrons or holes. The relationship is summarized by considering carriers as free electrons from the Drude model, from which conductivity, mobility, carrier concentration can be calculated if m^* is known.[100] Mobility can also be backed out from device measurements (e.g., in transistors), as is described for 2D chalcogenides in section 3.6.

2.4. Dopability

In addition to low m^* and high τ, eq 1 illustrates that high conductivity also requires a sufficiently high carrier concentration n_n for electrons (or n_p for holes). This depends on the material's dopability, which is a function of several parameters. For example, to be a highly conductive wide-gap p-type semiconductor, a material must support the introduction of p-type dopants (i.e., dopant must be soluble and energetically

stable), be dopable to a high enough concentration, and not be susceptible to compensation by n-type "hole killer" defects. It has been theorized that n-type dopability is favorable in materials with large electron affinities, while p-type dopability is favorable in materials with small ionization energies.[33] This is one reason why it is more difficult to dope wide-gap materials; in general as the gap increases, the CBM shifts toward vacuum level and the VBM shifts away from it. Additionally, the wider the gap the more likely defect levels are to emerge within the gap and induce carrier compensation. Because of the 3p, 4p, or 5p character of chalcogen atoms, valence levels of chalcogenides tend to lie closer to vacuum than oxides with 2p character of oxygen atoms, suggestive of a higher propensity for p-type doping in chalcogenides compared to oxides. However, while noting this general trend, many chalcogenides are in fact highly n-type dopable as well, and defect calculations, are usually necessary to understand dopability.

2.4.1. Computational Dopability.

Computationally understanding defect compensation and selecting appropriate dopants requires defect formation energy calculations, which require large DFT supercells and thus are computationally quite expensive. These calculations can estimate the energy level of particular dopants, whether they are shallow or deep, and whether they should lead to n-type or p-type conductivity (see Figure 4d). The defect formation energy, $E^f[X^q]$, is the energy cost to create or remove an isolated defect X with charge state q from a bulk material, and describes how favorable various defects and dopants are to form compared to one another. It is calculated as

$$E^f[X^q] = E_{\text{tot}}[X^q] - E_{\text{tot}}[\text{bulk}] - \sum_i n_i\mu_i + qE_{\text{F}} + E_{\text{corr}}$$

(5)

where $E_{\text{tot}}[X^q]$ and $E_{\text{tot}}[\text{bulk}]$ are DFT formation energies of defective and bulk supercells, $-\sum_i n_i\mu_i$ is the summation over chemical potentials of the defect elements, and qE_{F} is the cost in energy of adding or removing an electron (E_{F} is the Fermi level). E_{corr} are correction terms that account for mirroring of charges, VBM alignment, and other spurious computational effects. The calculated formation energies can be used as inputs to thermodynamic simulations that output equilibrium defect concentration, carrier densities, and Fermi level positions for an assumed set of chemical potentials. Specifics of these defect calculations and thermodynamic simulations are covered in comprehensive reviews.[101,102] Recently, codes such as PyCDT and Pylada have been developed to run defect calculations on a high throughput framework, making them more accessible to the research community.[103,104] Defect calculations can also be used to screen for defect tolerance[105−107] and for deep-level defect induced absorption that would decrease optical transparency.[108]

To roughly assess dopability, some high throughput studies have calculated the branch point energy (BPE, also referred to as Fermi level stabilization energy or charge neutrality level), which approximates the position where the Fermi level E_{F} is pinned when defects are introduced.[109] The BPE is calculated using the following formula:[110]

$$\text{BPE} = \frac{1}{2N_k} \sum_k \left[\frac{1}{N_{\text{CB}}} \sum_i^{N_{\text{CB}}} \epsilon_{\text{CB}_{ik}} + \frac{1}{N_{\text{VB}}} \sum_i^{N_{\text{VB}}} \epsilon_{\text{VB}_{ik}} \right]$$

(6)

where N_k is the number of k-points in the DFT calculation, N_{CB} and N_{VB} the number of CBs and VBs averaged over, and $\epsilon_{\text{CB}_{ik}}$

and $\epsilon_{\text{VB}_{ik}}$ the DFT energy eigenvalues at each k-point. This descriptor is advantageous because it uses only bulk DFT band structure calculations and can be simply incorporated into to high throughput methodologies. BPE has been benchmarked for several binary wurtzite, zincblende, and rocksalt systems,[110] and has been used in screenings for p-type transparent conductors.[111,112] However, despite its advantages BPE does not indicate whether a semiconductor is actually dopable in practice, cannot explain deep defect levels, varies depending on how many bands are averaged over, and has not yet been benchmarked for a comprehensive set of structures and chemistries.[113]

2.4.2. Experimentally Quantifying Doping.

Dopants are introduced intrinsically or intentionally during growth, or by a subsequent processing step such as rapid thermal processing or ion implantation. At concentrations greater than approximately 1%, impurity concentration can usually be determined via X-ray fluorescence spectroscopy (XRF), X-ray photoelectron spectroscopy (XPS), energy dispersive spectroscopy (EDS), or Rutherford backscattering spectroscopy (RBS), among other methods. Some highly sensitive techniques, such as secondary-ion mass spectrometry (SIMS), can detect impurities down to parts per million or even parts per billion,[114,115] but their quantification requires reference samples. X-ray absorption spectroscopy (XAS) can be useful to determine the location and coordination of defects, that is, whether they are vacancies V_A, interstitials A_i, substitutions B_A, antisites (X_A), or complexes, but also requires standards and detailed modeling. We note that the semiconductor community sometimes uses the term "dopant" for incorporation of chemical substitutions of greater than 1%, even in solid solutions or systems, where phase segregation occurs. This appears in multiple studies referenced in this Review, so it is important to be clear about diversity of this terminology.

Because of compensation, dopant concentration does not usually equal carrier concentration, so it is essential to measure carrier concentration directly. In the context of this article, the goal of doping a semiconductor is often to increase the majority carrier concentration without significantly reducing the mobility. These two properties can be measured using a Hall effect setup, as described previously and schematically shown in Figure 4h (left). It is highly recommended to ensure that the measured carrier type is the same and the carrier density is similar upon the magnetic field reversal. Even with these precautions, it may be difficult to accurately determine whether a material is doped n-type or p-type from Hall effect measurements of low-mobility materials or magnetic compounds. In such cases, the Seebeck coefficient (i.e., thermopower) can be measured using a Seebeck thermocouple probe (Figure 4h, right), which is less sensitive to artifacts. The majority carrier type is indicated by the sign of the Seebeck coefficient, and the carrier concentration is usually inversely proportional to the magnitude of the Seebeck coefficient.

2.5. Band Positions, Alignments, and Other Properties

Additional criteria essential for the implementation of materials into optoelectronic device applications are the energetic offsets of the band edges and the Fermi level E_{F} (i.e., ionization energy, electron affinity, and work function). These offsets referenced to those of the other layers in a device and the band bending of the resulting interface or junction determine the transport of electrons and holes through the interface of the device. For example, to align a top contact n-type wide-gap material to a p-
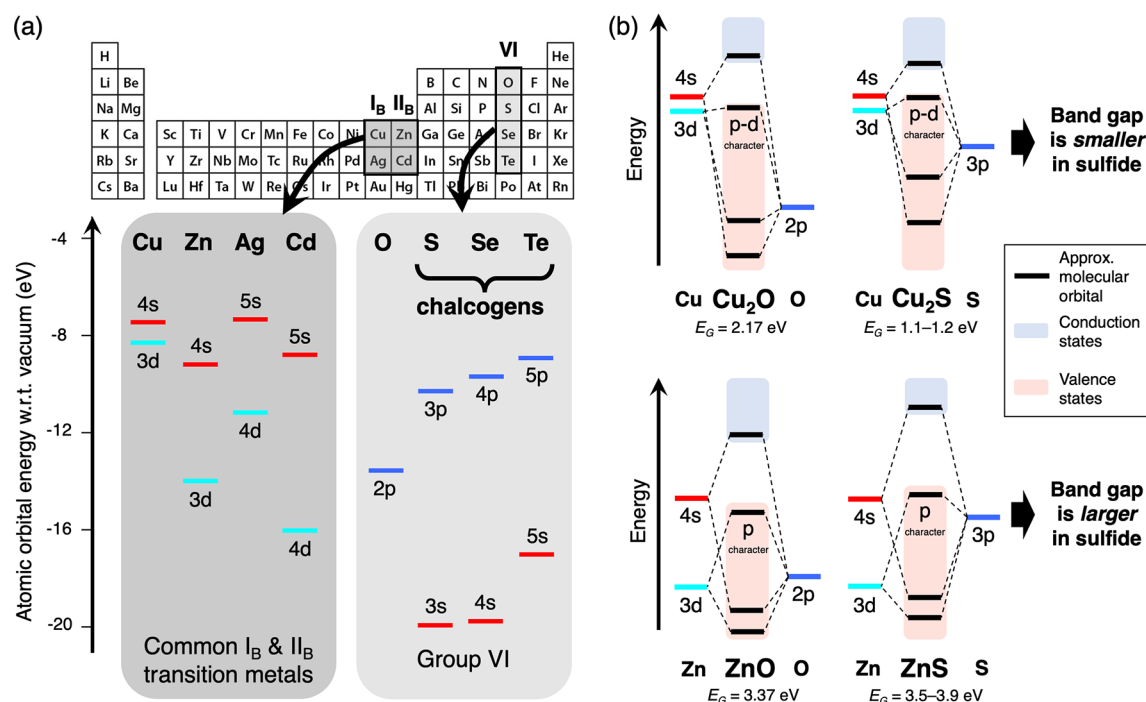
Figure 6. (a) Atomic orbital (AO) energies of group VI elements (including chalcogens S, Se, Te) and of common transition metal elements present as cations in compounds throughout this Review. Energies are from NIST database LDA calculations[121] and are aligned to experimental first ionization energies (see Supporting Information for details). (b) Molecular orbital (MO) schematics of representative binary oxides and sulfides: cuprite Cu_2O, chalcocite Cu_2S, wurtzite ZnO, and wurtzite ZnS (a wide-gap chalcogenide semiconductor, see section 3). Bonding diagrams and band offsets are approximated from the literature and density of states (DOS) calculations using a schema described in the Supporting Information.[123−126] We emphasize that these MO diagrams should be seen as schematic illustrations, as they neglect ionic bonding and cannot be directly scaled up to extended solids. For each compound, only the majority orbital contributions to the DOS are included. AO positions (colored bars) are to scale and band edges of each compound (blue and pink shading) are to scale with those of other compounds, but MO positions (black bars) and orbital splitting (dashed lines) are estimates and are not to scale.

type CdTe solar cell, the position of the CBM of the n-type material must be closely aligned in energy to the CBM of CdTe.[116] As mentioned in 2.1.3, chalcogenide materials tend to have higher VBMs closer to vacuum (lower ionization energies) than their oxide counterparts. This could enable band alignment configurations in devices and junctions that are not possible in oxides. Other properties of interest to wide band gap semiconductor materials and their practical applications include flexibility, lattice matching (i.e., interatomic distance), and microstructure, which will be discussed for materials in section 3.

2.5.1. Computational Band Alignment. As depicted in the bottom of the computation funnel of Figure 3, band alignment can be qualitatively assessed using DFT surface calculations of alternating crystal and vacuum slabs to estimate the ionization energy (IE or the VBM with respect to vacuum). These methods are reviewed comprehensively elsewhere.[117,118] Some studies have used these calculations for high-throughput screenings, in particular in searches for electrochemical catalysts and electrodes.[52] Band alignments can differ drastically depending on the surface morphology, including crystallographic plane, surface termination, and defects. As a result, band alignments in polycrystalline materials can be averaged over the most stable surfaces, but there is not yet a consensus among the DFT community about their treatment.[119] In addition, band alignments are often modified in practice when two materials are brought into direct contact (rather than contact with vacuum). Such interfacial band alignment can be accessed from explicit interface slab calculations for any material pair for which the crystallographic relationship at the interface is well-defined. This

is difficult to do for most materials without considering interfacial defects or strain; hence, such calculations are usually performed for epitaxial lattice-matched interfaces.

2.5.2. Experimental Band Alignment. Experimentally, work functions (E_F with respect to vacuum level) are typically measured by Kelvin probe or by ultraviolet photoelectron spectroscopy (UPS) from secondary electron cutoff.[120] Another powerful technique is XPS, which can be used to measure valence band offsets and band bending by following shifts in the core levels. Interfacial band alignment experiments can be performed by bottom-up (layer-by-layer deposition) or top-down (depth profiling) modes to experimentally measure band bending at interfaces, which is of particular importance to device applications. The latter mode is more common in the literature but less accurate due to chemical modification of the interface by sputtering with Ar ions. When determining band offsets from XPS core level shifts when another layer deposited on the original surface, it is important to keep in mind that the information depth depends on the kinetic energy of the photoelectrons. Complementary to XPS/UPS, Auger electron spectroscopy measurements are another possible way to detect the energy difference between E_F and the VBM. Such experimental assessment of band alignment is important for designing functional optoelectronic devices (see section 4).

3. MATERIALS

Wide band gap chalcogenide semiconductors have unique chemistries and properties compared to their oxide counterparts, which can be understood from the point of view of
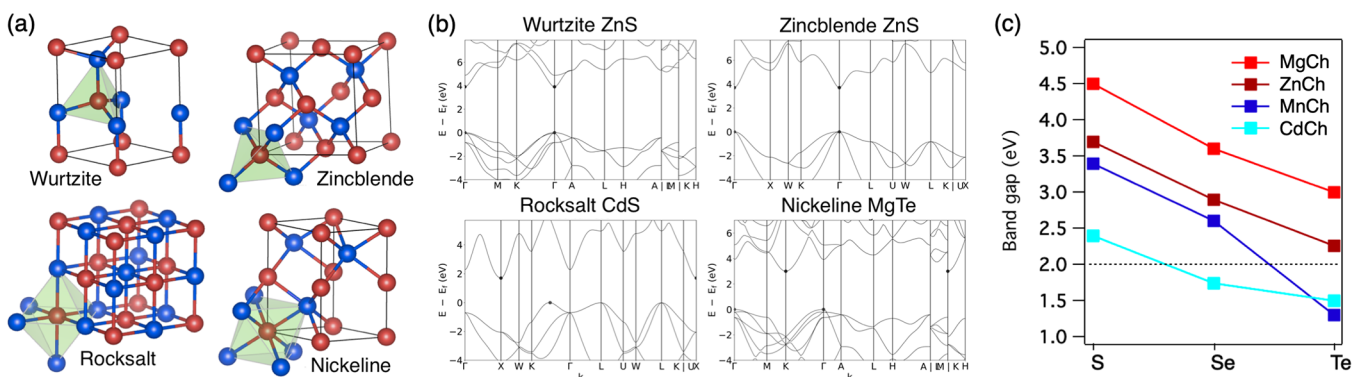
Figure 7. (a) The four most prevalent crystal structures of Zn-, Mg-, Mn-, and Cd-based binary, bivalent II-Ch metal chalcogenides. (b) Band structures of representative binaries with these crystal structures, calculated from the Materials Project database using a GGA functional and a scissor operation to correct for experimental band gap. (c) Experimental band gaps of the most stable structure of each material in this class, as discussed in this section (see Table 1).

molecular orbital theory. A simple chemical bonding schematic comparing atomic orbitals (AOs) and approximate molecular orbitals (MOs) is shown in Figure 6 (see Supporting Information for figure details) and is useful for illustrating bonding-derived distinctions between chalcogenides and oxides. Figure 6a depicts the AO energies for group VI,[121,122] demonstrating that p valence energies increase going down group VI (from O 2p, S 3p, Se 4p, Te 5p). Figure 6a also demonstrates that Ch p (and s) orbitals are much closer in energy to each other than to O 2p (and O 2s, not pictured), which helps explain why chalcogenides often crystallize in stable structures distinct from oxide counterparts but similar to one another (e.g., $CuAlO_2$ versus $CuAlCh_2$, see sections 3.3 and 3.4.3). Energy levels of common transition metals (M = Cu, Zn, Ag, Cd), which are cations in many compounds discussed in this Review, are also plotted in Figure 6a.

Figure 6b depicts molecular orbital schematics for four representative oxide and sulfide compounds (see Supporting Information). According to molecular orbital theory, orbitals closer in energy to one another are more likely to hybridize. In many common M–VI bonds, ionicity tends to decrease going down group VI, in particular in Cu–VI bonds due to Cu's high energy 3d orbitals. This promotes a larger p–d orbital overlap integral in chalcogenides than oxides, as exemplified in Figure 6b by a larger p–d overlap in Cu_2S than Cu_2O. Thus, higher energy p orbitals can hybridize more strongly with metal d orbitals. Assuming these orbitals contribute to the VB edge, this can lead to more delocalized VBMs, lower hole effective masses (see section 2),[6] and higher achievable mobilities in p-type chalcogenides as discussed in section 1 and subsequently.

The trade-off is that the band gap E_G tends to be smaller for chalcogenides than for oxides, for example, E_G of $Cu_2S < E_G$ of Cu_2O as shown in Figure 6b. However, Figure 6b also demonstrates an exception to this general trend, namely, E_G of ZnS > E_G of ZnO. One key difference between these Cu–VI and Zn–VI systems is that metal 3d states contribute significantly to the VB in Cu–VI, whereas the VB is primarily of anion p character in Zn–VI. We note that many of the compounds in this Review are Cu-based (see Tables 1–4), but some compounds still exhibit an exception to this general trend. A postulated design principle in the literature for achieving high p-type doping propensities is a small ionization energy, that is, higher position of p-orbital derived valence bands.[33] In Figure 6b, the VB edge is higher in ZnS than ZnO; ZnS has been shown to be p-type dopable (see section 3), while ZnO is definitively n-

type.[54,55] Cu_2O and Cu_2S have even higher VB edges and higher p-type dopabilities, respectively. The gap of Cu_2S is too low to be considered in this review, but many materials discussed subsequently contain Cu and thus Cu–Ch bonds.

In this section, we highlight the major advances in various classes of dopable wide band gap chalcogenide semiconductors ($E_G > 2.0$ eV) and compare their properties and their underlying physics. We will discuss bulk crystal structures, intrinsic and extrinsic dopants, and some alloys and composites, focusing mostly on materials that have been synthesized as polycrystalline thin films. Experimental band gaps and electrical properties discussed are measured at approximately 300 K, unless otherwise denoted. We also highlight some of the binary chalcogenides, ternary chalcogenides, and oxychalcogenides that have been predicted via computational searches. Many of these materials have not yet been explored in-depth for optoelectronic applications, so they open up areas of future experimental research. As stated previously, we will not cover amorphous materials or insulating materials, such as chalcogenide glasses, which are of interest but have been reviewed in depth elsewhere.[43] Materials reported in this section are summarized in Tables 1–4, and a summary figure in the end of this section.

3.1. Binary II-Ch Chalcogenides

Binary, bivalent metal chalcogenides $M^{2+}Ch^{2-}$ (Ch = S, Se, Te) are the simplest class of wide band gap chalcogenide semiconductors. The II–VI chalcogenide materials (notated II-Ch here) are the most common binaries for electronic applications, and typically contain metal cations from group II and II_B (Zn, Mg, Mn, or Cd, among others). II-Ch binaries typically crystallize in wurtzite (WZ), zincblende (ZB, also written "zinc blende", that is, sphalerite), rocksalt (RS, i.e., halite), or nickeline (NC, i.e., nickel arsenide) structures, as shown in Figure 7. These close-packed structures differ in their stacking (hexagonal close-packed in WZ and NC, face-centered cubic in RS) and their cation coordination (tetrahedral in WZ and ZB, octahedral in RS and NC).[127] The WZ, ZB, RS, and NC structures typically crystallize in space groups $P6_3mc$, $F\bar{4}3m$, $Fm\bar{3}m$, and $P6_3/mmc$, respectively.

The structural motifs in these binary chalcogenides are the building blocks for most of the wide band gap chalcogenide materials used today. Alloys and composites can be formed using these binaries as terminal compounds, forming isovalent isostructural alloys, for example, $Zn_xMg_{1-x}S$, heterovalent
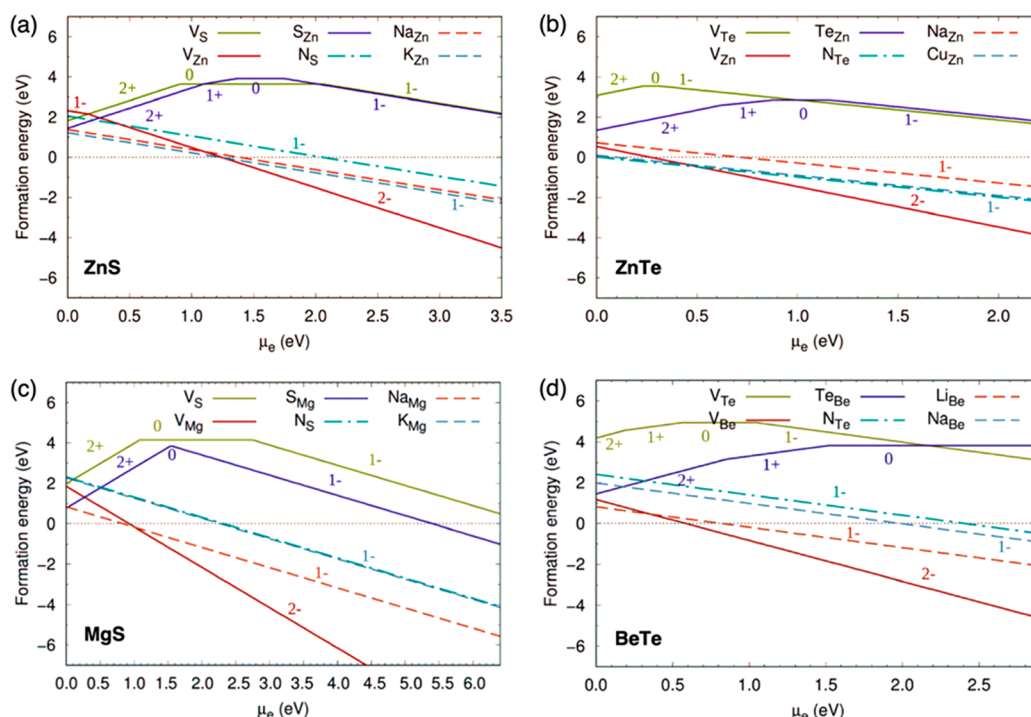
K

Figure 8. Defect formation energy plots for a representative set of binary II−VI chalcogenides: (a) ZnS, (b) ZnTe (c) MgS, and (d) BeTe. The defect formation energy $E^f[X^q]$ of a given dopant X^q is plotted as a function of chemical potential μ_e at 0 K (i.e., Fermi energy E_F). These plots show the lack of compensation for particular dopants, suggesting p-type conductivity. Reproduced with permission from ref 144. Copyright The Royal Society of Chemistry, 2008, under Creative Commons Attribution 3.0 Unported License https://creativecommons.org/licenses/by/3.0/.

heterostructural alloys with another lower gap binary, for example $Cu_xZn_{1-x}S$, or composite materials, for example, Cu_xS:ZnS. This strategy has been heavily explored in the space of n-type transparent conducting oxides and has led to state-of-the-art optoelectronic properties,[2,128] which motivates further exploration for p-type transparent conductors. Since the properties of these alloy and composite systems depend on the terminal compounds, we will focus on the binary compounds and mention only a few of their representative alloys. Next, we review the different chemistries and discuss n-type and p-type dopants in these material systems, both experimentally realized and theoretically predicted.

3.1.1. ZnCh. ZnS is one of the most prevalent sulfide minerals on Earth, and it used in numerous electronic device applications. It crystallizes in a low temperature cubic zincblende (ZB) phase ($F\bar{4}3m$), high temperature hexagonal wurtzite (WZ) phase (e.g., $P6_3mc$, most commonly with a 2H stacking polytype), or a mixture of both, depending on growth conditions.[8,129] Both structures have a fairly wide direct band gap of ∼3.7−3.8 eV for ZB and ∼3.9 eV for WZ.[130,131] These properties make both structures suitable as buffer layers and, if sufficiently dopable, as transparent electrode layers in solar cells. Importantly, ZnS is an nontoxic, earth-abundant material that is cheap and easily synthesizable in a variety of microstructures. It is closely lattice matched with $Cu(InGa)Se_2$, the absorber layer in CIGS solar cells, as well as GaP and other III−V and II−VI alloys.[132] ZnS is also important for its strong and stable luminescence, tunable across the blue to red end of the visible spectrum.[133]

The conductivity of undoped ZnS is usually very low,[134] likely due to low carrier concentration, and at slight off-stoichiometries is reported intrinsically n-type due to interstitial Zn (Zn_i) or S vacancies (V_S). However, ZnS has been reported to be

ambipolar upon extrinsic doping, e.g. n-type by Al_{Zn} (up to ∼10^{-3} S cm^{-1})[135] and p-type by Cu_{Zn} (∼10^{-5} S cm^{-1} for 0.1% Cu, and even up to ∼1 S cm^{-1} for 9%, though this may be influenced by Cu−S impurities; see section 3.1.7).[136] Other known n-type dopants are F_S (conductivities ∼2 × 10^{-7} S cm^{-1}),[137] Cl_S,[138] In_{Zn},[139] among others, and codoping strategies have been employed as p-type dopants (e.g., N/Li,[140] and In/Ag/N[139]). Both polymorphs of ZnS have low effective masses of both electrons (m_e^*) and holes (m_h^*), evident from highly dispersive CBMs and VBMs (see Figure 7). The ambipolar dopability may derive from appropriately aligned band positions with respect to vacuum, with reported electron affinities in zincblende ZnS of approximately 3.8−4.0 eV and ionization energies ∼7.5 eV by both computation and experiment (see section 4.3).[141−143] Additionally, ZnS has minimal compensating defects, as demonstrated computationally in a recent defect screening study of binary chalcogenides.[144] This study found p-type conductivity promising in doping Zn sites with Cu (Cu_{Zn}), confirming experimental results, as well as Na (Na_{Zn}), K (K_{Zn}), and doping S sites with N (N_S), as depicted in Figure 8a. This is evident by the low defect formation energy when the Fermi level E_F is near the VBM.

ZB ZnSe has a lower band gap than ZB ZnS (∼2.7 eV at room temperature, ∼2.8 eV at 10 K), but it is still sufficiently transparent for use as a window layer in solar cell applications.[145,146] It is also intrinsically n-type due to Zn_i or V_{Se}, although p-type conductivities up to ∼5 S cm^{-1} have been demonstrated in metalorganic vapor phase epitaxy films.[147] Various dopants have been explored experimentally to modify the conductivity of ZnSe, for example, N_{Se} (p-type, 0.02 S cm^{-1} and mobilities up to 13 cm^2 V^{-1} s^{-1}),[148] Ga_{Zn} (n-type, 20 S cm^{-1}),[149] Cl_{Se} (n-type, ∼333 S cm^{-1}),[150] among others. ZnSe has an even lighter effective mass than ZnS. Particularly notable
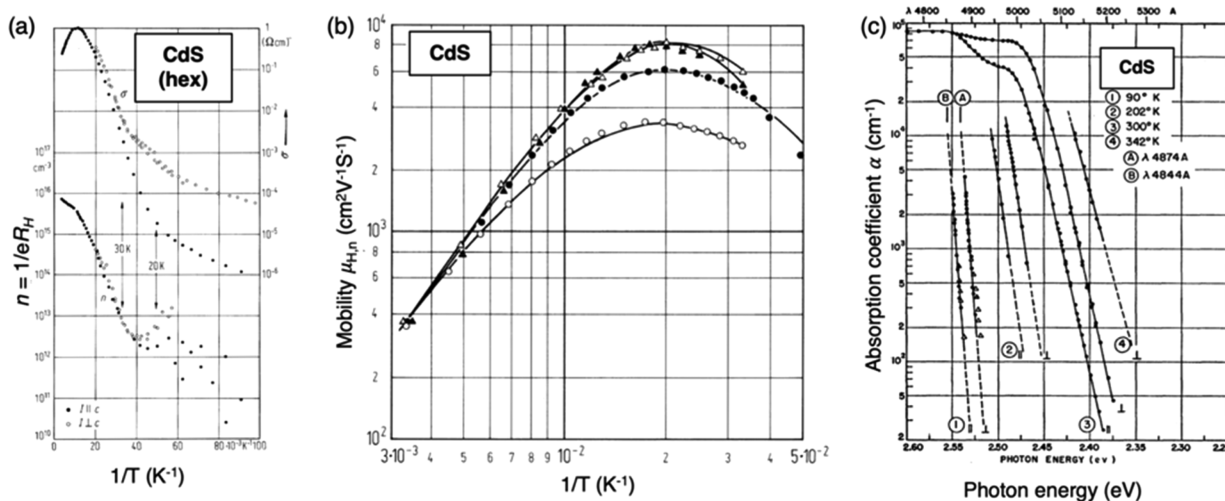
Figure 9. (a) N-type conductivity and Hall-derived carrier concentration, (b) electron mobility, and (c) absorption coefficient of wurtzite ("hex") CdS as a function of measurement temperature. Figures are from the *Semiconductors: Data Handbook* (pp 808 and 810).[163] Reproduced with permission from ref 163. Copyright 2012 Springer.

is that the mobility in high-quality, nominally updoped MBE-grown intrinsic n-type ZnSe has been reported up to 550 cm^2 V^{-1} s^{-1} at room temperature and is dominated at room temperature by polar optical phonon scattering. This high mobility motivates ZnSe's application in devices such as light emitting diodes (LEDs) and thin film transistors (TFTs).[151]

ZnTe also crystallizes in its ground state in the ZB structure, with a direct gap of ~2.3 eV,[152] and its intrinsic p-type conductivity is reportedly due to V_{Zn}. P-type dopants N_{Te} (25 S cm^{-1}),[153] Cu_{Zn} (~0.33 S cm^{-1}),[154] and Sb_{Zn} (~30 S cm^{-1})[155] improve the p-type conductivity of ZnTe, and several of these dopants have been confirmed computationally with defect studies (see Figure 8b).[144] N-type doping is trickier but has been achieved in epitaxial crystals with Al_{Zn}, Cl_{Te}, and Sn_{Zn}.[156−159] P-type ZnTe is commonly used in CdTe solar cells as a back contact due to its small valence band offset with CdTe of approximately <100 meV (see section 4),[160] and has been explored for photocatalysis applications.[161]

As expected from bonding trends and valence band positions of the chalcogen anions (see section 1), ZnS and ZnSe have a wider band gap but lower achievable dopings than ZnTe. A "δ-doping" technique has been used to leverage the wide band gap of ZnS and high dopability of ZnTe.[162] Highly conductive p-type ZnSe and ZnS films were achieved using molecular beam epitaxy (MBE) to insert heavily N-doped ZnTe layers between each layer ZnSe or ZnS layer. The hole concentration in a ZnSe/ZnTe:N δ-doped stack reaches 7×10^{18} cm^{-3}, and a [$N_a−N_d$] value reaches 5×10^{17} cm^{-3} in a ZnS/ZnTe:N δ-doped stack.[162] This is another technique that could be applied to other material spaces to engineer desired optoelectronic properties.

3.1.2. MgCh. There are fewer reports on MgCh compounds compared to ZnCh, likely because they react strongly with moisture and are not stable in air.[67] However, MgCh have larger band gaps than the other binary chalcogenide semiconductors mentioned here, so development of a stable synthesis pathway could be useful. The experimentally reported band gaps of MgS (ZB), MgS (WZ), MgSe (ZB), MgTe (ZB), and MgTe (WZ) have been estimated from MBE grown $Zn_{1−x}Mg_x$(S,Se,Te) and $Cd_{1−x}Mg_x$Te alloy films to be ~4.5 (measured at 77 K), 4.87 (measured at 77 K), ~3.6−4.05, ~3.5, and ~3 eV, respectively.[163,164,67] Considering their wide band gaps and

structural compatibility with other II−VI compounds, MgCh usually act as a critical component in various alloy structures and enable tuning of properties (see Figure 11). For example, alloying MgS with PbS in $Pb_{1−x}Mg_x$S can allow for tunable morphology, transparency, band gap, and conductivity.[165] Additionally, the lattice constant and band gaps increase with the increase of Mg content in $Zn_{1−x}Mg_x$Se,[166] and Mg content influences the band gap of $Cd_{1−x}Mg_x$Te, while maintaining a small mismatch with CdTe.[67] Polymorphs of MgCh can be stabilized when alloyed with other materials. Computational investigation has predicted rocksalt as the stable phase for MgS and MgSe, and the nickeline phase was predicted for MgTe alloys.[167] According to computational defect studies of rocksalt MgS (see Figure 8c) and wurtzite MgTe, alkali substitutional acceptor dopants Na_{Mg} and K_{Mg}, and anion substitutional dopant N_{Ch} should lead to p-type dopability. However, the doping ability of other MgCh-based alloys requires further investigation.[144]

3.1.3. MnCh. MnS is a wide-gap semiconductor that can crystallize in the WZ (γ) structure with a gap of 3.88 eV,[168] in the ZB (β) structure with a gap of 3.8 eV in single crystal samples,[169] rocksalt (α) with a gap of 2.8−3.2 eV and single crystal mobility of 10 cm^2 V^{-1} s^{-1} (the most stable phase at ambient conditions),[163] and in an amorphous phase with a gap of 2.8−3.0 eV.[170] MnS is intrinsically p-type, likely due to doubly ionized V_{Mn},[171] with a low room temperature reported conductivity of ~10^{-5} S cm^{-1},[172] and MnS has been doped by, for example, Cd_{Mn}.[173] Generally, MnSe is stable in its rocksalt (α) structure[174] and has a band gap of approximately 2.5 eV.[175] Its ZB and WZ polymorphs have also been synthesized, with reported gaps of ~3.4 and 3.5−3.8 eV,[176,177] respectively, and are structurally compatible with other III−V and II−VI semiconductor systems.[177] MnSe has been synthesized in a high-pressure nickeline (NC) phase as well. Doping has not been explored, but it is likely also p-type due to V_{Mn}. MnTe usually crystallizes in a NC phase ground state, while the band gap of the ZB polymorph of MnTe can reach 3.2 eV.[178] NC MnTe has high p-type conductivity compared to the other Mn-based compounds, up to 5−6 S cm^{-1}, with Hall mobilities up to 0.5 cm^2 V^{-1} s^{-1}, room temperature intrinsic degenerate doping of 5×10^{19} cm^{-3}, and an estimated hole effective mass of 1.5,[41] but a

lower band gap of 1.3 eV. WZ MnTe with a wider band gap of 2.7 eV can be stabilized by alloying with ZnTe,[41] or by growth on InZnO$_x$-coated glass.[179] Investigation into polymorphs with tunable band gaps and conductivities remains to be explored. We note that partially filled d orbitals in elements such as Mn and Co introduce a complication in that there can be additional magnetic degrees of freedom. Any magnetic order present, as well as hybridization between d and p orbitals, can strongly influence the material's optical and electronic properties and can often reduce the transparency window.

3.1.4. CdCh. CdS is one of the most intensively investigated wide-gap semiconductors, used in a large variety of optoelectronic applications, and has been heavily reviewed.[180−182] This material is the archetype n-type buffer layer used commercially in CdTe and CIGS solar cells,[182,183] and has been used for LEDs, TFTs, photonic/lasing devices, and piezoelectrics. CdS's most common form is hexagonal WZ, ZB phase has also been investigated, and there exists a high-pressure RS phase. Epitaxial growth has produced single phase, single crystal wurtzite material to quantify the room temperature direct gap at 2.5 eV (measured with ellipsometry), and the cubic phase has a similar but slightly lower measured direct gap of approximately ∼2.3−2.4 eV.[184] The RS phase has been reported to have an indirect gap of ∼1.5−1.7 eV, consistent with band structure calculations.[185] Polycrystalline thin films can be prepared by sputtering, chemical bath deposition (CBD), and thermal evaporation, among other methods, and tend to have a mixed WZ and ZB structure with band gaps of approximately 2.3−2.5 eV. This variation has been explained by the range of substoichiometric sulfur content in reported films because of various deposition temperatures.[184,186] WZ CdS is typically grown n-type, and is ambipolar with nearly intrinsic electron conductivity of 2.8×10^{-2} S cm^{-1} and nearly intrinsic hole conductivity of 1.5×10^{-2} S cm^{-1}.[163]

The temperature dependence of conductivity, electron concentration, and electron mobility in ultrapure CdS samples is shown in Figure 9. Hall measurements (see sections 2.3 and 2.4) of carrier concentration and conductivity generally increase as temperature increases (Figure 9a), while mobility decreases with increased temperature due to carrier scattering (Figure 9b). Figure 9c illustrates the sharp absorption edge in CdS due to its direct band gap, the directional dependence of the absorption edge in the crystal, as well as how increasing temperature lowers the absorption edge. Peak Hall n-type mobilities in ultrapure crystals have been measured up to 10^4 cm^2 V^{-1} s^{-1} at 30−40 K (see Figure 9b), while record room temperature n-type mobilities have been reported up to 160 cm^2 V^{-1} s^{-1} in CdS extrinsically doped with In$_{Cd}$ to 5×10^{19} cm^{-3} and conductivities up to ∼50 S cm^{-1}.[187,188] Hole mobilities are predicted to reach 15 cm^2 V^{-1} s^{-1}.[189] Other common n-type dopants include Ga$_{Cd}$,[190] Al$_{Cd}$,[190] and Cl$_S$,[138,191] while p-type dopants include Cu$_{Cd}$ (up to 2 S cm^{-1}, likely due to impurity band or hopping conduction)[192,193] and Bi$_S$ (up to 10^{-1} S cm^{-1} and mobilities of 3 cm^2 V^{-1} s^{-1}).[194] Compared to CdS, CdSe and CdTe have lower band gaps (<2.0 eV)[195,196] and are reviewed extensively elsewhere,[197−199] though we note they can also act as substitutional partners with other chalcogenides to form wide-gap semiconductor alloys (see Figure 11).

3.1.5. BeCh. BeS, BeSe, and BeTe all crystallize at ambient pressure in the zincblende structure. Alloyed M$_x$Be$_{1−x}$Ch compounds (M = V, Cr, C) have been investigated computationally for their ferromagnetism[200,201] but not yet as intensively for electronic properties. BeS crystallizes in a zincblende phase,

with an exceptionally high reported indirect gap of ∼5.5 eV,[202] and high pressure wurtzite and nickeline polymorphs have been computationally predicted. BeSe is also stable in the zincblende phase, with a high reported indirect gap ranging in various studies from 4.0 to 5.6 eV.[202,203] Be$_x$Zn$_{1−x}$Se and (Be,Mg,Zn)Se, which can be lattice matched to Si substrates, are used as transparent buffer layers in ZnSe-based laser diodes. BeS and BeSe have wide band gaps and low effective masses, but neither intrinsic nor extrinsic dopants (e.g., alkali and N) are favorable for p-type conductivity due to compensation.[144]

Zincblende BeTe has an experimental indirect band gap of approximately 2.7 (bulk)[202] and 2.8 eV (epitaxial thin film), and a direct gap transition of ∼4.1 eV at room temperature. It has been shown to be intrinsically p-type and has been p-doped in the literature by N$_{Te}$ to conductivities up to ∼86 S cm^{-1}, corresponding to mobilities up to 20 cm^2 V^{-1} s^{-1} and hole concentrations of 2.7×10^{19} in MBE films.[204] Because of its high conductivity, BeTe (or pseudograded superlattices of BeTe-ZnSe) is used as a p-type contact in ZnSe-GaAs-based green laser diodes. BeTe is advantageous due to its high-lying valence band, aligned to within 100 meV with GaAs, as well as a near lattice-match with GaAs and ZnSe.[204] BeTe has been explored as an alloy partner with MgTe and MnTe for this application. It has also been theoretically predicted from a high throughput screening to be p-type due to V$_{Be}$ and p-type dopable with Li$_{Be}$, as shown in Figure 8d,[144] but this and other p-type dopants have not yet been confirmed experimentally. No reports of n-type doping of BeTe could be found.

3.1.6. CaCh. CaS crystallizes in the rocksalt structure with a very wide indirect experimental gap of ∼4.5 eV, which increases with Bi doping to 4.8 eV (bulk) and 5.2 eV (nanocrystalline).[205] CaS has been studied as a solid electrolyte for its ionic conductivity.[206] (CaS-SrS):Eu^{2+} alloys have been used as phosphors for LEDs, where CaS is the host for luminescence center Eu^{2+}.[207] La-doping yields a highly resistive n-type semiconductor.[208] Rocksalt CaSe has a reported direct optical gap of 5 eV,[209] though computations have predicted a wide range of direct and indirect gaps. No investigation of electrical properties could be found. Rocksalt CaTe also exhibits an indirect gap, with an experimental absorption edge around 4.5 eV, and was very recently predicted computationally to be a potential p-type transparent semiconductor with a low hole effective mass.[210] This study acknowledged that Te$_{Ca}$ antisites could lead to hole compensation but identified a possible extrinsic p-type dopant, Na$_{Ca}$, that should have a lower formation energy than Te$_{Ca}$. Using electron−phonon coupling calculations, the mobility of CaTe was computationally predicted to be ∼20 cm^2 V^{-1} s^{-1}. Related alkali-earth chalcogenide materials, including SrS and BaS, have been also studied as wide-gap semiconductors, though no conductivity reports could be found.[211,212]

3.1.7. II-Ch Alloys and Composites. The II-Ch materials we just discussed can be alloyed with other isostructural binaries, swapping out cations or anions. Bowing in such binary alloy systems has been studied in depth (see Figure 11). Band gaps in isostructural A$_x$B$_{1−x}$ alloys can be estimated using Vegard's law with an applied bowing correction

$$E_G(x) = xE_G(A) + (1-x)E_G(B) - bx(1-x) \qquad (7)$$

where $E_G(A)$ and $E_G(B)$ are the band gaps of the end points A and B and b is the bowing parameter. One of the most technologically important alloys in this space is Cd$_{1−x}$Zn$_x$S, and other representative alloys include Cd$_{1−x}$Co$_x$S[213] and

Table 1. Experimentally Investigated Wide-Gap Binary Chalcogenides and Their Reported Optoelectronic Properties

compound	structure type	band gap (eV)	carrier type	dopant	conductivity (S cm^{-1})	refs
ZnS	ZB	~3.7−3.8	n	Al_{Zn}	~10^{-3}	135
				F_S	~2 × 10^{-7}	137
ZnS	WZ	~3.9	p	Cu_{Zn}	~10^{-5}	136
ZnSe	ZB	~2.7	n	Ga_{Zn}	20	149
				Cl_{Se}	~333	150
			p	N_{Se}	0.02	148
ZnTe	ZB	2.3	p	N_{Te}	25	153
				Cu_{Zn}	~0.33	154
				Sb_{Zn}	~30	155
MgS	ZB	~4.5				163
MgS	WZ	~4.87				163
MgSe	ZB	~3.6−4.05				163
MgTe	ZB	~3.5				67
	WZ	~3.0				67
MnS	WZ	3.88	p	V_{Mn}[171]	~10^{-5}	172
	ZB	3.8				169
	RS	2.8−3.2				163
MnSe	RS	2.5				174,175
	ZB	3.4				176
	WZ	3.5−3.8				177
MnTe	NC	1.3	p		~5−6	41
	ZB	3.2				178
	WZ	2.7				41
CdS	WZ	2.5	n	In_{Cd}	~50	182
			p	Cu_{Cd}	2	192,193
	ZB	~2.3−2.4				184
	RS	~1.5−1.7				185
BeS	ZB	~5.5				202
BeSe	ZB	4.0−5.6				202,203
BeTe	ZB	2.7−2.8	p	N_{Te}	86	204
SnS$_2$	layered $P\bar{3}m1$	~2.1−2.2	n	V_S	~1−10^{-7}	221−223
		2.9	p	S-doped	10^{-7}	224
In$_2$S$_3$	defect spinel $I4_1/amd$	1.80−2.75	n	intrinsic	2 × 10^{-4}	227
				Sn_{In}	~30	228
TaS$_2$	layered $P6_3/mmc$	2.3	n		~100	163
HfS$_3$	monoclinic $P2_1/m$	3.1	p		0.01	163
γ-Gd$_2$S$_3$	orthorhombic $Pnma$	3.4	n		0.004	163

$Cd_{1-x}Mn_xS$ (note the presence of magnetic cations). Alloys can also be formed between isostructural compounds with different cations and anions, for example, $Zn_xMg_{1-x}S_ySe_{1-y}$,[164] or with their oxide counterpart, for example, $Cu_{2-2x}Zn_xO_{1-y}S_y$.[214,215] For example, n-type ZnO_xS_{1-x} has been researched heavily as a front contact to CIGS solar cells.

An example of a II-Ch mixed with a nonisostructural and nonisovalent binary is the ternary space of $Cu_xZn_{1-x}S$ heterovalent heterostructural alloys, also denoted as Cu_xS:ZnS phase-separated composites past the solubility limit of Cu. This system has recently garnered attention due to its favorable combination of transparency and conductivity, and tunability of these properties, at low processing temperatures (25−100 °C). Cu mixing allows for hybridization with S 3p orbitals in the valence band.[216] Recent combinatorial sputtering across the full $Cu_xZn_{1-x}S$ cation alloy space (0 < x < 1) demonstrated the stabilization of a metastable wurtzite $Cu_xZn_{1-x}S$ alloy between two cubic binary end-points.[217] With 25 °C pulsed laser deposition, ZB and WZ $Cu_{0.3}Zn_{0.7}S$ alloy thin films have hole conductivities up to 40 S cm^{-1}, hole mobilities up to 1.4 cm^2 V^{-1} s^{-1}, and a direct band gap of ~3.1 eV, while in composite Cu_xS:ZnS zincblende CBD films conductivity increases to 1000

S cm^{-1} and the "gap" decreases to ~2.4 eV. (Note: Band gaps are not well-defined in composites.) This is one of the highest reported p-type conductivities for a wide-gap chalcogenide. Such CBD films have been incorporated as the heterojunction emitter layer in Si solar cells and have been studied as TFTs (see section 4).[218] These studies demonstrate that exploring combinations of a wide-gap semiconductor (e.g., ZnS) and highly conductive semiconductor (e.g., Cu_xS) could be a promising design route for discovering new tunable, low thermal budget, wide band gap p-type semiconductors.

3.2. Other Binary M_xCh_y Chalcogenides

SnS$_2$ is a layered material stacked via van der Waals forces[219] and typically crystallizes in a $P\bar{3}m1$ space group in the 2H polytype with a stacking sequence X−M−XX−M−X.[163] SnS$_2$ has been reported in single crystals with a forbidden indirect gap of ~2.1− 2.2 eV and a direct gap of 2.9 eV, though gaps have been reported in the literature between those values. A direct band gap of 2.2−2.4 eV is observed in SnS$_2$ thin films deposited by successive ionic layer adsorption and reaction,[220] but the values differ in the *Semiconductors: Data Handbook* (2.07 eV indirect, 2.88 eV indirect).[163] The n-type conductivity of SnS$_2$ is reported to range widely from ~1−10^{-7} S cm^{-1}, with carrier

concentrations $10^{13}-10^{18}$ cm^{-3} and electron mobilities in the 15−52 cm^2 V^{-1} s^{-1} range, depending on materials quality and deposition method.[221−223] It has been hypothesized using DFT defect calculations that sulfur vacancies V$_S$ act as donors to dominate n-type conductivity,[222] while in CVT grown crystals Cl$_S$ impurities are the dominant donors.[224] Carriers perpendicular to the c axis (in plane) have normal lattice scattering (phonon scattering), while those parallel to c axis (out of plane) conduct via activated hopping. p-type doping has been reported by adding excess sulfur, but conductivity is only <10^{-7} S cm^{-1}, and only one report of p-type SnS$_2$ exists, to our knowledge.[224] A high computed ionization potential of 9.54 eV and electron affinity of 7.30 eV suggest application of SnS$_2$ as an n-type buffer layer to thin film solar cells would be difficult (see Figure 24).

In$_2$S$_3$ is stable at room temperature as β-In$_2$S$_3$, an ordered defect spinel structure that crystallizes in a $I4_1/amd$ space group, although a higher temperature phase and an amorphous phase have also been reported. The energy gap of β-In$_2$S$_3$ polycrystalline thin films has been reported within the range of 1.80−2.75 eV.[163,225,226] This discrepancy in the literature spans from whether β-In$_2$S$_3$ is an indirect semiconductor, and from the possibility of mixed phases or off-stoichiometry. The conductivity mechanism has been studied in single crystal films, with undoped n-type conductivity of 2×10^{-4} S cm^{-1} at room temperature. It has been self-doped with S, with the band gap increasing to 2.43 eV in In$_2$S$_{3.9}$. Extrinsically, it has been substituted with O$_S$ to raise the gap,[227] and doped n-type with Sn$_{In}$ to increase conductivity ($\sim$30 S cm^{-1}),[228] as well as Na$_{In}$,[229] V$_{In}$,[230] and Mn$_{In}$,[231] by a variety of physical and chemical synthesis methods. No reports of p-type doping could be found. In$_2$S$_3$ has been investigated as a replacement buffer layer to CdS in CIGS, CdTe and CZTS solar cells (see section 4.1).

Wide-gap III−Se semiconductors have historically been studied for their close lattice match to Si and for Si passivation, but recent work suggests them as possible p-type TCs. Al$_2$Se$_3$ crystallizes in a tetrahedrally coordinated hexagonal Cc structure and has a wide band gap of 3.1 eV.[232] Defect calculations predicted potential p-type conductivity in Al$_2$Se$_3$ with Mg$_{Al}$ and N$_{Se}$ doping,[144] and this material has a low predicted hole effective mass of 0.56. Layered GaSe ($P6_3/mmc$) is also found to have a low planar effective mass of 0.25, and a mixture of Ga and Se p-states comprising the VBM states. Defect formation energy calculations suggest Zn$_{Ga}$ and P$_{Se}$ as appropriate dopants, but not alkalis nor N$_{Se}$ doping. Experimental measurements reveal a gap of 2 eV. Ambipolar doping has been reported in single crystals, presumably undoped p-type and Sn-doped n-type with hopping conductivity in both cases,[233] but doping has not been explored in depth.

In Table 1, we tabulate all the experimentally investigated binaries mentioned above and other wide-gap binary chalcogenide semiconductors that merit further investigation into dopability. We list their structure type, gap, doping information, and electronic properties, as reported in the references above and the *Semiconductors: Data Handbook*.[163] Computationally predicted wide-gap compounds with p-type conductivity are tabulated in Table 4. Other wide-gap binary chalcogenides with electronic properties that have not been measured and computed materials that have not been confirmed p-type are tabulated in the Supporting Information.

3.3. Ternary Chalcopyrite I-III-Ch$_2$ Compounds

We now turn our attention to ternary wide-gap chalcogenide semiconductors. In the I$_B^+$-III^{3+}-Ch$_2^{2-}$ ternary chalcopyrite

category (simplified as I-III-Ch$_2$ herein), the group I$_B$ transition metal cation is Cu^{1+} or Ag^{1+}, group III metal cation is Al^{3+}, Ga^{3+}, or In^{3+}, and the chalcogen anion Ch^{2-} is S^{2-}, Se^{2-}, or Te^{2-}. Wide-gap chalcopyrites have been investigated in depth for over 50 years for their intriguing properties and applications.[234−237] Their name stems from the chalcopyrite mineral CuFeS$_2$, and their structure is common for P and As anions, as well as chalcogens. Figure 10a shows the crystal structure of a representative compound, CuAlS$_2$ with tetragonal $I\bar{4}2d$ space

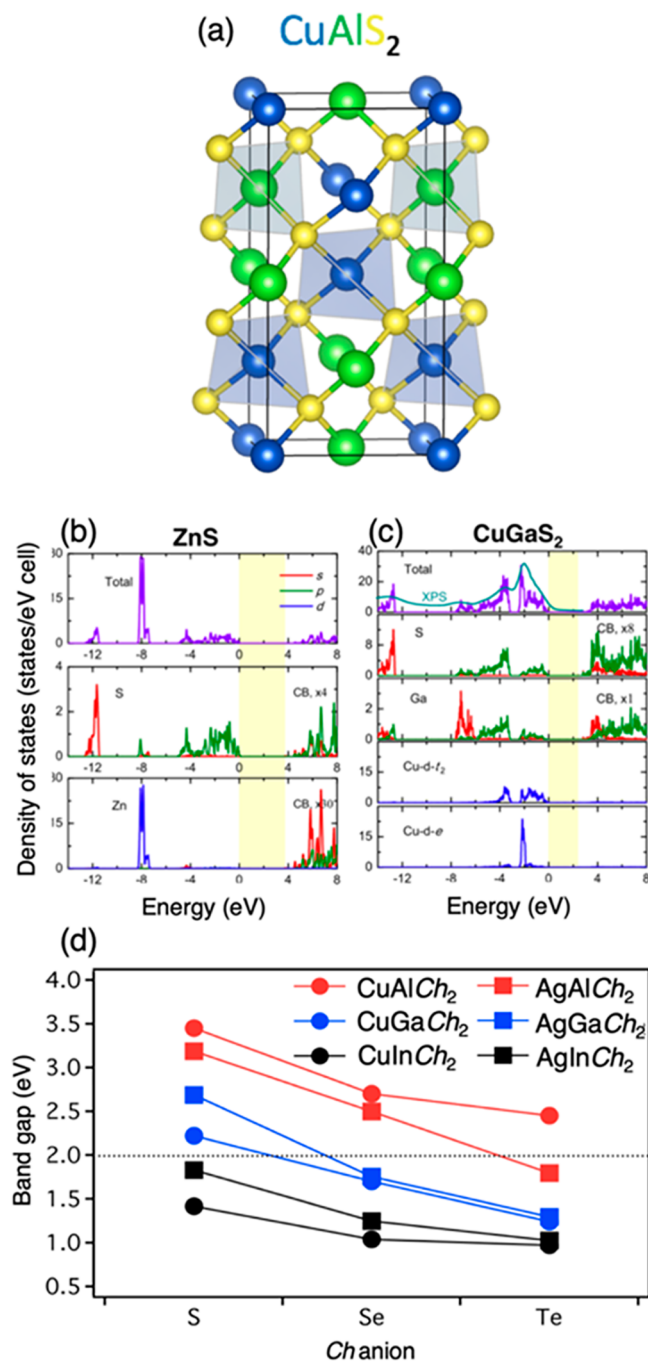**Figure 10.** Illustration of (a) the chalcopyrite structure, represented by CuAlS$_2$, and the DFT+U+G$_0$W$_0$ density of states from Zhang et al.[239] of (b) zincblende ZnS compared to (c) chalcopyrite CuGaS$_2$, indicating p−d hybridization at the VBM in the chalcopyrite structure. Reproduced with permission from ref 239. Copyright 2015 Elsevier. (d) Experimentally measured band gaps of I−III-Ch$_2$ semiconductors.

Table 2. Experimentally Investigated Wide-Gap Ternary Chalcogenides and Their Reported Optoelectronic Properties

compound	structure type	band gap (eV)	carrier type	dopant	conductivity (S cm^{-1})	refs.
CuAlS$_2$	chalcopyrite	~3.4−3.5	p	intrinsic	bulk (0.9)	248
					thin film (0.016)	249
				Cu-rich	250	30
				S-rich	4.6	11
				As$_S$	1	243
				Zn$_{Al}$	63.5	252
				Mg$_{Al}$	41.7	253
CuAlSe$_2$	chalcopyrite	~2.6−2.7	p	near-stoichiometry	3.3 × 10^{-3}	255
				Cu-rich	123	255
			n	Al-rich	2.3 × 10^{-3}	255
				intrinsic	50	256
CuAlTe$_2$	chalcopyrite	~2.1−2.5	p		~10^{-3}	258
CuGaS$_2$	chalcopyrite	2.22−2.55	p		bulk (1.7)	265
					thin film (0.7)	266
					single crystal (0.83)	264
AgAlS$_2$	chalcopyrite	~3.2				273
AgAlSe$_2$	chalcopyrite	2.5−2.7				276
AgAlTe$_2$	chalcopyrite	~2.3				278
AgGaS$_2$	chalcopyrite	~2.7	p		<10^{-5}	279
BaCu$_2$S$_2$	α-orthorhombic	2.1−2.5	p		0.1−53	12
BaAg$_2$S$_2$	CaAl$_2$Si$_2$-type	2 (calculated)				302
Cu$_3$TaS$_4$	sulvanite	3	p		1.6	132
Cu$_3$TaSe$_4$	sulvanite	2.35	p		3 × 10^{-3}	307
Cu$_3$NbS$_4$	sulvanite	2.6	p		0.1−0.2	308
Cu$_3$NbSe$_4$	sulvanite	~2.2	p		1.9	309,310
Cu$_3$PS$_4$	enargite (sulvanite-like)	2.38	p		0.2−1.0	314
Cu$_3$P(S$_3$Se)	enargite (sulvanite-like)	2.06	p		0.2−1.0	314
Ag$_3$PS$_4$	enargite (sulvanite-like)	2.88 (calculated)				315
Ag$_3$PSe$_4$	enargite (sulvanite-like)	2.09 (calculated)				315

group, consisting of tetrahedral coordination of anions and cations. The chalcopyrite structure is an isoelectronic ternary analog of the MCh zincblende structure, described previously, with a unit cell twice as large and with metal species I and III alternating between sites. It is distinct from the MCh zincblendes because of its cation ordering and resulting tetragonal distortion, resulting from unequal I-Ch and III-Ch bond lengths, and quantified by an anion displacement parameter μ.[238] The chalcopyrites have p−d and s−p hybridization at the VBM and CBM of I−III-Ch$_2$, respectively, compared to a single orbital p and s character bands in II-Ch. This is demonstrated in Figure 10b and 10c for representative structures of zincblende ZnS and chalcopyrite CuGaS$_2$.

Structural distortions, p−d hybridization, and cation electronegativity differences cause gaps of I−III-Ch$_2$ to be significantly lower than their binary counterparts.[238] However, these three features lead to a high propensity for p-type doping, and even ambipolar doping in many cases. The VBM p−d hybridization and the resulting exceptionally high dispersion at the VBM enables high hole mobilities.[239] For example, the hole effective mass of CuAlS$_2$ is approximately ten times lower than that of delafossite CuAlO$_2$ (the prototypical p-type TCO) and that of CuAlSe$_2$ is even lower. Similarly, the III-Ch bond distortion creates s−p hybridization at the CBM and leads to low electron effective masses and high electron conductivity if the material can be doped n-type. The chalcopyrite structure is highly tolerant to off-stoichiometry, facilitating intrinsic doping and the tuning of properties.[240] Intrinsic p-type dopants are typically group I vacancies (V$_I$) and group I on group III antisites (I$_{III}$), while intrinsic n-dopants may be chalcogen vacancies (V$_{Ch}$) and

group III on group I antisites (III$_I$), assuming they are sufficiently shallow. Additionally, it has been postulated that cation-terminated grain boundaries in chalcopyrites actually help increase p-type mobility in polycrystalline samples.[241]

Considering all the ion combinations discussed, the I−III-Ch system contains 18 possible chemistries. Figure 10d displays the experimentally derived optical band gap of these materials as a function of chalcogenide anion (representative reports listed in Table 2). Generally, the band gap magnitude is positively correlated with the electronegativity of the Ch anion, with the electronegativity difference between the two cations, and with atomic number (e.g., decreases along Al, Ga, In). The various combinations of cations also influence the degree of intrinsic localization and covalent bonding tendencies of the Cu 3d (and Ag 4d) states, for example, shorter Cu−S bonds lead to increased p−d VB hybridization and decreased hole effective masses.[239] Here, we summarize the eight stable semiconductors in this system whose reported experimental band gaps are above 2 eV: CuAlS$_2$, CuAlSe$_2$, CuAlTe$_2$, CuGaS$_2$, AgAlS$_2$, AgAlSe$_2$, AgAlTe$_2$, and AgGaS$_2$.

3.3.1. Cu(Al,Ga)Ch$_2$. CuAlS$_2$ (see Figure 10a) has the widest band gap (~3.4−3.5 eV) among all the I−III-Ch$_2$ chalcopyrite compounds and hence is the most transparent.[163] It was first investigated as a blue-UV LED material,[242,243] then later as a transparent semiconductor,[30] and has been synthesized using a wide variety of bulk and thin film techniques.[243−247] The p-type conductivity of undoped, near-stoichiometric CuAlS$_2$ only reaches 0.9 S cm^{-1} (bulk)[248] and 0.016 S cm^{-1} (thin film).[249] However, altering the I/III cation ratio allows for drastic changes in electronic properties. Under Cu-rich and Al-deficient

conditions ($Cu_{1+x}Al_{1-x}S_2$), the conductivity of bulk $CuAlS_2$ can reach up to 250 S cm^{-1} with high mobilities up to 21 cm^2 V^{-1} s^{-1}.[30] Similarly, bulk growth under S-rich conditions can increase conductivity to 4.6 S cm^{-1}, with lower mobilities of 0.4 cm^2 V^{-1} s^{-1}.[11] Antisite Cu_{Al} is a doubly ionized acceptor, but at near-stoichiometry its transition level $\varepsilon(0/-)$ is deep and should trap holes.[250] To qualitatively explain high off-stoichiometric conductivities, it has been calculated that the increased contribution of Cu 3d states to the VBM shifts the VB upward, decreasing the transition level and allowing for more shallow acceptor levels of Cu_{Al}.[251] This also decreases Cu–S bond length, further delocalizing the VBM. An alternative possible explanation is the presence of hard-to-measure Cu_xS impurities at Cu-rich synthesis conditions. In addition to intrinsic doping, extrinsic doping has been effective in enhancing conductivity. As_S, Zn_{Al}, and Mg_{Al} are found to be excellent p-type dopants for $CuAlS_2$, with conductivities reaching 1 (thin film),[243] 63.5 (thin film),[252] 41.7 S cm^{-1} (bulk),[253] respectively. $CuAlS_2$ has also been reported n-type dopable by Cd_{Cu}, Al_{Cu}, and Zn_{Cu} at high growth temperatures.[242] It is important to note that the optical band gap drops when p-doping the Al site, likely due to the increased VBM energy and presence of undetected Cu_xS impurities but does not under Cu-poor and S-rich conditions.[11,248]

$CuAlSe_2$ has a reported experimental band gap at near-stoichiometry of ∼2.6–2.7 eV and has been investigated for multiple applications, for example, blue LEDs, solar cells, and optical filters.[254] Similar to $CuAlS_2$, $CuAlSe_2$ is ambipolar dopable depending on the synthesis method and dopants. For example, $CuAlSe_2$ thin films grown by coevaporation have been reported p-type at near-stoichiometry with conductivity 3.3 × 10^{-3} S cm^{-1} and mobilities up to 18 cm^2 V^{-1} s^{-1}. Cu-rich conditions increased p-type conductivity nearly five orders to 123 S cm^{-1}, dropped mobility to 0.76 cm^2 V^{-1} s^{-1} at hole concentrations of 10^{21} cm^{-3}, and lowered the gap to 2.5 eV.[255] This corroborates the expectations of shifting the μ parameter, increasing the degree of p–d hybridization, and pushing the valence levels upward as discussed previously.[255] Al-rich conditions convert conductivity to n-type (2.3 × 10^{-3} S cm^{-1}) and raise the gap to 2.87 eV, and a report of epitaxial MBE films also found intrinsically n-type conductivity (50 S cm^{-1}).[255,256] Reported n-type extrinsic dopants are Zn_{Cu} and Cd_{Cu}, though V_{Cu}, Zn_{Al} and Cd_{Al} p-type compensation causes systematic uncertainties.[257]

$CuAlTe_2$, with reported gaps of ∼2.1–2.5 eV, is p-type with typical high resistivities (∼10^{-3} S cm^{-1}) and mobilities of ∼5–6 cm^2 V^{-1} s^{-1}.[258] Conductivity reportedly can reach up to ∼10 S cm^{-1} at room temperature;[259] however, its electronic properties have not been as heavily investigated as $CuAlS_2$ and $CuAlSe_2$. The growth of $CuAlTe_2$ thin films by RF sputtering is p-type as-deposited[260] but converted to n-type after a 140 °C anneal presumably due to acceptor–donor compensation.[261] $CuAlTe_2$ was found to form a good Ohmic contact to Mo and has been investigated computationally and experimentally for thermo-electrics and solar cells, among other applications.[261,262]

$CuGaS_2$ is a promising material for green LEDs, since its band gap is approximately 2.22–2.55 eV.[163,263,264] Reported p-type conductivities of bulk, thin film, and single crystal $CuGaS_2$ samples are 1.7 (660 °C anneal),[265] 0.7,[266] and 0.83 S cm^{-1},[264] respectively. Mobilities have been reported in the single crystal sample up to 15 cm^2 V^{-1} s^{-1}, with hole concentration 4 × 10^{17} cm^{-3}. This study revealed activated carrier transport in the temperature range of 5–300 K, and an activated hopping
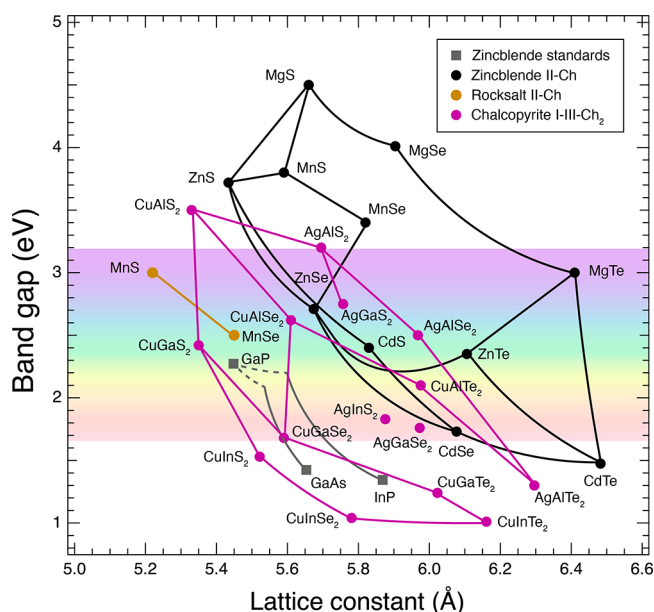

Figure 11. Room-temperature band gap vs lattice constant for the zincblende II–VI chalcogenides, rocksalt II–VI chalcogenides, and ternary I–III–VI$_2$ chalcopyrite chalcogenides discussed in this Review. A few binary standards are plotted for reference (dashed lines indicate structural phase transformations), and we include some structures below 2 eV to help conceptualize the alloy space. Bowing is plotted for the binary systems to align with literature reports.[295] Bowing is not included for ternary systems, though it has been studied in-depth for many ternary chalcopyrites.[285] We note that the zincblende structure is not the most thermodynamically stable polymorph for several of these systems (e.g., MnS, MnSe, CdS), but we plot zincblende for ease of visualization. Lattice constant data used to make this plot is from the Inorganic Crystal Structure Database (ICSD)[35,36] and is discussed and tabulated in the Supporting Information.

mechanism at temperatures less than 100 K.[267] $CuGaS_2$ has been predicted intrinsically p-type and not ambipolar, and no n-type reports have been found.[268] We note that $CuGaS_2$ has also been recently investigated as an intermediate band solar cell (IBSC) absorber, with Fe_{Ga}, Cr_{Ga}, Ti, Ge_{Ga}, and Sn_{Ga}[269,270] deep defects. $CuGaSe_2$ and $CuGaTe_2$ have low gaps of 1.68 and 1.24 eV, respectively,[271] but can serve as alloy partners (see Figure 11). We note that $I\bar{4}2d$ chalcopyrite $CuBS_2$ has been computationally predicted as a promising p-type transparent conductor, with a HSE06 direct gap of 3.41 eV, m_h^* of 1, and defect calculations suggesting p-type dopability.[272]

3.3.2. Ag(Al,Ga)Ch$_2$. $AgAlS_2$ has a comparable band gap (∼3.2 eV) to $CuAlS_2$,[273] though CBD synthesis yields a gap of 2.3 eV. However, it has been reported as unstable in air, which limits its practical applications.[274] There are few studies of its electrical properties, but it has potential to be alloyed with other chalcopyrite semiconductors. We also note that mixed ionic-electronic conductivity in this system (and in $AgGaS_2$) has been reported.[275] The experimental gap of $AgAlSe_2$ ranges from 2.5 to 2.7 eV,[276] but there are no studies of its n- or p-dopability to our knowledge. Computations predict deep extrinsic dopants Ge_{Al} and Sn_{Al} for use as an IBSC absorber.[277] $AgAlTe_2$ has an band gap energy of ∼2.3 eV, in agreement with computational predictions, and has also garnered interest as an IBSC absorber.[278]

$AgGaS_2$, with a gap of ∼2.7 eV,[279] is considered a semi-insulating material because of its extremely low reported p-type conductivity of <10^{-5} S cm^{-1},[280,281] though amorphous films

have conductivities ~1 S cm^{-1}.[282] AgGaS$_2$ has been reported with both p-type and n-type conductivity, with low dopings and mobilities up to 30 cm^2 V^{-1} s^{-1} at room temperature.[283] Under S-rich conditions, V$_{Ag}$ or V$_{Ga}$ lead to p-type doping, while in S-poor conditions (e.g., annealing in vacuum) V$_S$ defects lead to n-type doping. The proposed dominant scattering mechanism is neutral impurity or acoustic phonon scattering.[281] We note that this compound has the highest effective mass out of all of the I–III-Ch$_2$ chalcopyrites. AgGaSe$_2$ and AgGaTe$_2$ have gaps below 2 eV. Replacing Ag with Li to form LiAlTe$_2$ results in a compound with an HSE03 gap of 3.11 eV and m_h^* of 0.73, though dopability has not been studied.[210]

3.3.3. I–III–Ch$_2$ Alloys. The I–III-Ch$_2$ semiconductors can form various multinary alloys to stabilize polymorphs and to tailor the band gap, conductivity, and band edges toward a particular application. To assist in visualization of this alloy space, Figure 11 plots the band gap versus lattice constants for all of the I–III-Ch$_2$ chalcopyrite structures discussed previously, as well as a few others with gaps below 2 eV. Plotted alongside are the II-Ch zincblende compounds discussed in section 3.1, and binary zincblende III–V semiconductors GaP, GaAs, and InP for reference. Note that the effects of band gap bowing in chalcopyrites are not plotted, but many of these band gap dependencies have been shown computationally and experimentally to be close to linear with bowing parameters usually less than 0.5 eV (see below).[238,284,285] Also, alloy band gaps are only drawn here between isostructural systems with one substitution, though nonisostructural and multicomponent alloying are regularly utilized across this space, for example, zincblende (Be,Mg,Zn)Se used for UV lasers[286] and quinternary alloys CuAl$_x$Ga$_{1-x}$(S$_{1-y}$Se$_y$)$_2$.[287] We briefly discuss three strategies—alloying I, III, or Ch ions—and mention representative chalcopyrite alloys.

(Cu,Ag)-III-Ch$_2$. By alloying Cu–III-Ch$_2$ with Ag–III-Ch$_2$, one can obtain Cu$_x$Ag$_{1-x}$III-Ch$_2$. For example, Cu$_x$Ag$_{1-x}$AlS$_2$ polycrystalline thin films prepared by chemical spray pyrolysis at 360 °C have been reported, albeit with a tendency to oxidize due to residual oxidant in the precursor. It was observed that the optical band gap changes nonlinearly with respect to x, though bowing parameter was not reported.[288] Structural and optical properties of bulk Cu$_x$Ag$_{1-x}$GaS$_2$ materials have been investigated, with a large bowing parameter of 0.8 eV.[289]

I-(Ga,Al)-Ch$_2$. Alloys of CuGa$_{1-x}$Al$_x$S$_2$ were found experimentally to fit Vegard's law, with a near-linear gap versus lattice constant relation and a bowing parameter of 0.34 eV.[290,291] CuGa$_{1-x}$Al$_x$Se$_2$ has been more intensively investigated for its absorption, and has a reported bowing parameter of 0.28 eV.[246,285] In particular, Co$_{Cu}$ doping has been explored to alter absorption.[292,293] This composition has also been deposited as a layered heterostructure, which is another strategy to achieve a mixture of properties.

I–III-(S,Se,Te)$_2$. CuAl(S$_{1-x}$Se$_x$)$_2$ single crystals have a reported bowing parameter of 0.34 eV, while that of CuGa(S$_{1-x}$Se$_x$)$_2$ is approximately zero.[285] Both systems have been studied as solar absorbers. Transport properties of CuAl(S$_{1-x}$Se$_x$)$_2$ have been computed for use in thermoelectrics, finding p-type conductivity and a low theoretical power factor.[294]

3.4. Other Ternary Chalcogenides

3.4.1. α-BaM$_2$Ch$_2$, *Pnma* Structure. BaCu$_2$S$_2$ exists in two structures, a low-temperature orthorhombic structure (*Pnma*, α-BaCu$_2$S$_2$)[296] and high-temperature layered tetragonal structure

($I4/mmm$, β-BaCu$_2$S$_2$).[297] The BaCu$_2$S$_2$ reviewed here as a wide band gap semiconductor is the α phase, and we note that β-BaCu$_2$S$_2$ is primarily investigated for its thermoelectric properties.[298] As shown in Figure 12a, Ba occupies 7-fold S-coordinated sites while Cu atoms are tetrahedrally coordinated by S. In contrast with the layered delafossite structure, Cu-centered tetrahedrons are uniformly distributed in the 3D crystal. BaCu$_2$S$_2$ has a direct gap (see Figure 12b) reported experimentally between 2.1 and 2.5 eV in thin films.[12,299,300] BaCu$_2$S$_2$ has been synthesized by RF sputtering, reaching hole mobilities of 3.5 cm^2 V^{-1} s^{-1} at dopings of ~10^{19} cm^{-3}, and a conductivity of 17 S cm^{-1},[300] as well as by spin coating, reaching higher dopings of ~4 × 10^{20} cm^{-3} and conductivities up to 33.6 S cm^{-1}. This high p-type conductivity has been explained due to (1) short (~2.71 Å) Cu–Cu distances along a one-dimensional chain, allowing for a broad band along which hole conductivity takes place (see Figure 12c),[299] (2) hybridization of S 3p and Cu 3d states at the upper VB, resulting in low hole effective mass of ~0.8,[301] (3) holes from V$_{Cu}$ acceptors, and (4) a notably high ionization energy compared to other p-type chalcogenides (4.84 eV).[302] The p-type conductivity is limited by V$_S$ donor defects.[303] Combinatorial RF sputtering was used to explore the influence of off-stoichiometries and processing temperature on BaCu$_2$S$_2$ properties, as shown in Figure 12d,[12] finding conductivity to increase from 0.1 to 53 S cm^{-1} as the film transforms from amorphous to crystalline at a processing temperature of 250 °C. Higher processing temperatures lead to a drop of conductivity and increase in absorption. Both Ba and Cu off-stoichiometry can increase the conductivity at high processing temperatures, though degenerate doping limits this effect at lower temperatures. The combination of reasonably
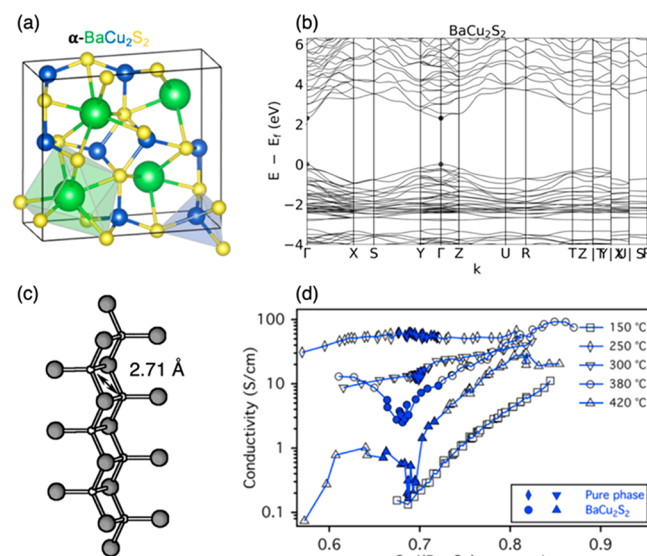
Figure 12. (a) α-BaCu$_2$S$_2$ unit cell, (b) electronic band structure of α-BaCu$_2$S$_2$ from the Materials Project database, with a scissor operation applied to correct for experimental band gap, (c) 1D chains of Cu–S within the structure from Park and Keszler,[299] where small circles are Cu atoms and large circles are S atoms, and (d) conductivity of α-BaCu$_2$S$_2$ as a function of processing temperature and Cu/(Ba+Cu) ratio.[12] Open circles indicate the presence of phase segregation within the film. Panel c is reproduced with permission from ref 299. Copyright 2002 the American Institute of Physics. Panel d is reproduced with permission from ref 12. Copyright 2017 the American Chemical Society.

high transparency, high p-type conductivity, and moderate processing temperatures makes α-BaCu$_2$S$_2$ a promising wide band gap chalcogenide semiconductor.

The semiconducting properties of BaCu$_2$Se$_2$ and BaCu$_2$Te$_2$ have also been characterized, but they are not discussed here because of their gaps below 2 eV.[304] BaAg$_2$S$_2$ ($I4/mmm$, not to be confused with its $P\bar{3}m$1 polymorph) has been calculated with HSE to have a gap just greater than 2 eV, but its mobility and conductivity have not been explored experimentally.[302] Other wide-gap compounds have been computationally predicted in this structural family, including SrCu$_2$S$_2$ (HSE gap 2.27 eV) and SrCu$_2$Se$_2$ (HSE gap 2.03 eV), with formation energies just above the convex hull (E_{hull} of 0.054 eV/atom and 0.027 eV/atom, respectively) according to theoretical calculations[302] but are difficult to synthesize.[12] It is possible that the Cu−Cu or Ag−Ag chains and hybridized VBMs could lead to high hole conductivities in these alternative structures as well.

3.4.2. Cu$_3$MCh$_4$ Sulvanite-like Materials. Compounds of the form Cu$_3$MCh$_4$ represent a group of copper-based chalcogenide semiconductors, where M is group V$_B$ transition metal V, Nb, Ta, and Ch is S, Se, Te. They share the cubic sulvanite structure (space group $P\bar{4}3m$), which leads to isotropic optical and electrical properties. Figure 13a illustrates the structure for representative compound Cu$_3$TaS$_4$. M cations are located at the corner of the unit cell, while Cu cations are edge centered. All M and Cu cations are tetrahedrally coordinated by Ch anions. This isotropic cubic structure avoids the need for special crystal substrates for epitaxial growth of common anisotropic Cu based wide band gap p-type semiconductors, which also require high growth temperatures and are difficult to make Ohmic contact to.[109] Kehoe et al. calculated indirect fundamental band gaps for this system, which decrease down the Ch group and up the M group. The band structure of Cu$_3$TaS$_4$ is shown in Figure 13c and corresponds to an average electron effective mass of 1.36 and a hole effective mass of 1.01, which could lead to high hole mobilities.[305] Similar to the other Cu-based chalcogenides, Cu 3d states mix with Ch np states at the VBM, helping delocalize the hole transport. The vacant center of

the cubic unit cell creates a "channel" along the (100) crystallographic plane, opening a pathway for ionic conductivity.[306] Considering the scope of this Review, we focus on the wide-gap sulvanites Cu$_3$TaS$_4$, Cu$_3$TaSe$_4$, Cu$_3$NbS$_4$, and Cu$_3$NbSe$_4$.

Cu$_3$TaS$_4$ thin films prepared by ALD are reported to have an indirect band gap of 2.7 eV. In contrast, computed PBEsol+U gaps are 2.1 eV (indirect) and 2.6 eV (direct).[132] Polycrystalline PLD films have an absorption onset at 3 eV, hole conductivities of 1.6 S cm^{-1}, mobilities of 0.2−0.4 cm^2 V^{-1} s^{-1} limited by sample morphology, and hole concentrations 5 × 10^{19} cm^{-3}. The gap of Cu$_3$TaSe$_4$ drops to 2.35 eV (computed indirect 1.71 eV and direct 2.22 eV).[13] Synthesized pellets confirm p-type conductivity according to Seebeck measurements, but has only been reported at ∼3 × 10^{-3} S cm^{-1}.[307] Cu$_3$NbS$_4$ has a computed indirect gap of 1.82 eV and direct gap of 2.3 eV, with a reported experimental optical gap of ∼2.6 eV.[308] Its effective mass is similar to Cu$_3$TaS$_4$, and a hole conductivity of 0.1−0.2 S cm^{-1} was reported for sintered pellets.[308] Similarly, bulk Cu$_3$NbSe$_4$ has been synthesized from stoichiometry elements.[307,308] Its predicted gap is below 2 eV, but a direct optical gap has been reported in the literature as ∼2.2 eV.[309] P-type conductivity was measured up to 1.9 S cm^{-1} in pellets. Synthesis of a p−n junction has been reported by thermal deposition of Cu$_3$NbSe$_4$ on an n-type silicon substrate.[310] Computational alloy studies found direct and indirect band gaps to vary almost linearly with x in solid solutions of Cu$_3$Ta(S$_{1-x}$Se$_x$)$_4$, Cu$_3$Nb(S$_{1-x}$Se$_x$)$_4$, and Cu$_3$Ta$_{1-x}$Nb$_x$S$_4$.[307] This was confirmed in experimental studies of Cu$_3$Nb(S$_{1-x}$Se$_x$)$_4$, finding x = 0.4 to have the highest alloy conductivity of ∼3 S cm^{-1} at room temperature.[308] Single-crystal Cu$_3$VS$_4$ has reported p-type conductivity ranging from 10^{-3}−10 S cm^{-1},[311] with a high Hall mobility of approximately 4 cm^2 V^{-1} s^{-1}. A database screening of ternary compounds predicts an HSE06 gap of 3.68,[272] but the experimentally reported gap is ∼1.3 eV.[312] Cu$_3$VSe$_4$ and Cu$_3$VTe$_4$ are p-dopable but have even lower gaps.

Cu$_3$PCh$_4$ has the same stoichiometry as Cu$_3$MCh$_4$, but its crystal structure is slightly different (i.e., "sulvanite-like") and P belongs to group V$_A$. Single-crystal X-ray diffraction of Cu$_3$PS$_4$ shows that it crystallizes in either an enargite structure or orthorhombic wurtzite-derived structure with the space group Pmn2 or Pmn2$_1$.[313] As in Cu$_3$TaS$_4$, all cations are tetrahedrally coordinated by Ch anions. Single crystals of Cu$_3$PS$_4$ (indirect optical band gap of 2.38 eV) and Cu$_3$P(S$_3$Se) (indirect optical band gap of 2.06 eV) have also been prepared by chemical vapor transport, resulting in p-type conductivity of 0.2−1.0 S cm^{-1}, and they have been implemented as cathodes for photo-electrolysis of water.[314] In addition, by replacing Cu with Ag, it has been calculated that Ag$_3$PS$_4$ (band gap of 2.88 eV) and Ag$_3$PSe$_4$ (band gap of 2.09 eV) are potential photocatalyst candidates.[315] A compound with a similar structure, KAg$_2$PS$_4$, has been predicted from first-principles to have a gap of 2.53 eV and m_h^* of 0.77, but dopability is not known.[210]

3.4.3. ABCh$_2$ Delafossites. The first predicted p-type wide-gap conducting oxide was CuAlO$_2$, which crystallizes in the delafossite structure ($R3m$ space group) and was selected based on chemical modulation of the valence band.[6] Subsequently, other delafossite oxides were synthesized as p-TCOs, including the highly conductive (albeit rather absorbing) Mg-doped CuCrO$_2$[316] and ambipolar CuInO$_2$.[317] Cu-based delafossites of the ABO$_2$ structure have been the prototypical TCO candidates because of their structural A−O−B−O−A−O channel for hole conductivity, hybridized delocalized VBM from Cu 3d and O 2p

Figure 13. (a) Crystal structure of sulvanite Cu$_3$TaS$_4$, (b) sulvanite-like Cu$_3$PS$_4$, and (c, d) their correspond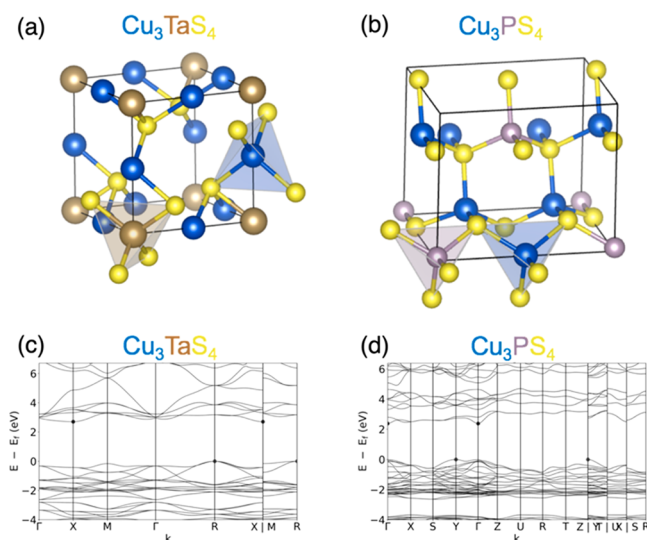ing GGA electronic band structures from the Materials Project database, with a scissor operation applied to correct for experimental band gap values.
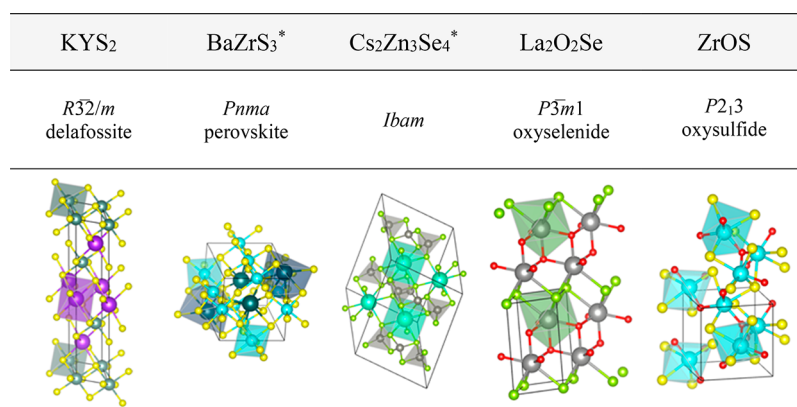
KYS$_2$	BaZrS$_3$*	Cs$_2$Zn$_3$Se$_4$*	La$_2$O$_2$Se	ZrOS
$R\bar{3}2/m$ delafossite	$Pnma$ perovskite	$Ibam$	$P\bar{3}m1$ oxyselenide	$P2_13$ oxysulfide

Figure 14. Chemical compositions and crystal structures of a representative set of computationally predicted wide-gap p-type dopable chalcogenides discussed in the text, with polyhedra to emphasize coordination. "*" indicates a new material not present in the ICSD or Materials Project database when the prediction study was performed.

orbitals, and closed d-shells to minimize visible absorption. It is reasonable that these design parameters could translate to chalcogenides, yet to date no wide-gap delafossite chalcogenides have been investigated experimentally as transparent conductors. This may be due to polymorphism; note that CuAlS$_2$, though similar in stoichiometry, crystallizes as a chalcopyrite not a delafossite.

Anticipating promise in this class of ternary chalcogenides, assuming they can be stabilized, computationally predicted wide-gap oxide and chalcogenide delafossite compounds ABCh$_2$ (Ch = O, S, Se, Te) for p-type dopability have been recently investigated.[112] This study looked not only at materials in the Materials Project, but used a global structure prediction algorithm to propose 79 new compounds. After screening for wide HSE06 gap (>2 eV), low m_h^* (>1.5), and low E_{hull}, the following class of Y- and Sc-based delafossites emerged from the selection criteria: AYS$_2$ (A = Ag[†], K, Au*), AScS$_2$ (A = K, Rb, Au*), AYSe$_2$ (A = K*, Cs), KScSe$_2$*, and BaCaTe$_2$*, with "*" indicating a new material not present in the ICSD or Materials Project database at the time of publication and "[†]" indicating a structure which, during the structure relaxation calculation, transformed from delafossite to a more stable structure (see Supporting Information). In particular, AgYS$_2$ was recommended for synthesis, with an HSE gap of 3.16 eV and a hole effective mass of 0.71. The crystal structure of another promising compound, KYS$_2$, is shown in Figure 14 for reference. Branch point energy calculations suggested midgap Fermi stabilization energies for nearly all of these compounds, which is, as discussed in section 2.4.1, not conclusive of doping type and thus defect calculations are still needed. This study is aimed toward finding p-type transparent conductors, but these predicted structures could also be used for other applications, such as those taking advantage of their magnetic properties.

3.4.4. ABCh$_3$ Perovskites. Perovskites are another class of ternary materials common as both n-type and p-type transparent conducting oxides, for example, n-type CdSnO$_3$ (CTO),[318] n-type La:BaSnO$_3$,[319] p-type In:SrTiO$_3$ (ISTO),[320] and p-type LaCrO$_3$.[321] A computational study screening for new sulfide perovskite materials as photoelectrochemical (PEC) absorbers discovered several compounds with wide band gaps (E_G > 2 eV) and low hole effective masses (m* < 1) that could be investigated as p-type transparent conductors, including BaZrS$_3$ (see Figure 14), BiGaS$_3$, BiScS$_3$, CaZrS$_3$ and ZrCdS$_3$ (see Supporting Information for other compounds and more

information).[322] These structures were screened for defect tolerance to ensure no defect states were present in the middle of the gap, though p-type dopability was not confirmed and remains to be investigated.

3.4.5. A$_2$B$_3$Ch$_4$ and Dimensional Reduction. With the exception of the materials discussed in section 3.1, many binary chalcogenides exhibit gaps lower than 2 eV. Dimensional reduction is an interesting strategy to expand the space of wide band gap ternary compounds by starting with small band gap binary constituents and widening their gaps.[323] For example, small gap binary chalcogenides MCh (Ch = S, Se, Te) can achieve a wider gap by admixing with Cs$_2$Ch to effectively reduce dimensionality (i.e., introduce layers) and reduce orbital overlap. A trade-off of this procedure, however, is a decreased dispersion due to weakened covalent bonding and thus larger hole effective masses, which is the opposite trend as going from II-Ch to I−III-Ch$_2$ material systems. On the basis of this method, a dimensional reduction on ZnCh and Cs$_2$Ch was performed, and Cs$_2$Zn$_3$Se$_4$ (see Figure 14) and Cs$_2$Zn$_3$Te$_4$ ternaries were proposed as promising p-type TCs, with HSE06 gaps of 3.61 and 2.82 eV and hole effective masses of 1.23 and 1.25, respectively. Undoped Cs$_2$Zn$_3$Se$_4$ and Cs$_2$Zn$_3$Te$_4$ were found to be intrinsically p-type materials. However, the free hole concentration may be limited by low energy of native donor defects, for example, Zn interstitials Zn$_i$.[324] Another dimensional reduction study with HgCh proposed Tl$_2$Hg$_3$S$_4$ and K$_2$Hg$_3$S$_4$ with gaps 2.22 eV and 2.2−2.6 eV, respectively.[325] The dimensional reduction strategy has only been applied to a few classes of binary chalcogenides, which have yet to be explored experimentally, so this strategy could benefit from further exploration.

3.4.6. A$_3$BCh$_3$ and Other Ternaries. Cu$_3$SbS$_3$ with the wittichenite structure ($P2_12_12_1$ space group), has a computed HSE gap of 2.02 (indirect) and 2.14 (direct), and nanowires have been reported with an experimental optical gap of 2.95 eV.[326] This material has been doped with O$_S$ to raise the gap. A screening of antimony based thermoelectric sulfides computed Li$_3$SbS$_3$, Na$_3$SbS$_3$, and Ca$_2$Sb$_2$S$_5$ to have gaps of 2.96, 3.14, and 2.11 eV, respectively, and low hole effective masses (not reported).[327] To our knowledge these materials have not yet been synthesized experimentally. This suggests incorporating information learned through screenings of thermoelectric materials to find new wide-gap chalcogenides. Other wide-gap ternary chalcogenides predicted computationally include spinels
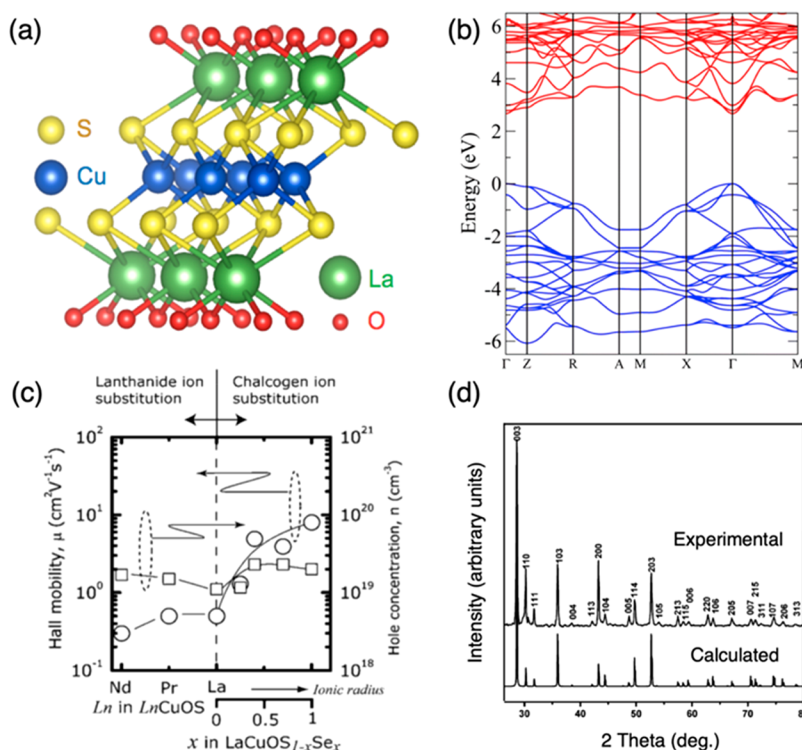
Figure 15. (a) Layered structure of LaCuOS. (b) HSE06 electronic band structure of LaCuOSe. Adapted with permission from ref 332. Copyright 2014 The Royal Society of Chemistry. (c) Hole transport properties of LnCuOCh (Ln = La, Pr, Nd; Ch = $S_{1-x}Se_x$) at 300 K as a function of chemical composition.[328] Reproduced with permission from ref 328. Copyright 2004 Springer. (d) Experimental and theoretical X-ray diffraction powder patterns of LaCuOTe.[336] Reproduced with permission from ref 336. Copyright 2007 Elsevier.

and spinel-like AB_2Ch_4 compounds e.g. Ba_2GeSe_4, Ba_2SiSe_4, (both predicted p-type dopable), $SrAl_2Se_4$ Al_2ZnS_4 (unlikely p-type dopable), and Al_2CdS_4, as well as BaB_2Se_6 and $IrSbS$, among others (see Table 4 and Supporting Information). In Table 2, we tabulate the experimentally verified ternary chalcogenides mentioned above. At the end of the table and in the Supporting Information, we include some other experimentally achieved ternary chalcogenides with wide band gaps that have not to our knowledge been explored in-depth for their electronic properties.

3.5. Quaternary and Mixed-Anion Chalcogenides

Mixing chalcogenides with oxygen or anions from other groups (e.g., halides), typically in layered motifs, results in wide band gap mixed-anion chalcogenides, such as LnCuOCh (Ln = La, Pr, Nd) and MCuChF (M = Ba, Sr).

3.5.1. LnCuOCh. We limit our discussion to LaCuOCh as a representative of the LnCuOCh oxychalcogenides family, since it has been most extensively investigated. (Pr,Nd)CuOCh have similar optoelectrical properties including band gap and p-type doping, but chalcogen type significantly influences carrier concentration as shown in Figure 15c.[328] Reported conductivities are in the planar direction. We note that these compounds are difficult to make Ohmic contact with due to their layered, anisotropic structure, and that no reports of n-type conductivity could be found in any of these systems.

LaCuOS thin films have been prepared by RF-sputtering with a direct band gap of 3.1 eV, and p-type conductivity confirmed by positive Seebeck coefficients.[329] Its undoped conductivity of 1.2×10^{-2} S cm^{-1} can be increased to 2.6×10^{-1} S cm^{-1} by partial substitution of La with divalent cations like Sr^{2+}.[330] Figure 15a shows the alternative stacking of La−O and Cu−S layers.

By substituting S with Se to form LaCuOSe, the band gap decreases from ~3.1 to ~2.8 eV but remains direct.[331] Figure 15b illustrates the HSE06 electronic band structure of LaCuOSe and its increased VBM dispersion due to Cu 3d and Se 4p mixing, with a VBM effective mass in the Γ−M direction of 0.30.[332] Epitaxial thin films of $LaCuOS_{1-x}Se_x$ solid solutions have been prepared to investigate hole transport properties, as shown in Figure 15c. The Hall mobility increases with x between ~0.5 cm^2 V^{-1} s^{-1} for LaCuOS and 8 cm^2 V^{-1} s^{-1} for LaCuOSe. This mobility is high for typical p-type transparent conductors, and the increase with x is expected because of increased hybridization with Cu 3d. The hole concentrations in undoped $LaCuOS_{1-x}Se_x$ are around 10^{19} cm^{-3} to 10^{20} cm^{-3}, so the doping is close to degenerate. Mg$_{La}$ has been shown to degenerately dope LaCuOSe, increasing carrier concentration by an order (up to 2×10^{20} cm^{-3}), while only decreasing mobility by half and raising hole conductivity up to the high reported value of 140 S cm^{-1}.[333] The layered structure induces a distinctive conduction mechanism in LaCuOSe. It was initially proposed that hole generation occurs in the $(La_2O_2)^{2+}$ layer, then holes are transported through the $(Cu_2Ch_2)^{2-}$ layer (hole conduction layer), successfully avoiding the influence of ionized impurity scattering.[334] It was later suggested by computation that the heavy hole doping from Mg may be due to the off-stoichiometry of Cu and Se rather than Mg doping at the La sites and that Sr should be a more optimal dopant than Mg.[332] Unlike LaCuOS and LaCuOSe, LaCuOTe has an indirect band gap because of the stronger La−Te interactions compared with other La−Ch.[335] A comparison of experimental and theoretical XRD patterns for LaCuOTe is shown in Figure 15d to demonstrate a single phase sample without other impurities.[336] Synthesis of a ceramic pellet of LaCuOTe yielded an optical band gap of 2.31

eV, conductivity of 1.65 S cm^{-1}, and exceptionally high Hall mobility of 80 cm^2 V^{-1} s^{-1}.[336] We note that other quaternary lanthanum copper oxysulfides, such as La$_3$CuO$_2$S$_3$ (gap of 2 eV),[337] have been investigated, suggesting further exploration of this chemistry, but electronic properties have not been reported. Substitutions of Ln have also been tried in LnCuOCh, as shown in the left section of Figure 15c.[328]

3.5.2. MCuChF. Replacing the La−O layer of LaCuOCh with a Ba−F layer results in another layered transparent semiconductor, BaCuChF. BaCuSF and BaCuSeF were first investigated in bulk form by solid state reaction and their p-type conductivity was confirmed by positive Seebeck coefficients.[338] The conductivity of undoped BaCuSF and BaCuSeF was reported as 8.8×10^{-2} and 6.1×10^{-2} S cm^{-1}, respectively, but could be enhanced significantly in both materials by doping with K$_{Ba}$ to achieve conductivities of 82 S cm^{-1} and 43 S cm^{-1}. The band gaps of BaCuSF and BaCuSeF were reported as 3.2 and 3.0 eV, respectively, and did not shift with doping.[338] Epitaxial, undoped BaCuTeF thin films have been synthesized by PLD, with reported conductivity of 167 S cm^{-1} and optical band gap close to 3 eV.[339] Elevated conductivity was reported in *c*-axis oriented BaCuTeF, likely correlating with a lower in-plane effective mass and increased mobility due to decreased scattering with fewer oxidized grain boundaries.[132] Investigations into alloys BaCuS$_{1-x}$Se$_x$F and BaCuSe$_{1-x}$Te$_x$F found the band gap to decrease linearly (negligible bowing) and conductivity to increase with increasing *x*, as shown in Figure 16.[340]

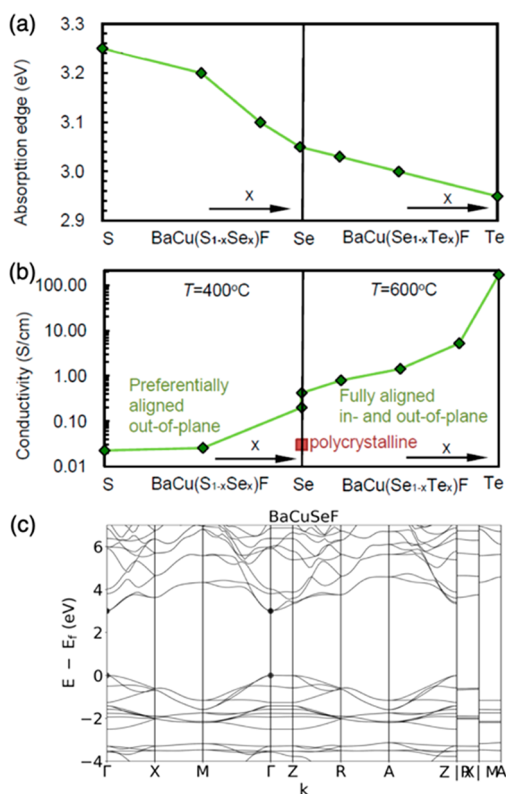**Figure 16.** (a) Absorption edge and (b) conductivity of BaCu-(Ch$_{1-x}$Ch$_x$)F thin film solid solutions. Reproduced with permission from ref 340. Copyright 2010 Elsevier. (c) GGA electronic band structure of BaCuSeF from the Materials Project database, with a scissor operation applied to correct for experimental band gap values.

SrCuSF, a layered material of the same family, has a reported band gap of 3.1 eV and p-type dopability, with Na substituting for Sr and O for S.[341] Recently, wide band gaps have been predicted computationally in the BaAgChF system of BaAgSF, BaAgSeF, and BaAgTeF, with mBJ-SR gaps of 3.13, 2.85, and 2.71 eV, respectively, and in-plane hole effective masses of 0.98, 0.94, and 0.42, respectively.[342]

3.5.3. MSCN. Copper thiocyanate, CuSCN, is a coordination polymer that typically crystallizes in a hexagonal, layered *P*6$_3$*mc* structure (*β*-CuSCN). Cu atoms are approximately tetrahedrally coordinated with three S and one N in a mixed ionic−covalent bond, while all other bonds are colinear, including a C≡N triple bond. The wide band gap of *β*-CuSCN (∼3.6−3.9 eV), its facile solution synthesis, and unusual quasi-molecular bonding character enable its device applications and its interest as a p-type transparent conductor.[15] Like other Cu-based p-type chalcogenides discussed previously, the upper valence bands have hybridized Cu 3d and S 3p character. However, the CBM at the K symmetry point has mostly a cyanide antibonding character, which leads to a more disperse VBM than CBM.[343] Dip coating synthesis on glass substrates resulted hole conductivities of 8×10^{-3} S cm^{-1} in undoped films and up to 2 S cm^{-1} with Cl doping (lowering the gap to 3.4 eV).[344] The field-effect mobility of CuSCN is reported in the range of 0.001−0.1 cm^2 V^{-1} s^{-1}.[345] P-type conductivity has been explained by Cu vacancies, and coupled C−N vacancies V$_{(CN)}$ have been proposed as an alternate method to increase conductivity.[343] Layered *β*-CuSCN has been intensively investigated recently as a solid electrolyte window layer in dye sensitized solar cells, as a hole transport layer in perovskite solar cells, and as a heterojunction partner with n-type semiconductors in TFTs and other devices.[346,347] We mention that monoclinic *α*-AgSCN (*C*2/*c*) has also reported to be a wide band gap material (3.4 eV).[348] It is studied as a battery electrode[349] but has not been as heavily investigated for optoelectronic properties.[350] A related compound, mixed-anion Pb(NCS)$_2$, was predicted as a scintillator material with a wide band gap and low m_h^*.[351]

3.5.4. Quintenary Layered Compounds. The approach of consecutively stacking O-based and S-based layers to create layered oxychalcogenide crystals has been expanded to quintenary systems. For example, thin films of Sr$_2$Cu$_2$ZnO$_2$S$_2$ have a reported optical band gap of 2.7 eV, with a E_F near the VBM indicating p-type conductivity. As with most Cu-Ch based chalcogenides, the VBM character is primarily hybridized Cu 3d and S 3p, while the CBM consists of a dispersive Zn 4s band.[352] Na doping leads to a p-type conductivity of 0.12 S cm^{-1}. This material system has been expanded by replacing Zn with Ga, In,[353] and Sc,[354] and adjusting O and S stoichiometries accordingly. The conductivity of Sr$_2$CuGaO$_3$S was improved to 2.4×10^{-2} S cm^{-1} by Na doping.[353] Additionally, Sr$_3$Cu$_2$Sc$_2$O$_5$S$_2$ combines a wide band gap of 3.1 eV and a high conductivity of 2.8 S cm^{-1}, which originates from a high hole mobility >150 cm^2 V^{-1} s^{-1}.[354]

3.5.5. Predicted Oxychalcogenides. The concept of introducing a chalcogen anion in addition to an oxygen anion has been a fruitful design route for p-type transparent semiconductors, yet only layered mixed-anion materials from the space group *P*4/*nmm* (and closely related *I*4/*mmm* for Sr$_2$Cu$_2$ZnO$_2$S$_2$) have been explored in-depth experimentally.[352] There is a trade-off between high conductivity and transparency in these materials, and they are often grown epitaxially, which can be costly and challenging to produce good device contacts.

Table 3. Experimentally Investigated Quaternary and Mixed-Anion Chalcogenide Semiconductors and Their Reported Optoelectronic Properties

compound	structure type	band gap (eV)	carrier type	dopant	conductivity (S cm^{-1})	refs
Cu_2ZnGeS_4	kesterite	2.27	p	VS	1	355
LaCuOS	tetragonal layered	3.1	p	Sr_{La}	0.26	329, 330
LaCuOSe	tetragonal layered	~2.8	p	Mg_{La}	140	331, 333
LaCuOTe	tetragonal layered	2.31	p		1.65	336
BaCuSF	tetragonal layered	3.2	p	K_{Ba}	82	338
BaCuSeF	tetragonal layered	3	p	K_{Ba}	43	338
BaCuTeF	tetragonal layered	3	p		167	339
CuSCN	layered	~3.6−3.9	p		2	15, 344
AgSCN	layered	3.4				348
$Sr_2Cu_2ZnO_2S_2$	tetragonal	2.7	p	Na	0.12	352
$Sr_2CuGaO_3S_2$	tetragonal		p	Na	2.4×10^{-2}	353
$Sr_3Cu_2Sc_2O_5S_2$	tetragonal	3.1	p		2.8	354

Additionally, each of these materials includes Cu, which may be detrimental to some device applications. This success of layered Cu-based oxychalcogenides supports the continued investigation of new oxychalcogenides with different structures, compositions, and properties.

Previous screenings on p-type transparent conducting oxides have included mixed oxychalcogenides in their findings. In the set of potential p-type TCOs calculated by Hautier and co-workers using the Materials Project, the sulfate Hg_2SO_4 and oxysulfides ZrOS (see Figure 14), and HfOS emerged as promising candidates.[92] The calculated m_h^* of these materials are 1.06, 0.96, and 0.9, and GW band gaps are 3.8, 4.3, and 4.5 eV, respectively. Defect calculations suggested all three to be intrinsically p-type. The p-type nature of Hg_2SO_4 is described by an overlap between the O/S p orbitals and Hg 6s orbitals (Hg has a filled 5d shell), while hole conductivities of ZrOS and HfOS are due to their mixed-anion nature. It is notable that oxysulfide ZrOS was found to have both a lower m^* and higher E_G than its analog sulfide ZrS_2.

Sarmadian et al. screened all oxides in the AFLOWLIB library (12 211 total compounds) for low effective mass and wide band gap and also included branch point energy (BPE) calculations as a proxy for p-type dopability.[111,92] Interestingly, out of all the oxides screened, oxychalcogenide materials proved to be the most promising. In particular, this study identified the class of $P3m1$ lanthanide oxyselenides, Ln_2SeO_2 (Ln = La, Pr, Nd, Gd) to be the most viable candidates. Their disperse VBMs (m_h^* = 0.69−0.92), wide band gaps (HSE06 gaps of 2.76−3.49 eV), and BPE levels at or near the VBM are all promising for wide band gap p-type semiconductor applications. La_2SeO_2 (see Figure 14) was studied in greater depth with defect formation energy calculations, suggesting that in anion-rich conditions Na_{La} should produce p-type conductivity without compensation from anion vacancies. If realized experimentally, this material could pose as an isotropic, Cu-free alternative to LaCuOSe. Additionally, this study revealed the following materials to consider for future investigation: $Tb_2Ti_2S_2O_5$, $NaVS_2O_8$, Hg_2SO_4, Hg_2SeO_3, $Ba_3Bi_2TeO_9$, and $CaTe_3O_8$ (though Tb- and Hg-containing compounds are impractical; see Table 4 and Supporting Information for computed properties). Additionally, oxychalcogenides Gd_2O_2Se and Y_2OS_2, among others, have been identified as potential scintillator materials, each with a low m_h^* and a relatively wide band gap.[351] Overall, prediction, synthesis, and characterization of oxychalcogenides pose a promising direction for future research. However, they also pose

unique challenges in terms of synthesis and stability that must be addressed to advance the field.

3.5.6. Quaternary Single-Anion Compounds. The most common quaternary chalcogenide structure is the kesterite structure I_2−II−IV−Ch_4, the quaternary extension of chalcopyrite. The prototype p-type kesterite Cu_2ZnSnS_4 (CZTS) has a gap ~1.4−1.5 eV (ideal for solar absorption), but there may be wide-gap materials within this ternary space or in related structural families (e.g., wurtzite-derived stannite). For example, kesterite and stannite Cu_2ZnGeS_4 have reported experimental gaps of 2.27 and 2.07 eV, respectively, and hole conductivity in the stannite phase has been reported up to ~1 S cm^{-1}.[355] α- and β-Cu_2ZnSiS_4 have higher band gaps of ~3.0 and ~3.2 eV, respectively,[356] but is effectively insulating.[355] Quaternary Ln-based $ALn_xM_yCh_z$ chalcogenides, where A is an alkali or alkali-metal (K, Rb, Cs, Ba, Sr, Cd, Mg) and M a transition metal (e.g., Cu, Ag, Zn), have been synthesized and solved for crystal structure. Band gaps tend to lie within a window of 2−2.6 eV, but there are not many published investigations of optoelectronic properties.[357−359] One such investigation reported the (010) band gaps of $CsYZnSe_3$, $CsSmZnSe_3$, and $CsErZnSe_3$ (*Cmcm* space group) as 2.41, 2.63, and 2.63 eV, respectively. $BaYCuS_3$, $BaNdCuS_3$, and $BaNdAgS_3$ have reported gaps of 2.61, 2.39, and 2.31, respectively.[360] In a table in the Supporting Information, we include Li_2GePbS_4, a computationally predicted quaternary wide-gap p-type chalcogenide derived from the sulvanite structure, but one can imagine other such compounds derived from binary and ternary structures. To compare properties of quaternary and mixed-anion chalcogenide semiconductors, we summarize the materials above in Table 3 and list others in the Supporting Information.

3.6. 2D Chalcogenides

Two dimensional (2D) chalcogenide semiconductors have been heavily investigated in recent years due to their unique properties resulting from 2D confinement. We will briefly discuss the optical and electronic properties of wide-gap 2D chalcogenides here, though they have been extensively reviewed elsewhere.[361−363] 2D materials typically possess weak interlayer van der Waals (vdW) forces with strong in-plane covalent bonds, but are not limited to this configuration. For example, several oxide-based bulk materials can be exfoliated into atomically thin crystals, for example, MoO_3 and WO_3, while in other cases the stoichiometry can differ from bulk form, for example, TiO_2.[364] 2D chalcogenides appear to be more favorable than 2D oxides for electronic applications because of their tunable band gaps and higher mobilities. Monolayer oxides

tend to have larger band gaps and lower dielectric constants compared to their bulk forms,[364,365] which suggests that thinning a 2D chalcogenide could be advantageous to attaining larger band gaps or higher transparency under visible light. In this section, we focus on wide band gap (>2 eV) 2D compounds in the following categories: transition-metal chalcogenides (TMC), post-transition-metal chalcogenides (PTMC), and transition-metal phosphorus trichalcogenides (MPT). As shown in Figure 17a, 2D chalcogenides share various crystal structures, such as the trigonal prismatic structure for WS_2 (2H-phase) from the TMC category,[366] β-phase GaSe from PTMC,[367] and $MnPS_3$ from MPT.[368]

Figure 17b summarizes predicted and experimental mobilities from the reviewed wide-gap 2D chalcogenide materials. We report mobility because it is generally more important than conductivity for optoelectronic carrier transport applications. The band gaps in 2D materials are typically a function of thickness and tend to differ substantially from bulk counterpart band gaps, as demonstrated in Figure 17c. It has been demonstrated that transition-metal dichalcogenides (TMDC), such as WS_2, exhibit indirect to direct band transition upon exfoliation from bulk crystals to monolayers.[369] Additionally, the carrier mobilities in monolayers may decrease by orders of magnitude, potentially due to charge traps introduced by substrates or surface defects, while the bulk crystal mobilities are typically limited by phonon scattering.[370] Future advances in this field will require synthesis of large and uniform atomically thin layers, comprehensive understanding of the 2D band structures and interfacial effects, and charge transfer processes across interfaces, not only to restore the mobilities to the bulk values but also improve their technological potentials. Phase engineering, heterostructure and superlattice construction, and band alignment tuning of 2D chalcogenides open up many prospects in optoelectronics.

3.6.1. Transition-Metal Chalcogenides. WS_2 in the 2H-polytype structure is an n-type indirect gap semiconductor with a band gap of ~1.35 eV.[371] Strong photoluminescence has been demonstrated from monolayer WS_2 because of the transition from its bulk indirect band gap to its monolayer direct band
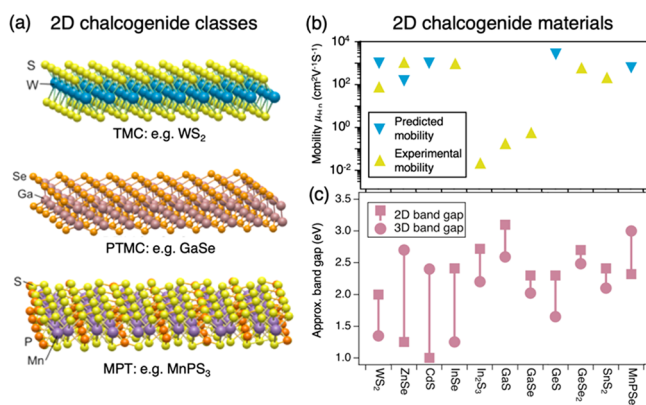
gap[372,373] of ~2 eV at room temperature.[374] Monolayer WS_2 provides the widest band gap and highest predicted phonon-limited mobility (over 1000 $cm^2\ V^{-1}\ s^{-1}$) among TMDCs (MCh_2, M = W, Mo; Ch = S, Se, Te) at room temperature.[375] Because of defects, charge traps, and Coulomb impurities, reported experimental mobility of monolayer WS_2 is only 83 $cm^2\ V^{-1}\ s^{-1}$, even after improvements via a combination of a thin layer of Al_2O_3 and thiol chemical functionalization.[376] It has been shown that in gated charge transport measurements, mechanically exfoliated monolayer WS_2 with a nitrogen plasma treatment has higher electron mobility (184.2 $cm^2\ V^{-1}\ s^{-1}$) than the scalable metal−organic CVD monolayer WS_2 (30 $cm^2\ V^{-1}\ s^{-1}$) at room temperature,[377,378] which reflects that there is still room to improve the synthesis of monolayer WS_2.[379] One recent strategy to increase monolayer mobility is doping with other transition metals, such as V and Zr.[380] The thin-layer nature of monolayer WS_2 opens up the possibility of manipulating its band structure by forming heterostructures. It is observed that conductivity enhancement and band bending occurs at the interface of WS_2-based heterojunctions.[381] 2D WS_2 has been explored as a hole-transport layer in perovskite solar cells, demonstrating higher performance and better stability than transitional conductive polymers.[382,383]

ZnS has a gap of ~3.7−3.8 eV (zincblende) in bulk form, as discussed in section 3.1.1. In monolayer ZnS, DFT GGA calculations predict a wide band gap of 2.07−2.77 eV.[384] Hydrothermal synthesized ZnS nanoparticles (15−25 nm) suggest a wider gap in the range of ~3.9−4.8 eV.[385] Monolayer ZnSe, a direct band gap semiconductor with a pseudohexagonal (ph) lattice structure,[386,387] demonstrates a high carrier mobility of 1250 $cm^2\ V^{-1}\ s^{-1}$ and generates a much higher photocurrent than in its bulk form.[388] The DFT calculated band gap of ph-ZnSe is reported to be 1.25 eV, using input atomic structural parameters from X-ray absorption fine structure (XAFS).[388] A tetragonal structure ZnSe (t-ZnSe) has been predicted under lateral pressure, with a wide band gap of 2−3 eV, and retention of its direct character up to 7% biaxial strain.[389] Computed n-type mobility of t-ZnSe is ~138.8 $cm^2\ V^{-1}\ s^{-1}$, making it a possible n-type channel material for transparent TFTs.[389]

CdS is also discussed previously as a wide band gap bulk semiconductor (~2.4 eV).[390] Several studies have investigated the synthesis and characterization of colloidal 2D nanosheets of CdS and $CdS_{1−x}Se_x$.[391,392] CdS nanosheets and nanoparticles have been intensively studied for photocatalysis by assembling into heterojunctions with other 2D materials, for example, graphene/graphene oxide,[393−395] MoS_2,[396,397] ZnSe,[398] etc., and monolayers or nanosheets can be stacked sequentially to form heterostructures. CdS/ZnSe in-plane heterostructures are predicted by HSE06 to have type-II band alignment and 2.31 eV direct band gap with the "armchair configuration", with predicted electron and hole mobilities of ~884 and ~1920 $cm^2\ V^{-1}\ s^{-1}$, respectively.[398]

3.6.2. Post-Transition-Metal Chalcogenides. The band gap of monolayer InSe is calculated to be 2.41 eV by DFT with the screened exchange (sX) hybrid density functional, in contrast to its calculated bulk indirect gap of 1.2−1.3 eV.[399] Predicted electron mobilities in atomically thin InSe are above $10^3\ cm^2\ V^{-1}\ s^{-1}$.[400,401] 2D InSe inherits the advantageous properties of bulk InSe, such as a low m_e^* and shallow dopant sites.[399,401] Several studies using InSe in optoelectronic applications have shown promising characteristics.[402,403] GaS in bulk form has a PBE predicted indirect band gap of 1.59 eV and a direct band gap of 2.59 eV.[404] Another first-principles

Figure 17. (a) Crystal structures of representative wide band gap 2D chalcogenide materials from three classes, namely, WS_2 from transition-metal chalcogenides (TMC), GaSe from post-transition-metal chalcogenides (PMT), and $MnPS_3$ from transition-metal phosphorus trichalcogenides (MPT). (b) Predicted (blue marker) and experimental (yellow marker) mobilities from a representative set of 2D materials. (c) A comparison of 2D (square marker) and bulk (i.e., 3D, circle marker) band gaps for the same set of 2D chalcogenide materials.

study predicts a direct band gap of 1.785 eV in monolayer GaS but a direct gap of 2.035 eV in bilayer GaS (less than 0.2 eV above its indirect band gap).[405] Bulk GaS has a hole mobility of ~80 cm^2 V^{-1} s^{-1},[406] while the reported electron mobility for 1.5 nm thick GaS is 0.2 cm^2 V^{-1} s^{-1}.[407] As a transistor, thin GaS demonstrates typical n-type conduction behavior with an on/off ratio of 10^4.[408] Band gap and mobility values enable GaS nanosheets as possible photodetectors.[405]

Monolayer GeS has predicted electron mobilities of 2950−3680 cm^2 V^{-1} s^{-1}, depending on the axis direction, and an indirect band gap of 2.34 eV,[409] in contrast to a calculated electron mobility of 2430 cm^2 V^{-1} s^{-1} and an HSE06 predicted indirect band gap as 2.29 eV.[409,410] Both external electric field and strain can tune the band gap.[411] Monolayer GeS has been investigated for applications such as gas sensors,[412] catalysis,[413] and photocatalysis.[414]

Bulk SnS$_2$ is a p-type semiconductor with a band gap of ~2.1 eV, as discussed in section 3.2.[415,416] Monolayer SnS$_2$ has a computed indirect band gap of 2.41 eV (by HSE06).[417] A monolayer SnS$_2$ FET demonstrates n-type conduction,[418] with an electron mobility of ~5 cm^2 V^{-1} s^{-1} reported at room temperature for exfoliated few-layer SnS$_2$. The FET devices in solution provide enhanced carrier mobilities up to 230 cm^2 V^{-1} s^{-1}.[419] This result emphasizes the sensitivity of the electronic properties of an atomic thin material on surface interactions.

The n-type semiconductor β-In$_2$S$_3$ has a reported band gap of 2.3 eV in thin film form and is the stable phase at room temperature (see section 3.2).[420] Synthesis of thin β-In$_2$S$_3$ nanosheets based on aqueous solution routes and CVD methods have been reported.[421−423] A photodetector based on β-In$_2$S$_3$ nanosheets has demonstrated a high responsivity and external quantum efficiency, while the calculated carrier mobility is 0.023 cm^2 V^{-1} s^{-1} with an on/off ratio of 1.5 × 10^3.[423] Bulk As$_2$S$_3$ is known as the mineral orpiment (layered P2$_1$/n structure) and is highly resistive p-type semiconductor with a band gap of 2.5 eV.[424] An indirect band gap of 2.12−3.18 eV has been predicted for monolayer As$_2$S$_3$, influenced by layer thickness and external strains as is observed in other 2D chalcogenides.[424]

Bulk TlInS$_2$, TlGaSe$_2$, and TlGaS$_2$ from the ternary thallium chalcogenide family TlMCh$_2$ (M = Ga or In, Ch = S, Se) have wide band gaps of >2 eV.[425−427] These compounds share a quasi-2D layered structure in bulk form, and potentially can be exfoliated to atomic-thick layers.[426] The field-effect mobility of a thin TlGaSe$_2$ sheet (~220 nm) was reported at 2.1 × 10^{-3} cm^2 V^{-1} s^{-1} with a DFT calculated band gap of 1.95 eV, though this is not technically 2D.[428] Recently, a high-throughput screening suggested that MgAl$_2$S$_4$, a layer-structured ternary chalcogenide material with a direct band gap of 2.015 eV (PBE), is stable in its monolayer form.[429]

3.6.3. Metal Phosphorus Trichalcogenides. MPS$_3$ (M = Fe, Mn, Ni, Cd, Zn) and MPSe$_3$ (M = Fe, Mn) constitute another family of layered 2D chalcogenides, some of which have been synthesized or exfoliated into monolayers.[368] The optical band gaps of monolayer MPS$_3$ and MPSe$_3$ materials vary from 1.3 to 3.5 eV, potentially suitable for photoelectrochemical applications.[368] For example, monolayer MnPSe$_3$ is predicted as a potential material for spintronic devices with electrically controllable spin polarization, while monolayer Ag$_{0.5}$Sc$_{0.5}$PSe$_3$ can serve as an efficient photocatalyst for water splitting.[430,431] The HSE calculated single layer band gaps of CdPS$_3$ and CdPSe$_3$ are 3.30 and 2.25 eV, respectively. Computed monolayer gaps are 1.93 and 1.29 eV (PBE), respectively, while the band gaps of bulk CdPS$_3$ and CdPSe$_3$ are 2.96 and 2.18 eV, respectively.[430]

Monolayer MnPSe$_3$ has a high predicted electron mobility up to 625.9 cm^2 V^{-1} s^{-1} and a predicted direct band gap of 2.32 eV.[432] To date, not many optoelectronic properties of 2D MPT materials have been experimentally demonstrated.

3.7. Summary of Optoelectronic Properties

With this breadth of wide-gap chalcogenide materials discussed above, it is of interest to summarize all of the materials and their most important properties. To provide an overview of the wide-gap chalcogenide semiconductors covered in this section, we compare the maximum achieved conductivity in the literature and the reported experimental band gaps of each material in Figure 18a (see Tables 1−3 for tabulated data). Error bars indicate the range of reported band gaps in the literature. This figure demonstrates that there are over 20 wide-gap chalcogenides with reported conductivities greater than 1 S cm^{-1}, and several with reported conductivities greater than 100 S cm^{-1}. Figure 18b includes computationally predicted wide
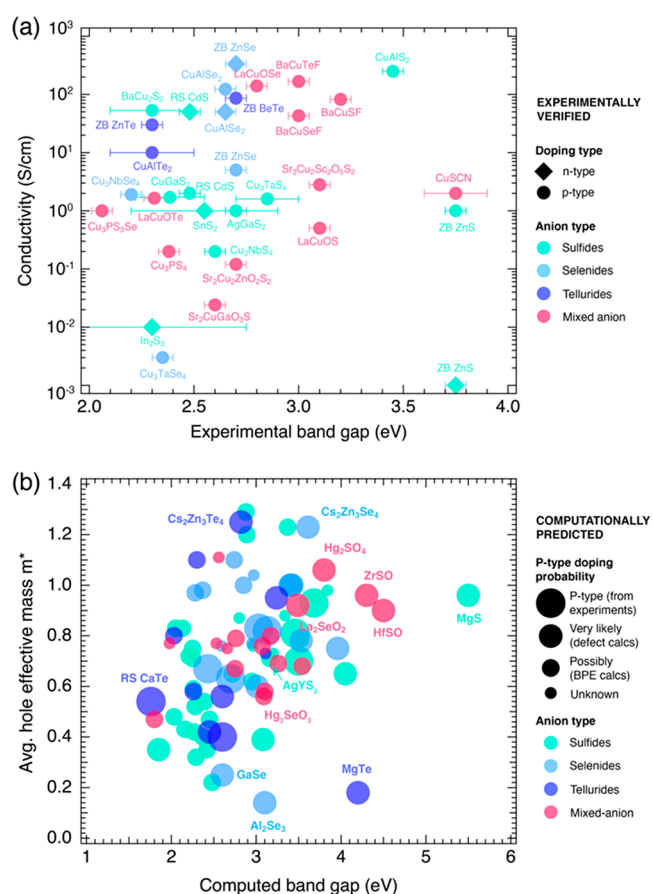

Figure 18. (a) Summary of the experimentally realized wide-gap semiconducting TCs discussed in this section, with the highest reported conductivity plotted as a function of experimental band gap. Error bars indicate the range of reported band gaps. Both n-type (diamonds) and p-type (circles) materials are plotted here. This plot only includes representative semiconductors where both conductivity and band gap are reported, and reports references in the text (Tables 1−3). (b) Computed properties of the predicted wide-gap p-type conductive materials discussed in this section. The size of the marker distinguishes the degree of certainty of p-type dopability, based on branch point energy (BPE) calculations (medium-sized) or defect calculations (large-sized). Data and references for each material are given in the text and Table 4 and the Supporting Information (note varying levels of theory for DFT calculations).

Table 4. Wide Band Gap Chalcogenides Computationally Explored in the Literature for p-Type Optoelectronic Applications[a]

material	space group	predicted band gap (eV)	DFT functional	predicted m_h^*(avg)	m_h^* calc. method	E_{hull} (eV/atom)	p-dopable?	ref.
ZnS	$F\bar{4}3m$	3.5	HSE06	0.7	EMC code		yes (exp)	144
ZnSe	$F\bar{4}3m$	2.7	HSE06	0.63	EMC code		yes (exp)	144
ZnTe	$F\bar{4}3m$	2.6	HSE06	0.4	EMC code		yes (exp)	144
MgS	$Fm\bar{3}m$	5.5	HSE06	0.96	EMC code		yes (defects)	144
MgTe	$F\bar{4}3m$	3.24	HSE03	0.95	BoltzTraP	0.9	yes (defects)	210
CaTe	$Fm\bar{3}m$	2.18 (d = 3.50)	HSE03	0.60	BoltzTraP	0	yes (defects)	210
SrSe	$Fm\bar{3}m$	3.03 (d = 3.68)	HSE03	0.83	BoltzTraP	0	yes (exp)	210
YbSe	$Fm\bar{3}m$	2.43 (d = 3.48)	HSE03	0.67	BoltzTraP	0	yes (exp)	210
YbTe	$Fm\bar{3}m$	1.76 (d = 3.09)	HSE03	0.54	BoltzTraP	0	yes (exp)	210
GaSe	$P6_3/mmc$	2.6	HSE06	0.25	EMC code	—	yes (defects)[144]	144
BeTe	$F\bar{4}3m$	2.6	HSE06	0.56	EMC code	—	yes (defects)	144
BeTe	$F\bar{4}3m$	2.45 (d = 4.04)	HSE03	0.42	BoltzTraP	0	yes (defects)[144]	210
GeS	$Pnma$	1.85 (2.5 for monolayer)	HSE06	0.35	EMC code	—	yes (defects)	144
Al$_2$Se$_3$	Cc	3.1	HSE06	0.14	EMC code	—	yes (defects)[144]	144
IrSbS	$P2_13$	3.08	HSE06	0.39	BoltzTraP (Dryad DB)	0	yes (defects)	272
RbAuSe	$Cmcm$	3.40	HSE06	1.0	BoltzTraP (Dryad DB)	0	yes (defects)	272
KAuSe	$Cmcm$	3.42	HSE06	1.0	BoltzTraP (Dryad DB)	0	yes (defects)	272
CuBS$_2$	$I\bar{4}2d$	3.41 (d)	HSE06	1.0	BoltzTraP (Dryad DB)	0	yes (defects)	272
Ba$_2$GeSe$_4$	$P2_1/m$	3.01 (d)	HSE06	0.60	BoltzTraP (Dryad DB)	0	yes (defects)	272
Ba$_2$SiSe$_4$	$P2_1/m$	3.96 (d)	HSE06	0.75	BoltzTraP (Dryad DB)	0	yes (defects)	272
BaB$_2$Se$_6$	$Cmce$	3.53	HSE06	0.78	BoltzTraP (Dryad DB)	0	yes (defects)	272
Cu$_3$VS$_4$	$P\bar{4}3m$	3.68	HSE06	0.93	BoltzTraP (Dryad DB)	0	yes (exp)	272
Cu$_3$NbSe$_4$	$P\bar{4}3m$	3.13	HSE06	0.82	BoltzTraP (Dryad DB)	0	yes (exp)[308]	272
Cs$_2$Zn$_3$Se$_4$	$Ibam$	3.61	HSE06	1.23	PBE, top VB	—	yes (defects)	324
Cs$_2$Zn$_3$Te$_4$	$Ibam$	2.82	HSE06	1.25	PBE, top VB	—	yes (defects)	324
Hg$_2$SO$_4$	$P2/c$	3.8	GW	1.06	BoltzTraP	0	yes (defects)	272
ZrOS	$P2_13$	4.3	GW	0.96	BoltzTraP	0	yes (defects)	210
HfOS	$P2_13$	4.5	GW	0.9	BoltzTraP	0.007	yes (defects)	210
Sb$_2$S$_2$O	$P\bar{1}$	1.24	DFT-GGA	1.38	BoltzTraP	0.002	yes (defects)	210
La$_2$SeO$_2$	$P\bar{3}m1$	3.49	HSE06	0.92	Avg. w/in 26 meV	0	yes (defects)	111

[a]We note that some of these have been explored experimentally (see section 3), while some warrant experimental confirmation. GW is expected to be the most accurate, followed by HSE06 and GLLB-SC, then by PBE+U (see section 2.2.1). A "d" indicates direct band gap, and hole effective mass m_h^* is averaged over three crystallographic directions. Under the column "p-type dopable?", "yes (exp)" indicates experimentally confirmed p-type dopability and "yes (defects)" indicates predicted p-type via defect formation energy calculations. More computed compounds that have not been confirmed p-type are listed in the Supporting Information.

band gap p-type semiconducting chalcogenides that have not yet been explored in-depth experimentally, plotting the average computed hole effective masses (m_h^*) as a function of computed band gap. We have compiled relevant computed data and computational methods in Table 4 for compounds confirmed p-type by experiment or defect calculations and include a table with compounds which have not yet been confirmed p-type in the Supporting Information. We note that band gaps are computed with a variety of functionals, as denoted in Table 4, so values from one study may not be directly comparable to those from another. Figure 18b indicates both compounds with confirmed p-type doping and those that have yet to be explored, with the marker size corresponding to the likelihood of p-type dopability. Though this is just a small representative set, we observe a slight positive correlation between gap and effective mass which reflects the very broad trend across materials of decreased band dispersion with widening gap. However, the key finding from across these computational studies is that many of these wide band gap chalcogenide compounds demonstrate exceptions to this trend: they have m_h^* of approximately 1 or less, which could indicate high p-type conductivities. Additionally, these materials contain cations from across the periodic table. We note that the calculation methodology differs by study, and that some studies look more in-depth into p-type dopability than

others (indicated by size of marker). As indicated by Figure 3a and b, we have covered materials with a wide range of conductivity and band gaps, paving the way for applications in a variety of optoelectronic devices which are discussed subsequently.

4. APPLICATIONS

In this section, we summarize the various roles that wide band gap chalcogenide semiconductors play in different electronic devices, focusing when appropriate on their unique advantages compared to other materials. Devices discussed here are photovoltaic (PV) solar cells, thin film transistors (TFTs), photoelectrochemical (PEC) water splitting devices, and light emitting diodes (LEDs), and a schematic of their stacking configurations and corresponding band diagrams is given in Figure 19. Other areas of interest that are reviewed elsewhere and that we will not focus on here include photodetectors, transparent diodes, laser diodes, upconverters, scintillators, gas sensors, thermoelectrics, and electrochromic windows.[1,433−441] Some traditional applications of wide band gap semiconductors, such as power electronics and radio frequency transistors,[442,443] have not been explored for chalcogenides to our knowledge, and hence are not reviewed here. For each device discussed in this section, we address the following considerations: (1) how wide
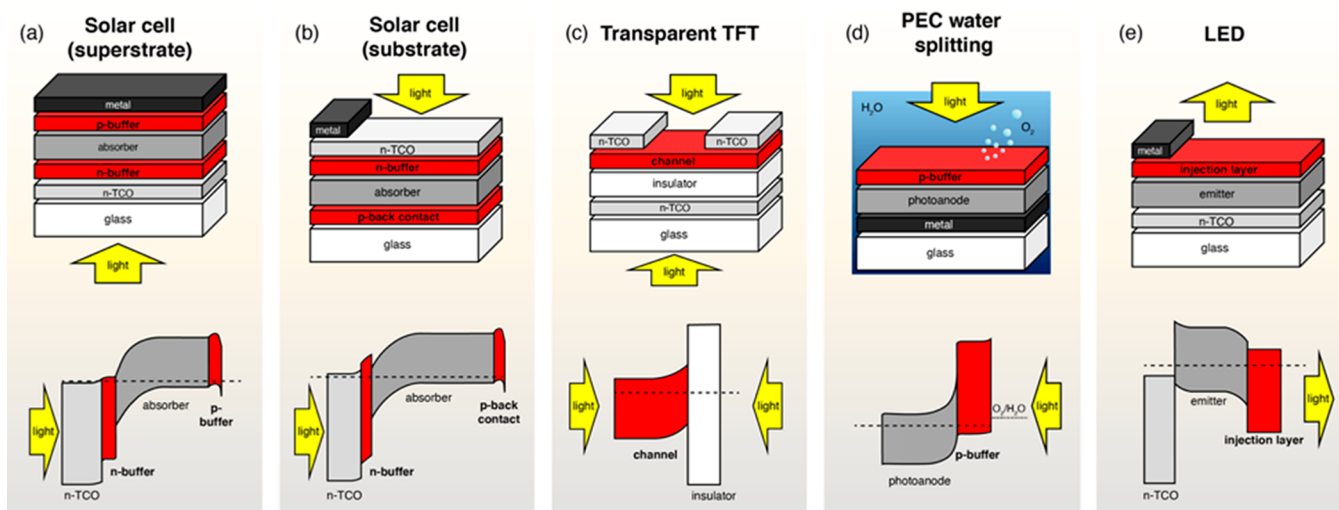
OPTOELECTRONIC APPLICATIONS

Figure 19. Comparative stack schematic of the devices discussed in this section, with corresponding representative electronic band diagrams under zero bias: (a) superstrate solar cell, for example, CdTe,[444] (b) substrate solar cell, for example, CIGS,[445] (c) transparent thin film transistor (TFT),[446] (d) photoelectrochemical (PEC) water splitting device (e.g., a one-terminal device photoanode shown only), and (e) light emitting diode (LED). Red coloring highlights the layer in which a wide-gap semiconductor can be implemented, labeling the functionality of the layer in each device, and the dotted line indicates the Fermi level E_F. Note that the y axis in the device stack corresponds to the x axis in the band diagrams (i.e., device thickness), and the thicknesses are not to scale.

band gap chalcogenide semiconductors contribute to each device, (2) which specific wide band gap chalcogenides have been implemented in each device so far, (3) what the performances are of such devices containing wide band gap chalcogenide semiconductors, and (4) what some prospective directions are for future research incorporating new wide-gap chalcogenide materials.

4.1. Solar cells

Solar cells, also known as photovoltaic (PV) cells, are one of the most prominent applications that incorporate wide-gap chalcogenide semiconductors. Here, we will focus primarily on CdTe[197] and Cu(In,Ga)(Se,S),[447] that is, CIGS (or CIGSe) devices, since they are the most commonly studied inorganic thin film solar cells that use wide-gap chalcogenide layers, but we will mention other PV applications (e.g., perovskite contacts, tandem window layers, IBSC absorbers). In this past decade (2010−2020), outstanding progress has been made in CdTe, CIGS(Se), and perovskite technologies, achieving certified power conversion efficiencies (PCE) exceeding 22% (22.1%, 23.4%, and 25.2%, respectively).[448]

4.1.1. CdTe Solar Cells. Homojunction devices are not attractive for CdTe solar cells due to CdTe's limited n-type dopability,[449] so a p−n heterojunction is typically formed between p-type CdTe and another n-type semiconductor. Figure 19a describes the layer stack of a typical CdTe solar cells in a "superstrate" configuration. A typical CdTe/CdS solar cell structure (from bottom up) consists of (1) an n-type transparent conductive oxide (TCO) on a glass substrate, usually fluorine-doped tin oxide (SnO_2:F or FTO), indium tin oxide (ITO), or cadmium stannate (Cd_2SnO_4),[450,451] (2) n-type buffer layer (also called emitter layer or window layer) on top of the TCO, such as CdS,[452−455] (3) the p-type CdTe absorber layer, with a postdeposition $CdCl_2$ treatment, (4) a p-type Ohmic back contact buffer layer to CdTe, such as Cu_xTe,[456] Te,[457] or ZnTe:Cu, and (5) a metal contact. Wide-gap chalcogenides are essential in layer (2), as a window layer between CdTe and the

n-type TCO, and in (4) as the buffer layer between CdTe and the metal back contact. Actual device stacks can be more complicated, with multiple buffer layers, but this is a basic schematic.

Front Buffer Layer to p-CdTe. One of the major purposes of this layer is to form a proper band alignment to the CdTe absorber to collect electrons and block holes. A flat or small positive conduction band offset between the CdTe and the window layer, as shown in the band diagram in Figure 19a and under bias in Figure 20a, has favorable band alignment for high cell performance. Since the light absorbed in the window layer does not contribute to the photocurrent, the band gap of the window layer should be as wide as possible to transmit maximum light to the junction and absorber. Other requirements are the ability for this layer to be deposited uniformly as a very thin film (5−50 nm) and to form thermochemically stable junctions. The band gap of CdS is ~2.4 eV and photoemission experiments have shown a valence band offset of $\Delta E_{VB} = $ ~1 eV at the CdS/CdTe interface,[452] which corresponds to a conduction band offset of ~−0.1 eV.

Historically CdS (E_G ~ 2.4 eV) was adopted as the standard "window layer" in PV, and it still is often used in research.[452−455] Although CdS provides favorable band alignment with CdTe, a spectrum loss is evident for photon energies larger than 2.4 eV (<550 nm). Such losses can be avoided by using buffer layers with higher band gaps and similar alignment. An increased transmission can be achieved by replacing the CdS with n-type ZnS (E_G of ~3.7 eV), but the band alignment at ZnS/CdTe interface is not optimal. Calculations show that the valence band offset at the interface is $\Delta E_{VB} = −0.2$ eV, while there is a very large positive conduction band offset of $\Delta E_{CB} = $ ~1.1 eV.[460] Modifying the band alignment by alloying the ZnS with CdS has been proposed, with demonstrated cell efficiencies greater than 10%. Alloying of ZnS with ZnO has been also attempted.[461] More recently, CdS has been replaced with a $Mg_xZn_{1−x}O$ (MZO) alloy. Figure 20b and c demonstrate current density
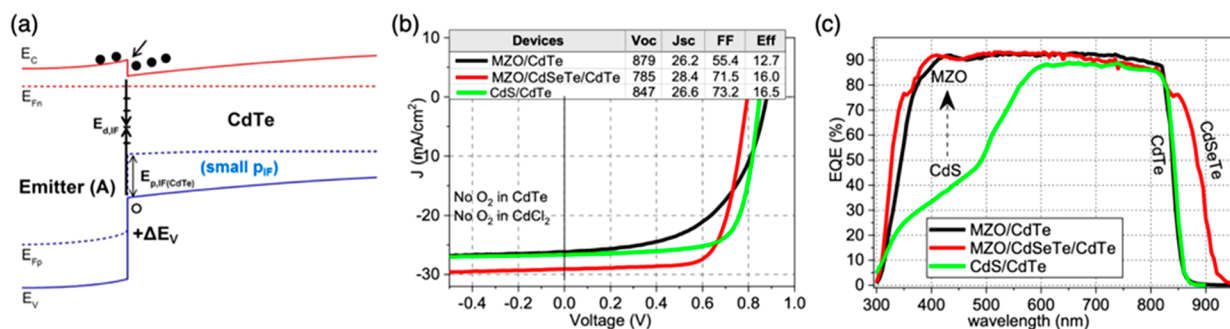
Figure 20. (a) CdTe-emitter interface under bias,[458] (b) current density versus voltage performance of different front interfaces in CdTe solar cells, and (c) a corresponding external quantum efficiency (EQE) plot.[459] In panels b and c, CdS and Mg$_x$Zn$_{1-x}$O (MZO) are compared as emitter layers. Panel a is reproduced with permission from ref 458. Copyright 2016 The American Physical Society. Panels b and c are reproduced with permission from ref 459. Copyright 2019 The Institute of Electrical and Electronics Engineers (IEEE).

versus voltage (JV) and external quantum efficiency (EQE) data from devices with different front interfaces showing the loss of current collection in CdS and how it improved when replaced with MZO. However, a new wide-gap n-type chalcogenide with good alignment could also be explored.

Back Contact to p-CdTe. Forming a low barrier Ohmic back contact to CdTe to extract photogenerated holes is challenging and is an ongoing subject of research. The Ohmic back contact does not necessarily need to be transparent, but wide band gap p-type back contacts are helpful to reflect photogenerated electrons. They would also allow for use as window layers in tandem devices or bifacial PV. CdTe has a very high ionization energy of ~5.9 eV, which would require a metal with a work function greater than or equal to 5.9 eV. However, such a metal does not exist. Direct deposition of metals with high work functions such as Au onto CdTe generally leads to an interfacial reaction, which causes Fermi level pinning at the interface and a drop-in device performance due to series resistance.

To decrease the barrier between CdTe and the metal contact, intermediate layers (buffers) are typically used. One approach, which has yielded some of the highest CdTe solar cell efficiencies, is using a very thin (~1−3 nm) Cu or Cu-containing layer between the CdTe/metal interface. The diffusion of Cu into CdTe is hypothesized as enhancing the p-type conductivity of CdTe, while it may also help reduce the back barrier between CdTe and the metal. Successful demonstration of such contacts includes Cu/Au bilayers,[462] Cu-containing graphite paste,[453] Cu$_2$Te,[463] CuCl$_2$, and Cu-doped ZnTe.[464] However, Cu may also be responsible for degradation,[465] so prospective area of research is finding a p-type non-Cu buffer layer that makes an Ohmic contact with CdTe.

An alternative strategy to mitigate this challenge is to add a thicker (~100−300 nm) electron reflector between the metal and CdTe. In addition to acting as an Ohmic contact for holes in the valence band, this layer raises the conduction band upward to create an energy barrier for electrons. Approaches to implement such an electron reflector include (1) creating positive conduction band bending in the rear interface, while maintaining a near-flat valence band offset, by heavy p-type doping near the back CdTe interface, and (2) implementing a contact with sufficiently low electron affinity and high work function to reverse the normal downward band bending. Wide-gap p-type chalcogenide materials with proper alignment are optimal for this latter strategy. P-type ZnTe, with an band gap of ~2.3 eV, is currently is a prototypical electron reflector.[466] The valence band offset at the CdTe/ZnTe interface has been

reported to be around 100 meV,[467,468] which is ideal for hole conduction through the interface. In addition, it has been reported that ZnTe can be highly p-type doped with Cu or N (>10^{20} cm^{-3}),[469,470] which can create an effective tunnel junction to the metal layer. First Solar Inc. has used ZnTe as a buffer layer and credited it with recent improvements in its world record efficiency solar cells.[471] However, it is possible that another wide-gap p-doped chalcogenide may enable even higher efficiencies, so the materials previously discussed in this Review may be interesting to explore for this application.

Top Contact to n-CdTe. Achieving a high-performing p-type transparent semiconductor also opens up the possibility of a device architecture using n-doped CdTe rather than p-doped CdTe and creating a p−n junction with n-CdTe and a p-type wide band gap chalcogenide. A transparent p-type contact would need to let light through to the absorber, have its VB closely aligned to that of CdTe, and be of high enough quality to not induce interfacial recombination or device degradation. For example, high quality monocrystalline n-type CdTe devices have been grown with amorphous Si:H as a p-type contact, but the VB alignment is not ideal.[472] Chalcogenides tend to have ionization potentials closer to vacuum, so they may have closer VB alignment to CdTe. Recently, a wide-gap p-type Cu$_x$S:ZnS nanocomposite (see section 3.1.7) was used as a transparent top contact to a monocrystalline n-type CdTe device, resulting in a high V_{oc} of nearly 1 V, but such devices have yet to be optimized.[218] Implementation of other p-doped wide band gap semiconductors into n-type CdTe devices could be an interesting area for future research, and may enable exploration of new solar cell architectures.

4.1.2. CIGS Solar Cells. High efficiency thin film solar cells based on alloys of CuInSe$_2$ (CIS) have been an ongoing research effort for decades. CuInSe$_2$ and its alloys crystallize in the chalcopyrite structure, as discussed previously (see Figures 10 and 11). The electronic and optical properties of CIS can be tuned by substituting In with Ga or Al and substituting Se with S. This leads to absorber material collectively called "CIGS" such as CuIn(S,Se)$_2$, Cu(In,Ga)Se$_2$, Cu(In,Ga)(S,Se)$_2$, etc., with a band gap range of ~1.1−1.7 eV for Cu(In,Ga)Se$_2$.[473] CIGS has emerged as one of the most promising PV materials for low-cost and high-quality thin film solar cells because of its tunable band gap, high absorption coefficient due to direct character of this gap ($\alpha > 10^5$ cm^{-1}), and high tolerance to off-stoichiometry, defects, and impurities.[474] CIGS absorbers are all intrinsically p-doped due to the presence of Cu vacancies (V$_{Cu}$), which are shallow acceptors.
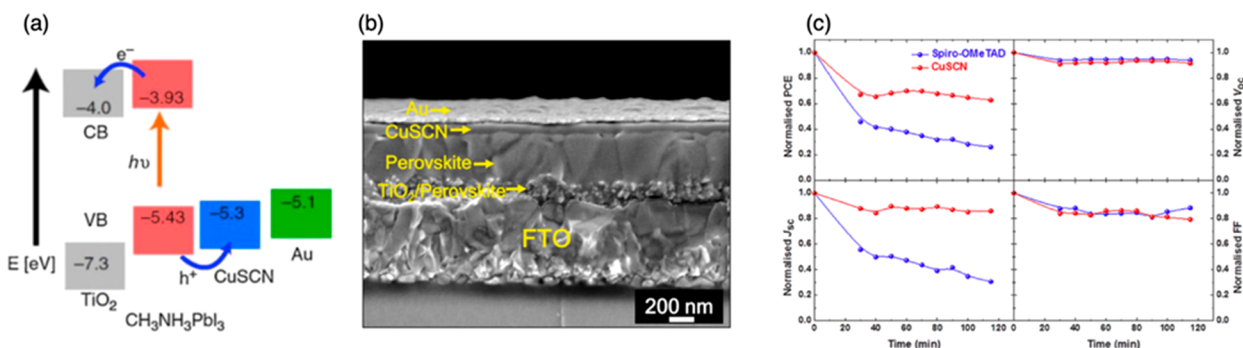
Figure 21. CuSCN as a wide-gap mixed-anion chalcogenide in a perovskite solar cell. (a) Band alignment in a perovskite solar cell, demonstrating the adequate VBM position of CuSCN with respect to $CH_3NH_3PBI_3$.[501] (b) TEM interface image from Arora et al.[497] and (c) reduced thermal degradation of cells using CuSCN, compared to Spiro-OMeTAD, from Jung et al.[500] Panel a is reproduced with permission from ref 501. Copyright 2015 Elsevier. Panel b is reproduced with permission from ref 497. Copyright 2017 American Association for the Advancement of Science (AAAS). Panel c is reproduced with permission from ref 500. Copyright 2016 Wiley.

A simplified structure of a typical CIGS cell is illustrated in Figure 19b. In contrast to the "superstrate" device configuration of CdTe with illumination from the glass side (Figure 19a), CIGS cells typically use a "substrate" configuration with illumination from the nonglass side. The front contact is a degenerately doped n-type TCO, usually Al-doped ZnO (AZO). A resistive ZnO layer is generally combined with the highly conductive TCO to form AZO/ZnO bilayers to minimize shunting. Cells require both the front contact and the buffer layer to have a wide enough band gap to minimize spectral losses. The standard back contact is Mo, which sometimes selenizes to form a thin interfacial $MoSe_2$ layer. Wide band gap p-type oxides such as MoO_x have also been researched at the back interface,[475] but no work on wide-gap chalcogenides for this layer could be found.

Various buffer layers have been used between the front contact and the CIGS absorber. The buffer layer is an n-type wide band gap material which forms a p−n junction with the p-type CIGS absorber. Similar to CdTe, the major selection criteria for the buffer layers are (1) a wide band gap to avoid undesirable absorption, (2) a suitable conduction band-offset, critical for minority carrier transport, and (3) a low defect density and controllable reactions at the interfaces. The second requirement is often the trickiest; although tuning the band gap can be achieved by varying the In/Ga or S/Se ratios in $Cu(In,Ga)(S,Se)_2$, this also alters CB alignment. For a typical, high-efficiency CIGS material composition of Cu/(In + Ga) = ∼0.9 and Ga/(In + Ga) = ∼0.3, the electron affinity is reported to be 4.5 eV.[476] Therefore, a wide band gap material with electron affinity of ∼4.2−4.5 eV is preferred, which will produce flat band offsets, or a 0.3 eV spike in the conduction band going from CIGS to a buffer.

CdS has been widely adopted as a buffer layer, with a spike-type CB offset. The experimental determination of the VB offset at the CIGS/CdS interface is ΔE_{VB} = 0.8−1.1 eV,[477] leading to an estimated 0.0−0.3 eV CB offset. Theoretical calculations suggest the lack of a strong dependence of ΔE_{VB} on the Ga content, since the introduction of Ga into $CuInSe_2$ primarily shifts the CB to higher values,[478] and experimental observations corroborate the theory.[478] Thus, for CIGS solar cells with a higher Ga content, finding an alternative n-type buffer layer is especially important.

For this reason and because of the small band gap of CdS (2.4 eV) and spurious optical absorption, alternative buffer layers have been developed. Binary chalcogenides, such as n-type CdSe, ZnS, ZnSe, and ZnTe, have been investigated as potential buffer layers.[479] Currently, Zn(S,O) is extensively used. Adjusting x in $ZnO_{1-x}S_x$ can tune the gap from that of wurtzite ZnO (3.2 eV) to that of zincblende ZnO (3.6 eV), and conduction band offsets, ΔE_C, from −0.1 to 0.3 eV at the Zn(O,S)/CIGS interface, albeit with large band bowing at intermediate compositions. This allows for largely unimpeded electron transfer, forming a foundation for high-efficiency Zn(O,S) buffer based CIGS solar cells.[480] N-type In_2S_3 has also been investigated as a buffer layer, resulting in ∼16% efficiency cells.[481] As discussed in section 3, the optical band gap of the In_2S_3 are 1.9−2.8 eV, where the range is due to different phases, deposition techniques and the In/S ratio. CB offsets of the In_2S_3/CIGSe interface have been reported in a wide range, from −0.45 to 0.5 eV.[482] However, the interfacial chemistry is complex, and several reports have observed chemical reactions occurring at the interface.[483−485] The highest efficiencies in CIGS solar cells with CdS and Zn(O,S) buffer layers are 22.3% and 22.8%, respectively,[486] and the search for the next generation of buffer layers is still underway.

Other chalcogenide materials mentioned in section 2 have been also researched for CIGS solar cells. A thin p-type $CuGaS_2$ layer, sandwiched between a p-type $CuInS_2$ absorber layer and a Mo back contact, has a beneficial effect on the performance of thin-film CIGS solar cells fabricated on glass substrates.[487] A thin interlayer of $CuAlS_2$ has been also considered promising for its high thermal stability and wide band gap. Besides CIGS, n-type and p-type wide-gap chalcogenide materials have been researched for $Cu_2ZnSn(S,Se)_4$ solar cells (i.e., CZTS, $CZTS_{1-x}Se_x$), with quaternary kesterite crystal structures (see section 3.5.6) and similar material parameters as CIGS. Similar to CIGS, CdS, and ZnS buffer layers have been used for CZTS solar cells.[488−490] However, since CZTS devices have similar interfacial properties but lower efficiency than CIGS, this Review does not go into detail, and instead, we refer the reader elsewhere.[491]

4.1.3. Additional PV Applications. *Silicon PV.* An ongoing field of research in silicon heterojunction (SHJ) photovoltaics is the development of hole-selective contacts to Si to replace traditional homojunctions formed by diffusion doping.[492] An example of an SHJ device is a HIT cell (heterojunction with intrinsic thin layer), with a heterojunction between amorphous Si and crystalline Si. Wide-gap p-type transition metal oxides, such as MoO_x and WO_3, have been reported as hole-selective contacts with high V_{OC}, and transparent graphene and carbon

nanotubes have been investigated as well.[493,494] This is another space where implementation of a wide-gap chalcogenide-based semiconductor with sufficient alignment to the Si VBM could be fruitful, so long as passivation of the absorber is maintained. For example, it was recently demonstrated that a nanocomposite of $Cu_xS:ZnS$ could be used as a hole-selective contact to n-type Si, and proof-of-concept devices were fabricated with V_{OC} up to 535 mV and J_{SC} of 21 mA/cm^2, using 1 sun illumination.[495] There also may be applications for wide-gap chalcogenide contacts in bifacial Si solar cells.

Hybrid Organic−Inorganic Halide Perovskite Solar Cells. Hybrid organic−inorganic halide perovskite solar cells, based on $CH_3NH_3PbI_3$ (i.e., MAPI) and related absorbers, have gained huge prominence in the past decade, but there are still many major engineering challenges to be solved. The challenge of relevance to this review article is finding a high performing hole transport layer (HTL or HTM).[496] Typically, polymer materials such as Spiro-OMeTAD have been used for this layer, but their conductivities are very low, and finding optimal replacements is an active area of research. Wide-gap chalcogenides could serve as this layer due to their high mobilities and adequate band alignment. As depicted in Figure 21a and b, CuSCN is a common material used as an HTM in both perovskite solar cells and dye sensitized solar cells (DSSC).[344,497,498] Kesterite Cu_2ZnSnS_4 has been also applied as an HTM to perovskite solar cells.[499] An additional criteria would be to function dually as a capping layer to protect the perovskite absorber from degradation under ambient atmosphere and heating, so materials with high stability are preferable for this application. CuSCN has been shown to be more thermally stable than the classic Spiro HTM (see Figure 21c).[500]

Tandem or Multijunction Photovoltaics. Tandem or multijunction photovoltaics consist of two stacked solar cells that selectively absorb different sections of the solar spectrum.[502] To make contact between the two layers, these devices require a tunnel p−n junction in between the two cells that can selectively transport current but let enough light through to be absorbed by the bottom cell. N-type TCOs are currently used in this application, and development of an adequate p-type transparent conductor would have important implications. This is another area where a wide-gap p-type chalcogenide could be useful, in particular for tandems with chalcogenide absorbers.

Intermediate Band Solar Cells (IBSCs). Intermediate band solar cells (IBSCs) are a creative approach to achieve efficiencies beyond the Shockley−Queisser limit.[503] Rather than optimizing the fundamental band gap for solar absorption, IBSCs intentionally introduce a deep level, midgap defect such that absorption occurs at two different wavelengths, from the CB to the deep level and from the deep level to the VB.[269] Wide-gap chalcopyrite chalcogenides have been explored as the absorbers for IBSC because of their wide, direct gap, and their ease of dopability. There have been investigations on possible IBSC dopants in chalcopyrites $CuAlS_2$, $CuGaS_2$, $AgGaSe_2$, and $AgGaTe_2$,[270,277,504] but very few device related publications could be found in literature.

4.2. Other Devices

4.2.1. Transparent Thin Film Transistors. Transparent thin film transistors (TFTs) require wide band gap semiconductors as the active/channel layer to ensure visible range transparency. An advantage of wide band gap semiconductors for TFT applications is that their intrinsic carrier concentrations

tend to be lower than for narrow band gap materials (since the former are more difficult to dope), thus achieving low "off" current. Another advantage is that the wider band gap generally results in a larger band offset, leading to better control of the carrier concentrations by the gate voltage. Simultaneously, high electronic quality of the channel's interfaces with the insulator is generally required to maintain high carrier mobilities without scattering on interfacial defects. Thus, wide band gap semiconductors with high mobility but low carrier concentrations are suitable as the active layer in transparent TFTs. N-type oxides, such as amorphous In−Ga−Zn−O (IGZO), meet these requirements and are the conventional choice of channel layer material in unipolar switching devices.[511] On the other hand, chalcogenide wide band gap semiconductors may enable bipolar devices, complementary metal oxide semiconductor (CMOS) technology and transparent circuits, since they have better propensity for p-type doping the oxides.

Figure 19c depicts a typical schematic of a transparent TFT and its band alignment under no bias. The source electrode is grounded, a fixed voltage bias is applied to the drain electrode, and the gate voltage V_g is used to control the carrier concentration in the channel, for example, the current between source and drain. For example, in an n-type TFT when V_g is above the threshold voltage V_{th}, the channel layer CBM bends down and is closer to E_F, leading to a higher concentration near the insulator/channel layer interface, called the "on" state. In contrast, if V_g is lower than V_{th}, the CBM bends upward and causes a lower carrier concentration, that is, the "off" state. Thus, the current between source and drain, I_{DS}, shows a clear on−off switching as a function of V_g. I_{DS} from p-type TFTs changes inversely compared to n-type TFTs (Figure 22). There are several p-type oxides used as TFT channels, mainly based on CuO or SnO.[7] But their performance is not as good as for their n-type counterparts, likely due the low hole mobility originating from localized oxygen 2p orbitals. By introducing a chalcogen, more covalent bonds are formed between cations and anions and a higher mobility is expected, which may lead to better performance.

There have only been a few reported attempts to implement wide-gap chalcogenides into transistors, and their high achieved mobilities offer inspiration to continue to explore this material space. For example, the fabrication of an n-type $SnS_{2−x}Se_x$ TFT by spin coating resulted in an n-type mobility greater than 10 cm^2 V$^{−1}$ s$^{−1}$, comparable to the mobility of IGZO based TFTs (~20 cm^2 V$^{−1}$ s$^{−1}$).[505,506] TFTs using p-type ZnTe as the channel layer were first reported as far back as 1967, with mobilities of 1−10 cm^2 V$^{−1}$ s$^{−1}$.[507] Since then, p-type ZnTe
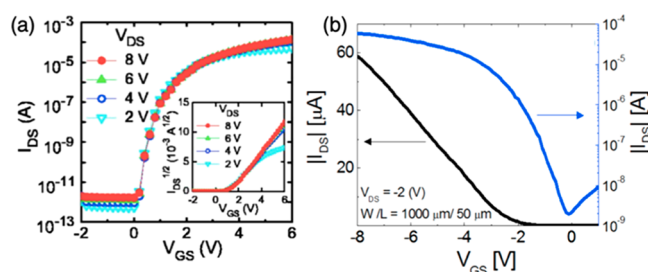

Figure 22. Example transfer curves of (a) an n-type TFT, using IGZO,[515] and (b) a p-type transparent TFT, using SnO.[516] Panel a is reproduced with permission from ref 515. Copyright 2006 the American Institute of Physics. Panel b is reproduced with permission from ref 516. Copyright 2014 IOP Publishing.
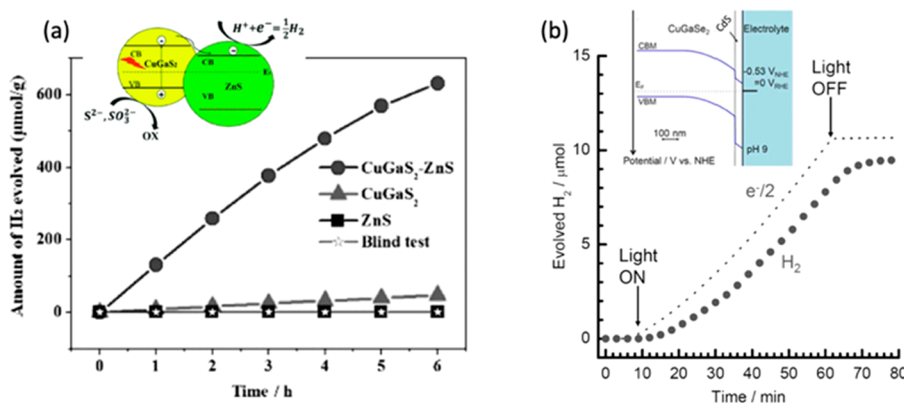
Figure 23. (a) Photocatalytic H_2 production from $CuGaS_2$:ZnS nanoheterostructure under visible light irradiation. Reproduced with permission from ref 519. Copyright 2016 The Royal Society of Chemistry. (b) Photoelectrochemical H_2 evolution from a Pt/CdS/CuGaSe$_2$ electrode (0.09 cm^2) under 300 W Xe lamp with an electrode potential of −0.1 V RHE. Reproduced with permission from ref 535. Copyright 2013 The American Chemical Society.

TFTs were integrated with n-type ZnO TFTs to form a complementary logic circuit, but the low on-current limited the on/off ratio to only ∼100.[508]

N-type CdS TFTs have also been reported to function in both accumulation and depletion mode, with a mobility of 1.25 cm^2 V^{-1} s^{-1}.[509] CdS is promising due to its high mobility >100 cm^2 V^{-1} s^{-1} and its low temperature processing for flexible electronics.[510] Additionally, n-type CdSe was reported decades ago with a mobility of 4−30 cm^2 V^{-1} s^{-1}.[511] P-type PbS TFTs have been prepared chemically, with low mobility in as-deposited devices but improvement after thermal annealing.[512,513] We note that channel layers are not limited to wide band gap semiconductors. TFTs using narrower band gap (<2 eV) semiconductors as channel layers have been reported, for example, CuInTe$_2$.[514]

4.2.2. Water Splitting Photoelectrocatalysts. Wide band gap chalcogenides have suitable properties for applications in both two types of water splitting mechanisms—as photocatalysts for photocatalytic (PC) devices and as photoelectrocatalysts for photoelectrochemical (PEC) devices—and have been extensively investigated.

Photocatalysts. Because of the relatively high CB positions compared to oxides, wide band gap chalcogenides are attractive choices as photocatalysts for "overall water splitting". The three fundamental criteria of a photocatalyst material for H_2 generation by water splitting are (1) suitable band alignment, (2) optimal band gap, and (3) resistance to corrosion in electrolyte solution. In particular, the CBM potential must be lower than 0 V vs the normal hydrogen electrode (NHE) to reduce water, and the VBM potential must be higher than 1.23 V vs NHE to oxidize water. Although the difference between water reduction and oxidation potentials is only 1.23 eV, for a single semiconductor photoelectrode the band gap must lie within the range of $1.6 < E_G < 2.4$ eV.[517] This is due to the required overpotential to drive the hydrogen evolution reaction (HER) and oxygen evolution reaction (OER) at the same time, as well as to account for different loss mechanisms in practical devices. Other desirable properties are high carrier mobility to enhance charge transfer, and good electron and hole mobilities to increase charge separation and to reduce recombination. A trade-off between crystallinity and active surface area is also of interest, as a higher degree of crystallinity improves charge transport, while a nanoporous or amorphous structure provides more active sites for catalysis.

Multinary metal chalcogenides, such as ZnS:CuInS$_2$, ZnS:CuGaS$_2$, ZnIn$_2$S$_4$, and NaInS$_2$, have been explored in search of improved photocatalytic properties in the visible spectrum.[518−521] For a visible light driven hydrogen evolution reaction, the band gaps of ZnS, CuGaS$_2$, and AgGaS$_2$ are too wide to absorb enough light. For CuInS$_2$ and AgInS$_2$, the conduction band potential is too low. Alloyed wide-gap chalcogenides with optimized compositions (e.g., CuIn$_{0.3}$Ga$_{0.7}$S$_2$ and AgIn$_{0.1}$Ga$_{0.9}$S$_2$) can balance the optimal properties of band gap and CB alignment and tune them to desirable levels.[522,523] Computational screenings have recently provided a promising avenue for searching for photocatalysts. On the basis of the first-principles analysis, Ba$_2$ZnSe$_3$, with a band gap of 2.75 eV, was predicted to be a potential candidate for visible light responsive photocatalytic water splitting.[524] Lower optical absorption of wide band gap chalcogenides in the solar spectrum can be overcome by careful tuning of morphology. CdS in nanoparticle, nanorod, and nanosheet structures exhibit high photocatalytic efficiency for hydrogen generation.[525−527] ZnS has been investigated with various metallic dopants (Ni, Cu, Pb).[528] Additionally, expensive noble metals, such as Pt, Ru, Ag, and Au, are required as cocatalysts for HER. Wide-gap chalcogenides, such as MoS$_2$ and WS$_2$, have been investigated as inexpensive substitutes.[529,530]

Other wide band gap chalcogenides remain to be investigated. Figure 24 labels the HER and OER potentials ("H$^+$/H$_2$" and "O$_2$/H$_2$O", respectively), indicating the wide-gap chalcogenides from this Review that can have application as water splitting photocatalyst. Materials with CBMs above the hydrogen reduction potential can be suitable HER catalysts, those with VBMs below the oxygen reduction potential are prospective OER catalysts, and those which meet both criteria can be applicable for overall water splitting, given that the stability and required overpotential criteria are also met.

Photoelectrocatalysts. In photoelectrochemical (PEC) water splitting, photogenerated electrons and holes split the water into hydrogen and oxygen. An external bias may be necessary based on the band alignment of the semiconductor being used. An alternative kind of water splitting device involves combining a photoelectrode with photovoltaic (PV) cells in a multijunction hybrid structure, also known as a hybrid photoelectrode and is essentially a solar cell submerged in electrolyte solution. Tandem device architecture with a wide band gap top absorber is employed to generate the required
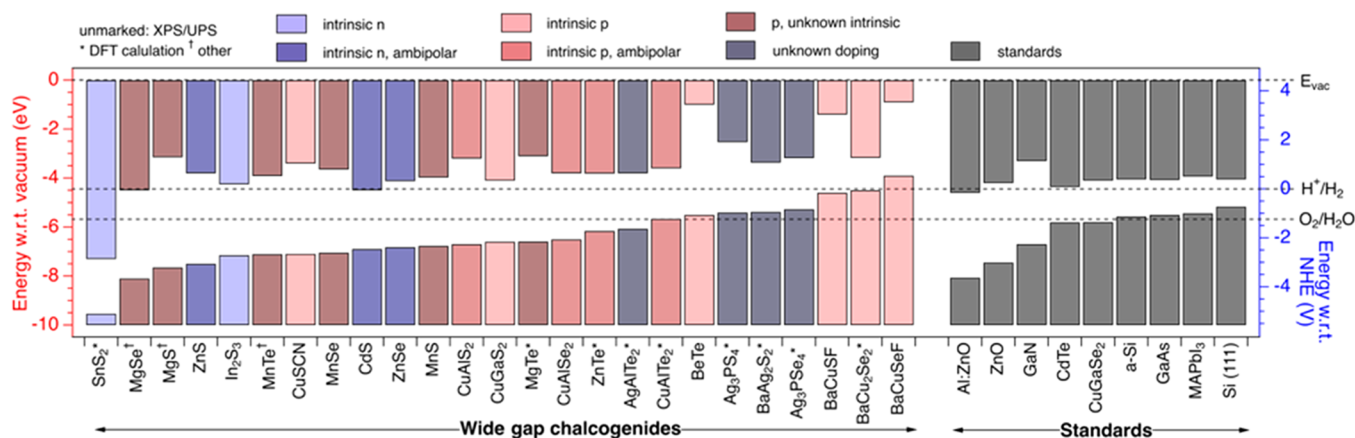
Figure 24. Literature reported band offsets of the wide band gap chalcogenides from this Review, referenced to vacuum energy E_{vac} and to the normal hydrogen electron (NHE). HER and OER potentials are labeled as "H$^+$/H$_2$" and "O$_2$/H$_2$O", respectively. Values, measurement or calculation details, and corresponding references are tabulated in the Supporting Information. We include several PV absorbers and n-type TCOs as standards (gray). All values are determined from X-ray and ultraviolet electron spectroscopy (XPS/UPS), except those with * are from DFT calculations (see Supporting Information for DFT functional used), and those with † are from another technique. Colors indicate the doping type reported in the literature. We note that modifications due to surface dipoles, band-bending, polar mismatch, and strain are not included.

potential for driving the water splitting reactions and to efficiently utilize the solar spectrum.[531]

Wide band gap chalcogenides are particularly attractive in single material systems, or as top electrodes in tandem systems, due to their high open circuit potential. With proven PV device performance, low cost, and tunable band gap, wide band gap varieties of different known chalcogenides are actively being investigated for PEC device applications. Band gaps of Cu(In,Ga)S$_2$ can span 2.05−2.45 eV based on In and Ga content, and current generation capacity up to −5.25 mA/cm^2 at saturation has been demonstrated from such photocathodes.[532] Different CuGaS$_2$ based photocathodes are also investigated (see Figure 23), which in conjunction with Co:BiVO4 photocathode, showed solar water splitting without external bias.[533,534] CdS can enhance the performance of p-type chalcogenide photocathodes by creating a p−n junction, resulting in enhanced photocurrent and onset potential. CdS-modified CuGaS$_2$ and (Ag,Cu)GaSe$_2$ electrodes have exhibited stability beyond 10 days in electrolytes and H$_2$ evolution has been demonstrated.[535,536] In$_2$S$_3$ also has similar applications and has been investigated with CuInS$_2$ photocathodes due to suitable band alignment.[537,538]

4.2.3. Diodes. *Light Emitting Diodes.* Light emitting diodes (LEDs) allow for direct conversion of electrical energy to light. A simple device structure and band diagram schematic is depicted in Figure 19e. Holes and electrons are injected via the hole transport and electron injection layer, respectively, and combine in the active layer to emit light. Some wide band gap chalcogenides are used in LEDs as transport and injection layers. Their wide band gaps enable light to escape the device, maximizing the luminescence quantum efficiency. Band alignments of the transport and injection layers with the emitting layer, as well as their high conductivities, are important interface and materials properties for this application. Here, we mention some examples of wide band gap chalcogenides used in LEDs. In addition to acting as transport layers, wide-gap chalogenides have been used as active layers too (e.g., ZnS,[539] CdS,[540] etc.).

N-type CdS has been studied as an electron transport layer in LEDs by forming a heterojunction with poly-*p*-phenylenevinylene (PPV).[541] The close band alignment between CdS and PPV, compared to that between Al and PPV, lowers the energy

barrier for electron injection. Concurrently, CdS blocks holes from flowing to the negative electrode, and helps electron injection. 2D materials such as MoS$_2$, WS$_2$, and TaS$_2$ have also been investigated as hole injection layers to replace contact materials in organic LED (OLED) applications, since these chalcogenides will not cause degradation of the organic components like ITO electrodes do.[542]

A few p-type chalcogenides have also been deployed in LEDs as hole transport or injection layers. Hole-injection barrier formed between oxygen plasma treated LaCuOSe:Mg and N,N′-diphenyl-N,N′-bis(1,1′-biphenyl)-4,4′-diamine (NPB) can be as low as 0.3 eV, approximately half that of a conventional ITO and NPB interface, indicating its potential as an efficient transparent anode for OLEDs and other organic electronic devices.[543] A chemically inert interface with a hole injection barrier of 0.11 eV was formed at the interface of BaCuSeF and ZnPc (zinc phthalocyanine), probably providing improved device performance for OLEDs and OPVs compared with ITO electrodes.[544] A p-type CuSCN layer can help balance electron and hole injection rates in n-ZnO nanorod/p-CuSCN heterojunction LEDs, enhancing efficiency of radiative recombination.[545] CuSCN is advantageous due to its wide band gap, hole-transport characteristics, and low-temperature solution-processability.[546]

In the past, ZnS has been heavily studied as a candidate active material for blue LEDs,[539,547] but these research efforts decreased with the advent of GaN-based LEDs. More recently, core/shell nanocrystal quantum dots of CdSe-ZnS[548] and CdSe-CdS,[540] among other systems, have been studied as efficient electroluminescent materials to be incorporated into light emitting diodes. The good alignment between CdSe nanocrystals and the metal electrode contributes to a low operating voltage. The color of the emission can be tuned by voltage due to quantum size effects.[549] Single-crystal p-type ZnTe can also be made into green LED using an Al-diffusion technique at the p−n junction.[550]

4.3. Band Offsets of Wide-Gap Chalcogenides

In section 3, we have discussed a large set of wide-gap chalcogenide semiconductors that could be used for device applications, and assessed their optoelectronic properties.

However, in section 4, we have seen that the materials used in solar cells, transparent transistors, etc., are limited to only a few candidates, primarily CdS, ZnS, ZnTe, In_2S_3, CuSCN, and SnS_2. What is preventing researchers from incorporating less conventional chalcogenides into these devices as contacts or active layers? First may be simply the lack of recognition of which materials are available and what their corresponding properties are. We hope to have alleviated this barrier with the discussion of potential materials and their properties in section 3, including a summary in Figure 18 and tabulated values in Tables 1−4. Second, to select an appropriate material for a device application, it is essential to understand the alignment of the valence and conduction bands at interfaces and the types of junctions that will form. This can be a somewhat trickier constraint, as alignment changes drastically depending on environment, grain orientation, interface configuration, etc.

To help assess band alignment for current and future device applications, in Figure 24, we compile and tabulate the band offset positions reported in the literature for many of the wide-gap chalcogenide semiconductors discussed previously. When available, we have reported measurements from X-ray and ultraviolet electron spectroscopy (XPS/UPS), referenced to vacuum levels. If these have been not experimentally measured, we have reported calculated offsets and denoted these cases with an asterisk suffix (see Supporting Information for level of theory and DFT functional used). Band offsets are arranged in increasing order of ionization potential, and color represents reported doping type in the literature. The gray materials on the right side of the graph are known absorbers in solar cell applications (CdTe, CIGS, Si, GaAs). References for all reported values are tabulated in the Supporting Information. The dotted lines correspond to the HER and OER potentials. We also note that uncertainties in XPS/UPS data are typically >0.1 eV, and that it is strictly a surface measurement. DFT alignments can vary by crystallographic facet orientations considered in the model and averaging scheme, so they may not robustly represent experimental alignments.

This figure illustrates that the band edges of the wide-gap chalcogenides reviewed here vary drastically. Considering the wide array of possible alloys between these compounds, as well as new chalcogenides with band edges not yet known, this gives an immense amount of possibilities for tuning band alignment to a given application of interest. For example, from comparing BeTe and ZnTe we can hypothesize that a $Be_xZn_{1-x}Te$ alloy may result in a VBM aligned with that of CdTe. In addition to the transport properties we've discussed so far, these band offsets are key first steps to understanding band bending and charge transport at the interfaces of the heterojunctions we have discussed in this section. The next steps are explicit interface simulations via slab supercell approaches and junction modeling and are covered in depth elsewhere (see section 2.5.1). Ultimately experimental band alignment measurements of real interfaces is needed to assess band positions and bending. This has been performed for many of the chalcogenide interfaces discussed in section 4[120,285,482,331,551] but not for the less studied materials.

5. SUMMARY AND OUTLOOK

In this Review, we have explored the current state of materials research in wide band gap (E_G > 2 eV) chalcogenide (Ch = S, Se, Te) semiconductors, demonstrating that this is an important space for ongoing and future research. In section 1, we introduced the existing material space of wide-gap chalcogenides

in comparison to oxides and other chemistries. In section 2, we gave an overview of computational and experimental design criteria and methodology to investigate functional wide-gap chalcogenide semiconductors. In section 3, we focused on distinctive chemical bonding and properties of chalcogenides and then covered general classes of wide band gap chalcogenide semiconductors that have been experimentally synthesized, including binary chalcogenides MCh (e.g., ZnCh), ternaries (represented by chalcopyrites, for example, $CuAlCh_2$, sulvanites, for example, Cu_3TaCh_4, α-$BaCu_2S_2$, and related structures), layered mixed-anion oxychalcogenides (e.g., LaCuOCh, BaCuChF, etc.), and touched on multinary compounds, as well as 2D chalcogenides. We focused on their respective optical properties as well as the mobilities and conductivities they have achieved (see Tables 1−3), and commented on the influence of structure and chemistry on these properties. And finally in section 4, we elaborated upon the use of wide-gap chalcogenides as functional layers in optoelectronic devices. Specifically, we looked at solar cells, thin film transistors, water splitting devices, and light emitting diodes. Most of these devices use the same simple binaries (e.g., CdS, ZnTe), so we suggest incorporation of other less common chalcogenide materials discussed in this text into these devices to address technological challenges. A conclusion from this Review is that wide band gap chalcogenide material and device spaces are still underexplored. We discussed the paradigm of materials exploration as it applies to searching for new wide-gap chalcogenide semiconductors, including several classes of computationally predicted compounds, and proposed potential future directions in new device applications of known materials.

We have discussed both n-type and p-type materials (see Figure 18 and Tables 1−4), but in particular have covered dozens of wide-gap p-type chalcogenide compounds and demonstrated how computational methods enable future discoveries. Prospective guidelines for computational discovery of new chalcogenide (semi)transparent p-type conductors are (1) to further investigate previously synthesized materials in databases for their properties, (2) to take structural analogs of oxides or other counterparts (e.g., chalcogenide delafossites or perovskites, see sections 3.4.3 and 3.4.4) to find new materials, or (3) to propose new stoichiometries and chemistries altogether (e.g., $Cs_2Zn_3Se_4$). As noted, only a portion of these materials have been calculated to be p-type dopable; only a fraction of those have specific dopants proposed, and even fewer have been synthesized with proposed dopants. As mentioned previously, tools are now available (e.g., PyCDT, PyLADA) to ease implementation of defect calculations in high throughput computational screenings. Defect calculations and corresponding experimental exploration of dopants will be essential to understand physical properties and potential optoelectronic applications. In addition to further studies of dopability, defects, and synthesizability, it is also important to consider the band offsets and alignments of these materials to justify their use in specific optoelectronic devices.

What are some next steps that can be taken through experimental materials engineering and design? First, it will be important to synthesize and characterize computationally predicted wide-gap conducting p-type materials (e.g., ZrOS, $Cs_2Zn_3Se_4$, etc.). Second, we suggest continued research into combining known compounds with complementary properties to tune desired functionality. This involves continued investigation into anion and cation alloying in the materials discussed in this Review (e.g., $Cd_{1-x}Zn_xS$, $Cu_xAg_{1-x}AlS_2$,

LaCuOS$_{1-x}$Se$_x$), and in others we have yet to discover. As shown in this Review, as well as in the n-type TCO literature, many material breakthroughs have originated from tuning properties in solid solutions and alloys. In addition, exploring composite material systems (e.g., Cu$_x$S:ZnS, section 3.1.7) and using "δ-doping" (e.g., ZnCh system, see section 3.1.1) to combine different systems could leverage the desired properties of each subsystem. Third, this Review promotes clever engineering of known chalcogenide compounds, including new processing techniques, nonequilibrium synthesis methods, postprocessing, etc., to promote carrier transport and high doping in chalcogenide host materials. Additionally, the community could engineer quasi-molecular structures, such as CuSCN, where the VBM is more disperse than the CBM, and explore band engineering by thinning materials to tune band gaps and mobilities (see section 3.6). These suggested approaches are inspired by the progress so far in the wide-gap chalcogenide community, as discussed in this Review.

Finally, this Review motivates continued investigation of interfaces of wide band gap chalcogenides and their device applications. Developing a theoretical understanding of stability, degradation, and interface modeling in chalcogenides is essential to deciding which materials can be used in devices. In particular, the band alignment of many of the systems we have discussed remain undetermined, and understanding them will be critical to tailoring materials to a particular device. Experimentally, this can be realized by synthesis of heterostructures and measurement of their interfacial band offsets. Incorporating both n-type and p-type chalcogenide materials into existing devices, as well as designing new device architectures using these unique materials, could lead to significantly higher performances and efficiencies. Together, this suite of future advances into wide band gap chalcogenide materials and devices containing such materials could be a key component in accelerating society's renewable energy transformation and enabling future technological advances.

ASSOCIATED CONTENT

Supporting Information

The Supporting Information is available free of charge at https://pubs.acs.org/doi/10.1021/acs.chemrev.9b00600.

> Atomic and molecular orbital diagram details, band gap versus lattice constant data, band offset data, other wide band gap chalcogenides, and computed wide-gap p-type chalcogenides (PDF)

AUTHOR INFORMATION

Corresponding Author

Andriy Zakutayev — *Materials Science Center, National Renewable Energy Laboratory, Golden, Colorado 80401, United States;* orcid.org/0000-0002-3054-5525; Email: andriy.zakutayev@nrel.gov

Authors

Rachel Woods-Robinson — *Materials Science Center, National Renewable Energy Laboratory, Golden, Colorado 80401, United States; Applied Science and Technology Graduate Group, University of California, Berkeley, California 94720, United States; Energy Technologies Area, Lawrence Berkeley National Laboratory, Berkeley, California 94720, United States;* orcid.org/0000-0001-5009-9510

Yanbing Han — *School of Physics and Microelectronics, Zhengzhou University, Zhengzhou 450052, China; Materials Science Center, National Renewable Energy Laboratory, Golden, Colorado 80401, United States;* orcid.org/0000-0003-1159-1005

Hanyu Zhang — *Materials Science Center, National Renewable Energy Laboratory, Golden, Colorado 80401, United States;* orcid.org/0000-0001-9942-8186

Tursun Ablekim — *Materials Science Center, National Renewable Energy Laboratory, Golden, Colorado 80401, United States;* orcid.org/0000-0002-7442-7862

Imran Khan — *Materials Science Center, National Renewable Energy Laboratory, Golden, Colorado 80401, United States;* orcid.org/0000-0002-8483-2896

Kristin A. Persson — *Department of Applied Science and Technology, University of California, Berkeley, California 94720, United States; Energy Technologies Area, Lawrence Berkeley National Laboratory, Berkeley, California 94720, United States;* orcid.org/0000-0003-2495-5509

Complete contact information is available at: https://pubs.acs.org/10.1021/acs.chemrev.9b00600

Author Contributions

[#]R.W.-R. and Y.H. contributed equally to this Review. A.Z, R.W.-R., and Y.H. conceptualized the Review and edited the manuscript. R.W.-R. and Y.H. cowrote sections 2 and 3.1−3.5. R.W.-R. wrote sections 1, 4.3, and 5 and the introductions to all sections. H.Z. wrote section 3.6. T.A. and R.W.-R. wrote section 4.1. Y.H. wrote sections 4.2.1 and 4.2.3. I.K. wrote section 4.2.2. R.W.R. created original Figures 1−4, 6, 7c, 11, 17c, 18, 19, and 24, and Y.H. created original Figures 5 and 10d. A.Z. and K.A.P. supervised the work.

Notes

The views expressed in the article do not necessarily represent the views of the DOE or the U.S. Government.
The authors declare no competing financial interest.

Biographies

Rachel Woods-Robinson is a Ph.D. Candidate at UC Berkeley, researching at the Lawrence Berkeley National Laboratory and National Renewable Energy Laboratory under Prof. Kristin Persson and Dr. Andriy Zakutayev. She received a Physics B.S. from UCLA and is an NSF Graduate Research Fellow and UC Chancellors Fellow. Her research focuses on combining computational and experimental materials discovery of p-type transparent chalcogenide semiconductors for photovoltaics. She is also the cofounder of Cycle for Science, a STEM outreach organization.

Yanbing Han is currently a researcher at Zhengzhou University. He received his Ph.D. in Physical Electronics in 2019 from Fudan University. During his Ph.D., he spent 2016−2018 at the National Renewable Energy Laboratory as a visiting student, researching chalcogenide semiconductors and stabilization of metastable polymorphs under the supervision of Dr. Andriy Zakutayev. His research interests include novel oxide and chalcogenide semiconductors and their applications.

Hanyu Zhang obtained a Ph.D. in 2016 from the School of Mechanical Engineering at Purdue University, as well as his BSME and MSME. He currently is working as a postdoctoral researcher at the National Renewable Energy Laboratory. His research focuses on investigating 2D transition metal dichalcogenides for energy conversion applications via surface modulation and phase engineering.

Tursun Ablekim is a postdoctoral research scientist within the thin film photovoltaics group at the National Renewable Energy Laboratory (NREL) in Golden, CO. He joined NREL in 2017 after receiving his Ph.D. in Materials Science and Engineering from Washington State University with Prof. Kelvin Lynn as his advisor. His graduate work was focused on synthesis and defect analysis of CdTe bulk crystals. Tursun's current research interests include II−VI semiconductor materials and their applications for energy conversion.

Imran Khan is a postdoctoral researcher at the National Renewable Energy Laboratory. His current work involves the synthesis and characterization of novel oxide and nitride thin films for photovoltaic and photoelectrochemical applications. He obtained his B.S. from Bangladesh University of Engineering & Technology. He received his M.S. and Ph.D. at the University of South Florida, focusing on the development of dye sensitized solar cells and cadmium telluride solar cells, respectively.

Kristin A. Persson is a Professor at UC Berkeley and a Senior Faculty Scientist at Lawrence Berkeley National Laboratory. She is the Director of the Materials Project (www.materialsproject.org), a leading Materials Genome Initiative program. She is an Associate Editor for Chemistry of Materials and has published over 160 papers in peer-reviewed journals. She has received the DOE Secretary of Energy's Achievement Award, the TMS Faculty Early Career Award, and she is a Kavli Fellow.

Andriy Zakutayev is a scientist at National Renewable Energy Laboratory, working on discovery and design of new materials for energy applications. To achieve these goals, he applies high-throughput combinatorial thin film methods in close iterative coupling with first-principles calculations. Dr. Zakutayev received his Ph.D. in Physics from Oregon State University, where he studied mixed-anion p-type transparent conductors.

ACKNOWLEDGMENTS

REFERENCES

(1) Wager, J. F.; Keszler, D. A.; Presley, R. E. *Transparent Electronics*; 2010.

(2) Minami, T. Transparent Conducting Oxide Semiconductors for Transparent Electrodes. *Semicond. Sci. Technol.* **2005**, *20*, S35.

(3) Rakhshani, A. E.; Makdisi, Y.; Ramazaniyan, H. A. Electronic and Optical Properties of Fluorine-Doped Tin Oxide Films. *J. Appl. Phys.* **1998**, *83*, 1049−1057.

(4) Jiang, X.; Wong, F. L.; Fung, M. K.; Lee, S. T. Aluminum-Doped Zinc Oxide Films as Transparent Conductive Electrode for Organic Light-Emitting Devices. *Appl. Phys. Lett.* **2003**, *83*, 1875−1877.

(5) Nomura, K.; Ohta, H.; Takagi, A.; Kamiya, T.; Hirano, M.; Hosono, H. Room-Temperature Fabrication of Transparent Flexible Thin-Film Transistors Using Amorphous Oxide Semiconductors. *Nature* **2004**, *432*, 488−492.

(6) Kawazoe, H.; Yasukawa, M.; Hyodo, H.; et al. P-Type Electrical Conduction in Transparent Thin Films of CuAlO2. *Nature* **1997**, *389*, 939−942.

(7) Wang, Z.; Nayak, P. K.; Caraveo-Frescas, J. A.; Alshareef, H. N. Recent Developments in P-Type Oxide Semiconductor Materials and Devices. *Adv. Mater.* **2016**, *28*, 3831−3892.

(8) Cheng, J.; Fan, D.; Wang, H.; Liu, B.; Zhang, Y.; Yan, H. Chemical Bath Deposition of Crystalline ZnS Thin Films. *Semicond. Sci. Technol.* **2003**, *18*, 676−679.

(9) Choi, J. Y.; Kim, K.-J.; Yoo, J.-B.; Kim, D. Properties of Cadmium Sulfide Thin Films Deposited by Chemical Bath Deposition with Ultrasonication. *Sol. Energy* **1998**, *64*, 41−47.

(10) Rodriguez, J.A.; Gordillo, G. Study of Electricla Properties in ZnxCd1-XS Thin Films. *Sol. Energy Mater.* **1989**, *19*, 421−431.

(11) Liu, M.; Wang, Y.; Huang, F. Optical and Electrical Properties Study on P-Type Conducting CuAlS2+x with Wide Band Gap. *Scr. Mater.* **2007**, *57*, 1133−1136.

(12) Han, Y.; Siol, S.; Zhang, Q.; Zakutayev, A. Optoelectronic Properties of Strontium and Barium Copper Sulfides Prepared by Combinatorial Sputtering. *Chem. Mater.* **2017**, *29*, 8239−8248.

(13) Newhouse, P. F.; Hersh, P. A.; Zakutayev, A.; Richard, A.; Platt, H. A. S.; Keszler, D. A.; Tate, J. Thin Film Preparation and Characterization of Wide Band Gap Cu3TaQ4 (Q = S or Se) p-Type Semiconductors. *Thin Solid Films* **2009**, *517*, 2473−2476.

(14) Hiramatsu, H.; Kamioka, H.; Ueda, K.; Ohta, H.; Kamiya, T.; Hirano, M.; Hosono, H. Opto-Electronic Properties and Light-Emitting Device Application of Widegap Layered Oxychalcogenides: LaCuOCh (Ch = Chalcogen) and La2CdO2Se2. *Phys. Status Solidi A* **2006**, *203*, 2800−2811.

(15) Hatch, S. M.; Briscoe, J.; Dunn, S. A Self-Powered ZnO-Nanorod/CuSCN UV Photodetector Exhibiting Rapid Response. *Adv. Mater.* **2013**, *25*, 867−871.

(16) Kim, K. S.; Zhao, Y.; Jang, H.; Lee, S. Y.; Kim, J. M.; Kim, K. S.; Ahn, J. H.; Kim, P.; Choi, J. Y.; Hong, B. H. Large-Scale Pattern Growth of Graphene Films for Stretchable Transparent Electrodes. *Nature* **2009**, *457*, 706−710.

(17) Che, Y.; Chen, H.; Gui, H.; Liu, J.; Liu, B.; Zhou, C. Review of Carbon Nanotube Nanoelectronics and Macroelectronics. *Semicond. Sci. Technol.* **2014**, *29*, 073001.

(18) Casady, J. B.; Johnson, R. W. Status of Silicon Carbide (SiC) as a Wide-Bandgap Semiconductor for High-Temperature Applications: A Review. *Solid-State Electron.* **1996**, *39*, 1409−1422.

(19) Mohammad, S. N.; Salvador, A. A.; Morkoç, H. Emerging Gallium Nitride Based Devices. *Proc. IEEE* **1995**, *83*, 1306.

(20) Rajan, S.; Jena, D. Gallium Nitride Electronics. *Semicond. Sci. Technol.* **2013**, *28*, 070301.

(21) Aperathitis, E.; Kambilafka, V.; Modreanu, M. Properties of N-Type ZnN Thin Films as Channel for Transparent Thin Film Transistors. *Thin Solid Films* **2009**, *518*, 1036−1039.

(22) Grundmann, M.; Schein, F. L.; Lorenz, M.; Böntgen, T.; Lenzner, J.; von Wenckstern, H. Cuprous Iodide - A p-Type Transparent Semiconductor: History and Novel Applications. *Phys. Status Solidi A* **2013**, *210*, 1671−1703.

(23) Takahashi, K.; Yoshikawa, A.; Sandhu, A. *Wide Bandgap Semiconductors* **2007**, DOI: 10.1007/978-3-540-47235-3.

(24) Zhang, K. H. L.; Xi, K.; Blamire, M. G.; Egdell, R. G. P -Type Transparent Conducting Oxides. *J. Phys.: Condens. Matter* **2016**, *28*, 383002.

(25) Delahoy, A. E.; Guo, S. Transparent Conducting Oxides for Photovoltaics. In *Handbook of Photovoltaic Science and Engineering*; Luque, A., Hegedus, S., Eds.; John Wiley & Sons, Ltd., 2011; pp 716−796.

(26) Morko, H. *Handbook of Nitride Semiconductors and Devices*; 2008.

(27) Pierson, H. O. *Handbook of Refractory Carbides and Nitrides: Properties, Characteristics, Processing, and Applications*; 1996.

(28) Allen, M. J.; Tung, V. C.; Kaner, R. B. Honeycomb Carbon: A Review of Graphene. *Chem. Rev.* **2010**, *110*, 132−145.

(29) Ruda, H. E. *Wide Gap II−VI Compounds for Opto-Electronic Applications*; Ruda, H. E., Ed.; Springer Science & Business Media, 2013.

(30) Huang, F.; Liu, M.; Yang, C. Highly Enhanced P-Type Electrical Conduction in Wide Band Gap. *Sol. Energy Mater. Sol. Cells* **2011**, *95*, 2924−2927.

(31) Hiramatsu, H.; Ueda, K.; Ohta, H.; Hirano, M.; Kamiya, T.; Hosono, H. Degenerate P-Type Conductivity in Wide-Gap LaCuOS1-XSex (X = 0−1) Epitaxial Films. *Appl. Phys. Lett.* **2003**, *82*, 1048−1050.

(32) Tate, J.; Ju, H. L.; Moon, J. C.; Zakutayev, A.; Richard, A. P.; Russell, J.; McIntyre, D. H. Origin of P-Type Conduction in Single-Crystal CuAlO2. *Phys. Rev. B: Condens. Matter Mater. Phys.* **2009**, *80*, 165206.

(33) Zunger, A. Practical Doping Principles. *Appl. Phys. Lett.* **2003**, *83*, 57.

(34) Jain, A.; Ong, S. P.; Hautier, G.; Chen, W.; Richards, W. D.; Dacek, S.; Cholia, S.; Gunter, D.; Skinner, D.; Ceder, G.; et al. Commentary: The Materials Project: A Materials Genome Approach to Accelerating Materials Innovation. *APL Mater.* **2013**, *1*, 011002.

(35) Bergerhoff, G.; Brown, I. D. *Crystallographic Databases*; International Union of Crystallography, 1987.

(36) Zagorac, D.; Müller, H.; Ruehl, S.; Zagorac, J.; Rehme, S. Recent Developments in the Inorganic Crystal Structure Database: Theoretical Crystal Structure Data and Related Features. *J. Appl. Crystallogr.* **2019**, *52*, 918−925.

(37) Morales-García, Á.; Valero, R.; Illas, F. An Empirical, yet Practical Way To Predict the Band Gap in Solids by Using Density Functional Band Structure Calculations. *J. Phys. Chem. C* **2017**, *121*, 18862−18866.

(38) Chan, M. K. Y.; Ceder, G. Efficient Band Gap Prediction for Solids. *Phys. Rev. Lett.* **2010**, *105*, 196403.

(39) Sun, W.; Bartel, C. J.; Arca, E.; Bauers, S. R.; Matthews, B.; Orvañanos, B.; Chen, B. R.; Toney, M. F.; Schelhas, L. T.; Tumas, W.; et al. A Map of the Inorganic Ternary Metal Nitrides. *Nat. Mater.* **2019**, *18*, 732−739.

(40) Bauers, S. R.; Holder, A.; Sun, W.; Melamed, C. L.; Woods-Robinson, R.; Mangum, J.; Perkins, J.; Tumas, W.; Gorman, B.; Tamboli, A.; et al. Ternary Nitride Semiconductors in the Rocksalt Crystal Structure. *Proc. Natl. Acad. Sci. U. S. A.* **2019**, *116*, 14829−14834.

(41) Han, Y.; Holder, A. M.; Siol, S.; Lany, S.; Zhang, Q.; Zakutayev, A. Zinc-Stabilized Manganese Telluride with Wurtzite Crystal Structure. *J. Phys. Chem. C* **2018**, *122*, 18769−18775.

(42) Bureau, B.; Zhang, X. H.; Smektala, F.; Adam, J. L.; Troles, J.; Ma, H. L.; Boussard-Plèdel, C.; Lucas, J.; Lucas, P.; Le Coq, D.; et al. Recent Advances in Chalcogenide Glasses. *J. Non-Cryst. Solids* **2004**, *345*, 276−283.

(43) Zakery, A.; Elliott, S. R. Optical Properties and Applications of Chalcogenide Glasses: A Review. *J. Non-Cryst. Solids* **2003**, *330*, 1−12.

(44) Curtarolo, S.; Setyawan, W.; Wang, S.; Xue, J.; Yang, K.; Taylor, R. H.; Nelson, L. J.; Hart, G. L. W.; Sanvito, S.; Buongiorno-Nardelli, M.; et al. AFLOWLIB.ORG: A Distributed Materials Properties Repository from High-Throughput Ab Initio Calculations. *Comput. Mater. Sci.* **2012**, *58*, 227−235.

(45) Lany, S. Band-Structure Calculations for the 3d Transition Metal Oxides in GW. *Phys. Rev. B: Condens. Matter Mater. Phys.* **2013**, *87*, 085112.

(46) Lany, S. Semiconducting Transition Metal Oxides. *J. Phys.: Condens. Matter* **2015**, *27*, 283203.

(47) Stevanović, V.; Lany, S.; Zhang, X.; Zunger, A. Correcting Density Functional Theory for Accurate Predictions of Compound Enthalpies of Formation: Fitted Elemental-Phase Reference Energies. *Phys. Rev. B: Condens. Matter Mater. Phys.* **2012**, *85*, 115104.

(48) Kirklin, S.; Saal, J. E.; Meredig, B.; Thompson, A.; Doak, J. W.; Aykol, M.; Rühl, S.; Wolverton, C. The Open Quantum Materials Database (OQMD): Assessing the Accuracy of DFT Formation Energies. *npj Comput. Mater.* **2015**, *1*, 15010.

(49) Woods-Robinson, R.; Broberg, D.; Faghaninia, A.; Jain, A.; Dwaraknath, S. S.; Persson, K. A. Assessing High-Throughput Descriptors for Prediction of Transparent Conductors. *Chem. Mater.* **2018**, *30*, 8375−8389.

(50) Hautier, G.; Ong, S. P.; Jain, A.; Moore, C. J.; Ceder, G. Accuracy of Density Functional Theory in Predicting Formation Energies of Ternary Oxides from Binary Oxides and Its Implication on Phase Stability. *Phys. Rev. B: Condens. Matter Mater. Phys.* **2012**, *85*, 155208.

(51) Aykol, M.; Dwaraknath, S. S.; Sun, W.; Persson, K. A. Thermodynamic Limit for Synthesis of Metastable Inorganic Materials. *Sci. Adv.* **2018**, *4*, eaaq0148.

(52) Singh, A. K.; Zhou, L.; Shinde, A.; Suram, S. K.; Montoya, J. H.; Winston, D.; Gregoire, J. M.; Persson, K. A. Electrochemical Stability of Metastable Materials. *Chem. Mater.* **2017**, *29*, 10159−10167.

(53) Patel, A. M.; Nørskov, J. K.; Persson, K. A.; Montoya, J. H. Efficient Pourbaix Diagrams of Many-Element Compounds. *Phys. Chem. Chem. Phys.* **2019**, *21*, 25323−25327.

(54) Nian, H.; Hahn, S. H.; Koo, K.-K.; Shin, E. W.; Kim, E. J. Sol−Gel Derived N-Doped ZnO Thin Films. *Mater. Lett.* **2009**, *63*, 2246−2248.

(55) Bian, J. M.; Li, X. M.; Gao, X. D.; Yu, W. D.; Chen, L. D. Deposition and Electrical Properties of N−In Codoped p-Type ZnO Films by Ultrasonic Spray Pyrolysis. *Appl. Phys. Lett.* **2004**, *84*, 541.

(56) Cao, Z. *Thin Film Growth: Physics*; Material Science and Applications, 2011.

(57) Rockett, A. *The Materials Science of Semiconductors*, 2008.

(58) Seshan, K. *Handbook of Thin Film Deposition*; William Andrew, 2018.

(59) Holloway, P. H.; Mcguire, G. E. *Handbook of Compound Semiconductors: Growth, Processing, Characterization, and Devices (Materials Science and Process Technology Series)*; 1995; Vols. *1−3*.

(60) Capper, P. *Bulk Crystal Growth of Electronic*; Optical and Optoelectronic Materials, 2010.

(61) Rocket, A. Physical Vapor Deposition. *Mater. Sci. Semicond.* **2008**, 505−572.

(62) Depla, D.; Mahieu, S.; Greene, J. E. Sputter Deposition Processes. In *Handbook of Deposition Technologies for Films and Coatings*; 2010; pp 253−296.

(63) Fujioka, H. Pulsed Laser Deposition (PLD). In *Handbook of Crystal Growth*; 2015; pp 365−397.

(64) Bishop, C. A.; Bishop, C. A. Thermal Evaporation. In *Vacuum Deposition Onto Webs, Films and Foils*; 2015; pp 301−331.

(65) Bishop, C. A. Electron Beam (E-Beam) Evaporation. In *Vacuum Deposition Onto Webs, Films and Foils*; 2015; pp 289−299.

(66) Arthur, J. R. Molecular Beam Epitaxy. *Surf. Sci.* **2002**, *500*, 189−217.

(67) Waag, A.; Heinke, H.; Scholl, S.; Becker, C. R.; Landwehr, G. Growth of MgTe and Cd1−xMgxTe Thin Films by Molecular Beam Epitaxy. *J. Cryst. Growth* **1993**, *131*, 607−611.

(68) Ritala, M.; Niinisto, J. Atomic Layer Depositioň. In *Chemical Vapor Deposition*; 2009; pp 158−206.

(69) Pakkala, A.; Putkonen, M. Atomic Layer Deposition. In *Handbook of Deposition Technologies for Films and Coatings*; 2010; pp 364−391.

(70) Thompson, A. G. MOCVD Technology for Semiconductors. *Mater. Lett.* **1997**, *30*, 255−263.

(71) Reif, R.; Kern, W. Plasma-Enhanced Chemical Vapor Deposition. In *Thin Film Processes II*; 2012; pp 525−564.

(72) Kopp Alves, A.; Bergmann, C. P.; Berutti, F. A. Spray Pyrolysis. In *Novel Synthesis and Characterization of Nanostructured Materials*; 2013; pp 23−30.

(73) Hench, L. L.; West, J. K. The Sol-Gel Process. *Chem. Rev.* **1990**, *90*, 33−72.

(74) Levy, D.; Zayat, M. *Sol-Gel Handbook* **2015**, DOI: 10.1002/9783527670819.

(75) De Guire, M. R.; Bauermann, L. P.; Parikh, H.; Bill, J. *Chemical Solution Deposition of Functional Oxide Thin Films*; 2013.

(76) Goushi, Y.; Hakuma, H.; Tabuchi, K.; Kijima, S.; Kushiya, K. Fabrication of Pentanary Cu(InGa)(SeS)2 Absorbers by Selenization and Sulfurization. *Sol. Energy Mater. Sol. Cells* **2009**, *93*, 1318−1320.

(77) Fiory, A. T. Methods in Rapid Thermal Annealing. *Proceedings of RTP 2000, Eighth International Conference on Advanced Thermal Processing of Semiconductors* 2000, 15−25.

(78) Lüdge, A.; Riemann, H.; Wünscher, M.; Behr, G.; Löser, W.; Muiznieks, A.; Cröll, A. Floating Zone Crystal Growth. In *Crystal Growth Processes Based on Capillarity*; 2010; pp 203−275.

(79) Markov, I. V. *Crystal Growth for Beginners: Fundamentals of Nucleation, Crystal Growth and Epitaxy*; World Scientific, 2003.

(80) Jurisch, M.; Eichler, S.; Bruder, M. Vertical Bridgman Growth of Binary Compound Semiconductors. In *Handbook of Crystal Growth: Bulk Crystal Growth*, 2nd ed.; 2014; Vol. 2, pp 331−372.

(81) Mannix, A. J.; Kiraly, B.; Hersam, M. C.; Guisinger, N. P. Synthesis and Chemistry of Elemental 2D Materials. *Nat. Rev. Chem.* 2017, 1, 0014.

(82) Kvick, Å.. X-Ray Diffraction, Materials Science Applications. In *Encyclopedia of Spectroscopy and Spectrometry*; 2017; pp 648−655.

(83) Stahel, W. R. The Circular Economy. *Nature* 2016, 531, 435.

(84) Li, W.; Walther, C. F. J.; Kuc, A.; Heine, T. Density Functional Theory and beyond for Band-Gap Screening: Performance for Transition-Metal Oxides and Dichalcogenides. *J. Chem. Theory Comput.* 2013, 9, 2950−2958.

(85) Pankove, J. I. *Optical Processes in Semiconductors*; Courier Corporation, 1975.

(86) Sardela, M. *Practical Materials Characterization*; 2014.

(87) Bashara, N. *Ellipsometry and Polarized Light*; North Holland: Amsterdam, 1987.

(88) Faix, O. *Fourier Transform Infrared Spectroscopy*; Springer: Berlin, 1992.

(89) Kittel, C.; Kittel, B. *Introduction to Solid State Physics*; Wiley: New York, 1986.

(90) Madsen, G. K. H.; Singh, D. J. BoltzTraP. A Code for Calculating Band-Structure Dependent Quantities. *Comput. Phys. Commun.* 2006, 175, 67−71.

(91) Sutton, A.; Fonari, C. *Effective Mass Calculator for Semiconductors*; 2012.

(92) Hautier, G.; Miglio, A.; Ceder, G.; Rignanese, G.-M.; Gonze, X. Identi Cation and Design Principles of Low Hole Effective Mass p -Type Transparent Conducting Oxides. *Nat. Commun.* 2013, 4, 2292.

(93) Zhang, D. H.; Ma, H. L. Scattering Mechanisms of Charge Carriers in Transparent Conducting Oxide Films. *Appl. Phys. A: Mater. Sci. Process.* 1996, 62, 487−492.

(94) Gantmakher, V. F.; Levinson, Y. B.; Grinberg, A. a.; Luryi, S. Carrier Scattering in Metals and Semiconductors. *Phys. Today* 1988, 41, 84.

(95) Herring, C.; Vogt, E. Transport and Deformation-Potential Theory for Many-Valley Semiconductors with Anisotropic Scattering. *Phys. Rev.* 1956, 101, 944−961.

(96) Granqvist, C. G. Transparent Conductors as Solar Energy Materials: A Panoramic Review. *Sol. Energy Mater. Sol. Cells* 2007, 91, 1529−1598.

(97) Ellmer, K. Past Achievements and Future Challenges in the Development of Optically Transparent Electrodes. *Nat. Photonics* 2012, 6, 809−817.

(98) Faghaninia, A.; Ager, J. W.; Lo, C. S. Ab Initio Electronic Transport Model with Explicit Solution to the Linearized Boltzmann Transport Equation. *Phys. Rev. B: Condens. Matter Mater. Phys.* 2015, 91, 235123.

(99) Yan, J.; Gorai, P.; Ortiz, B.; Miller, S.; Barnett, S. A.; Mason, T.; Stevanović, V.; Toberer, E. S. Material Descriptors for Predicting Thermoelectric Performance. *Energy Environ. Sci.* 2015, 8, 983−994.

(100) Mishima, Y.; Hirose, M.; Osaka, Y. Optical Determination of Mobility and Carrier Concentration in Heavily Doped Polycrystalline Silicon. *J. Appl. Phys.* 1980, 51, 1157−1159.

(101) Van De Walle, C. G.; Neugebauer, J. First-Principles Calculations for Defects and Impurities: Applications to III-Nitrides. *J. Appl. Phys.* 2004, 95, 3851−3879.

(102) Freysoldt, C.; Grabowski, B.; Hickel, T.; Neugebauer, J.; Kresse, G.; Janotti, A.; Van De Walle, C. G. First-Principles Calculations for Point Defects in Solids. *Rev. Mod. Phys.* 2014, 86, 253−305.

(103) Broberg, D.; Medasani, B.; Zimmermann, N. E. R; Yu, G.; Canning, A.; Haranczyk, M.; Asta, M.; Hautier, G. PyCDT: A Python Toolkit for Modeling Point Defects in Semiconductors and Insulators. *Comput. Phys. Commun.* 2018, 226, 165−179.

(104) Goyal, A.; Gorai, P.; Peng, H.; Lany, S.; Stevanović, V. A Computational Framework for Automation of Point Defect Calculations. *Comput. Mater. Sci.* 2017, 130, 1−9.

(105) Zakutayev, A.; Caskey, C. M.; Fioretti, A. N.; Ginley, D. S.; Vidal, J.; Stevanovic, V.; Tea, E.; Lany, S. Defect Tolerant Semiconductors for Solar Energy Conversion. *J. Phys. Chem. Lett.* 2014, 5, 1117−1125.

(106) Walsh, A.; Zunger, A. Instilling Defect Tolerance in New Compounds. *Nat. Mater.* 2017, 16, 964−967.

(107) Brandt, R. E.; Poindexter, J. R; Gorai, P.; Kurchin, R. C.; Hoye, R. L. Z.; Nienhaus, L.; Wilson, M. W. B.; Polizzotti, J. A.; Sereika, R.; Žaltauskas, R.; et al. Searching for "Defect-Tolerant" Photovoltaic Materials: Combined Theoretical and Experimental Screening. *Chem. Mater.* 2017, 29, 4667−4674.

(108) Lany, S.; Zunger, A. Dopability, Intrinsic Conductivity, and Nonstoichiometry of Transparent Conducting Oxides. *Phys. Rev. Lett.* 2007, 98, 045501.

(109) Van De Walle, C. G. Universal Alignment of Hydrogen Levels in Semiconductors and Insulators. *Phys. B* 2006, 376−377, 1−6.

(110) Schleife, A.; Fuchs, F.; Rödl, C.; Furthmüller, J.; Bechstedt, F. Branch-Point Energies and Band Discontinuities of III-Nitrides and III-/II-Oxides from Quasiparticle Band-Structure Calculations. *Appl. Phys. Lett.* 2009, 94, 012104.

(111) Sarmadian, N.; Saniz, R.; Partoens, B.; Lamoen, D. Easily Doped P-Type, Low Hole Effective Mass, Transparent Oxides. *Sci. Rep.* 2016, 6, 20446.

(112) Shi, J.; Cerqueira, T. F. T.; Cui, W.; Nogueira, F.; Botti, S.; Marques, M. A. L. High-Throughput Search of Ternary Chalcogenides for p-Type Transparent Electrodes. *Sci. Rep.* 2017, 7, 43179.

(113) Varley, J. B.; Samanta, A.; Lordi, V. Descriptor-Based Approach for the Prediction of Cation Vacancy Formation Energies and Transition Levels. *J. Phys. Chem. Lett.* 2017, 8, 5059−5063.

(114) Walker, A. V. Secondary Ion Mass Spectrometry. In *Encyclopedia of Spectroscopy and Spectrometry*; 2010; pp 2504−2510.

(115) Heinrich, K. F. J.; Newbury, D. E. Secondary Ion Mass Spectrometry. In *Proceedings of a Workshop on Secondary Ion Mass Spectrometry and Ion Microprobe Mass Analysis*; 1975; p 227.

(116) Fritsche, J.; Kraft, D.; Thißen, A.; Mayer, T.; Klein, A.; Jaegermann, W. Band Energy Diagram of CdTe Thin Film Solar Cells. *Thin Solid Films* 2002, 403−404, 252−257.

(117) Sun, W.; Ceder, G. Efficient Creation and Convergence of Surface Slabs. *Surf. Sci.* 2013, 617, 53−59.

(118) Park, J.-S.; Jung, Y.-K.; Butler, K. T.; Walsh, A. Quick-Start Guide for First-Principles Modelling of Semiconductor Interfaces. *J. Phys. Energy* 2019, 1, 016001.

(119) De Waele, S.; Lejaeghere, K.; Sluydts, M.; Cottenier, S. Error Estimates for Density-Functional Theory Predictions of Surface Energy and Work Function. *Phys. Rev. B: Condens. Matter Mater. Phys.* 2016, 94, 235418.

(120) Klein, A.; Körber, C.; Wachau, A.; Säuberlich, F.; Gassenbauer, Y.; Harvey, S. P.; Proffit, D. E.; Mason, T. O. Transparent Conducting Oxides for Photovoltaics: Manipulation of Fermi Level, Work Function and Energy Band Alignment. *Materials* 2010, 3, 4892−4914.

(121) Kotochigova, S.; Shirley, E. L.; Levine, Z. *Atomic Reference Data for Electronic Structure Calculations*; 2002.

(122) Lide, D. R. Atomic, Molecular, and Optical Physics; Ionization Potentials of Atoms and Atomic Ions. In *CRC Handbook of Chemistry and Physics*; Lide, D. R., Ed.; CRC Press: Boca Raton, FL, 2003.

(123) Oliveira, F. A. P. *Raman Spectroscopy Studies of Sn(x)Ge(1-x) and ZnO: Mn Semiconductor Solid Solutions*; Universidade do Minho, 2018.

(124) Dadlani, A. L.; Trejo, O.; Acharya, S.; Torgersen, J.; Petousis, I.; Nordlund, D.; Sarangi, R.; Schindler, P.; Prinz, F. B. Exploring the Local Electronic Structure and Geometric Arrangement of ALD Zn(O,S)

Buffer Layers Using X-Ray Absorption Spectroscopy. *J. Mater. Chem. C* **2015**, 3, 12192−12198.

(125) Fortunato, E.; Figueiredo, V.; Barquinha, P.; Elamurugu, E.; Barros, R.; Gonçalves, G.; Park, S.-H. K.; Hwang, C.-S.; Martins, R. Thin-Film Transistors Based on p-Type Cu2O Thin Films Produced at Room Temperature. *Appl. Phys. Lett.* **2010**, 96, 192102.

(126) Klein, A. Energy Band Alignment in Chalcogenide Thin Film Solar Cells from Photoelectron Spectroscopy. *J. Phys.: Condens. Matter* **2015**, 27, 134201.

(127) Vaughan, D. J.; Craig, J. R. Mineral Chemistry of Metal Sulfides. *Earth-Science Rev.* **1978**, 15, 494.

(128) Wu, X.; Coutts, T. J.; Mulligan, W. P. Properties of Transparent Conducting Oxides Formed from CdO and ZnO Alloyed with SnO2 and In2O3. *J. Vac. Sci. Technol., A* **1997**, 15, 1057−1062.

(129) Kennedy, J.; Murmu, P. P.; Gupta, P. S.; Carder, D. A.; Chong, S. V.; Leveneur, J.; Rubanov, S. Effects of Annealing on the Structural and Optical Properties of Zinc Sulfide Thin Films Deposited by Ion Beam Sputtering. *Mater. Sci. Semicond. Process.* **2014**, 26, 561−566.

(130) Han, J.; Fu, G.; Krishnakumar, V.; Liao, C.; Jaegermann, W.; Besland, M.-P. Preparation and Characterization of ZnS/CdS Bi-Layer for CdTe Solar Cell Application. *J. Phys. Chem. Solids* **2013**, 74, 1879−1883.

(131) Wang, J.; Isshiki, M. Wide-Bandgap II−VI Semiconductors: Growth and Properties. In Springer Handbook of Electronic and Photonic Materials; 2006; pp 325−342.

(132) Tate, J.; Newhouse, P. F.; Kykyneshi, R.; Hersh, P. A.; Kinney, J.; McIntyre, D. H.; Keszler, D. A. Chalcogen-Based Transparent Conductors. *Thin Solid Films* **2008**, 516, 5795−5799.

(133) Deng, Z.; Tong, L.; Flores, M.; Lin, S.; Cheng, J.-X.; Yan, H.; Liu, Y. High-Quality Manganese-Doped Zinc Sulfide Quantum Rods with Tunable Dual-Color and Multiphoton Emissions. *J. Am. Chem. Soc.* **2011**, 133, 5389−5396.

(134) Göde, F.; Gümüş, C.; Zor, M. Investigations on the Physical Properties of the Polycrystalline ZnS Thin Films Deposited by the Chemical Bath Deposition Method. *J. Cryst. Growth* **2007**, 299, 136−141.

(135) Nagamani, K.; Revathi, N.; Prathap, P.; Lingappa, Y.; Reddy, K. T. R. Al-Doped ZnS Layers Synthesized by Solution Growth Method. *Curr. Appl. Phys.* **2012**, 12, 380−384.

(136) Mohamed, S. H. Photocatalytic, Optical and Electrical Properties of Copper-Doped Zinc Sulfide Thin Films. *J. Phys. D: Appl. Phys.* **2010**, 43, 035406.

(137) Kucukomeroglu, T.; Bacaksiz, E.; Terzioglu, C.; Varilci, A. Influence of Fluorine Doping on Structural, Electrical and Optical Properties of Spray Pyrolysis ZnS Films. *Thin Solid Films* **2008**, 516, 2913−2916.

(138) Grün, M.; Storzum, A.; Hetterich, M.; Kamilli, A.; Send, W.; Walter, T.; Klingshirn, C. Chlorine Doping of Cubic CdS and ZnS Grown by Compound Source Molecular-Beam Epitaxy. *J. Cryst. Growth* **1999**, 201, 457−460.

(139) Kishimoto, S.; Kato, A.; Naito, A.; Sakamoto, Y.; Iida, S. Attempts of Homo P-n Junction Formation in ZnS by Impurity Co-Doping with Vapor Phase Epitaxy. *Phys. Status Solidi B* **2002**, 229, 391−393.

(140) Svob, L.; Thiandoume, C.; Lusson, A.; Bouanani, M.; Marfaing, Y.; Gorochov, O. P-Type Doping with N and Li Acceptors of ZnS Grown by Metalorganic Vapor Phase Epitaxy. *Appl. Phys. Lett.* **2000**, 76, 1695−1697.

(141) Sgiarovello, C.; Binggeli, N.; Baldereschi, A. Surface Morphology and Ionization Potentials of Polar Semiconductors: The Case of GaAs. *Phys. Rev. B: Condens. Matter Mater. Phys.* **2004**, 69, 35320.

(142) Swank, R. K. Surface Properties of II-VI Compounds. *Phys. Rev.* **1967**, 153, 844−849.

(143) Stevanović, V.; Lany, S.; Ginley, D. S.; Tumas, W.; Zunger, A. Assessing Capability of Semiconductors to Split Water Using Ionization Potentials and Electron Affinities Only. *Phys. Chem. Chem. Phys.* **2014**, 16, 3706−3714.

(144) Kormath Madam Raghupathy, R.; Kühne, T. D.; Felser, C.; Mirhosseini, H. Rational Design of Transparent P-Type Conducting Non-Oxide Materials from High-Throughput Calculations. *J. Mater. Chem. C* **2018**, 6, 541−549.

(145) Kalita, P. K. R.; Sarma, B. K.; Das, H. L. Structural Characterization of Vacuum Evaporated ZnSe Thin Films. *Bull. Mater. Sci.* **2000**, 23, 313−317.

(146) Ohtake, Y.; Kushiya, K.; Ichikawa, M.; Yamada, A.; Konagai, M. Polycrystalline Cu (InGa)Se2 Thin-Film Solar Cells with ZnSe Buffer Layers. *Jpn. J. Appl. Phys.* **1995**, 34, 5949.

(147) Yasuda, T.; Mitsuishi, I.; Kukimoto, H. Metalorganic Vapor Phase Epitaxy of Low-Resistivity p-Type ZnSe. *Appl. Phys. Lett.* **1988**, 52, 57−59.

(148) Ohkawa, K.; Karasawa, T.; Mitsuyu, T. Characteristics of P-Type ZnSe Layers Grown by Molecular Beam Epitaxy with Radical Doping. *Jpn. J. Appl. Phys.* **1991**, 30, L152.

(149) Niina, T.; Minato, T.; Yoneda, K. Ga-Doped ZnSe Grown by Molecular Beam Epitaxy for Blue Light Emitting Diodes. *Jpn. J. Appl. Phys.* **1982**, 21, L387.

(150) Ohkawa, K.; Mitsuyu, T.; Yamazaki, O. Characteristics of Cl-doped ZnSe Layers Grown by Molecular-beam Epitaxy. *J. Appl. Phys.* **1987**, 62, 3216−3221.

(151) Yao, T.; Ogura, M.; Matsuoka, S.; Morishita, T. High-quality ZnSe Thin Films Grown by Molecular Beam Epitaxy. *Appl. Phys. Lett.* **1983**, 43, 499−501.

(152) Rao, G. K.; Bangera, K. V.; Shivakumar, G. K. The Effect of Substrate Temperature on the Structural, Optical and Electrical Properties of Vacuum Deposited ZnTe Thin Films. *Vacuum* **2009**, 83, 1485−1488.

(153) Späth, B.; Fritsche, J.; Klein, A.; Jaegermann, W. Nitrogen Doping of ZnTe and Its Influence on CdTe/ZnTe Interfaces. *Appl. Phys. Lett.* **2007**, 90, 062112.

(154) Gessert, T. A.; Mason, A. R.; Reedy, R. C.; Matson, R.; Coutts, T. J.; Sheldon, P. Development of Rf Sputtered, Cu-Doped ZnTe for Use as a Contact Interface Layer to p-CdTe. *J. Electron. Mater.* **1995**, 24, 1443−1449.

(155) Barati, A.; Klein, A.; Jaegermann, W. Deposition and Characterization of Highly P-Type Antimony Doped ZnTe Thin Films. *Thin Solid Films* **2009**, 517, 2149−2152.

(156) Chang, J. H.; Takai, T.; Koo, B. H.; Song, J. S.; Handa, T.; Yao, T. Aluminum-Doped n-Type ZnTe Layers Grown by Molecular-Beam Epitaxy. *Appl. Phys. Lett.* **2001**, 79, 785−787.

(157) Tao, I. W.; Jurkovic, M.; Wang, W. I. Doping of ZnTe by Molecular Beam Epitaxy. *Appl. Phys. Lett.* **1994**, 64, 1848−1849.

(158) Olusola, O. I. O.; Madugu, M. L.; Dharmadasa, I. M. Growth of N-and p-Type ZnTe Semiconductors by Intrinsic Doping. *Mater. Res. Innovations* **2015**, 19, 497−502.

(159) Makhny, V. P.; Grivul, V. I. Diffusion ZnTe:Sn Layers with n-Type Conductivity. *Semiconductors* **2006**, 40, 774−775.

(160) Späth, B.; Fritsche, J.; Säuberlich, F.; Klein, A.; Jaegermann, W. Studies of Sputtered ZnTe Films as Interlayer for the CdTe Thin Film Solar Cell. *Thin Solid Films* **2005**, 480−481, 204−207.

(161) Jang, Y. J.; Jeong, I.; Lee, J.; Lee, J.; Ko, M. J.; Lee, J. S. Unbiased Sunlight-Driven Artificial Photosynthesis of Carbon Monoxide from CO 2 Using a ZnTe-Based Photocathode and a Perovskite Solar Cell in Tandem. *ACS Nano* **2016**, 10, 6980−6987.

(162) Jung, H. D.; Song, C. D.; Wang, S. Q.; Arai, K.; Wu, Y. H.; Zhu, Z.; Yao, T.; Katayama-Yoshida, H. Carrier Concentration Enhancement of P-Type ZnSe and ZnS by Codoping with Active Nitrogen and Tellurium by Using a δ-Doping Technique. *Appl. Phys. Lett.* **1997**, 70, 1143−1145.

(163) Madelung, O. I$_x$−VI$_y$ Compounds. In *Semiconductors: Data Handbook*, 3rd ed.; Berlin, 2004.

(164) Okuyama, H.; Nakano, K.; Miyajima, T.; Akimoto, K. Epitaxial Growth of ZnMgSSe on GaAs Substrate by Molecular Beam Epitaxy. *Jpn. J. Appl. Phys.* **1991**, 30, L1620.

(165) Rajashree, C.; Balu, A. R.; Nagarethinam, V. S. Enhancement in the Physical Properties of Spray Deposited Nanostructured Ternary

PbMgS Thin Films towards Optoelectronic Applications. *J. Mater. Sci.: Mater. Electron.* **2016**, *27*, 5070−5078.

(166) Pelucchi, E.; Rubini, S.; Bonanni, B.; Franciosi, A.; Zaoui, A.; Peressi, M.; Baldereschi, A.; De Salvador, D.; Berti, M.; Drigo, A.; et al. Structural and Electronic Properties of Wide Band Gap Zn$_{1−x}$Mg$_x$Se Alloys. *J. Appl. Phys.* **2004**, *95*, 4184−4192.

(167) Duman, S.; Bağcı, S.; Tütüncü, H. M.; Srivastava, G. P. First-Principles Studies of Ground-State and Dynamical Properties of MgS, MgSe, and MgTe in the Rocksalt, Zinc Blende, Wurtzite, and Nickel Arsenide Phases. *Phys. Rev. B: Condens. Matter Mater. Phys.* **2006**, *73*, 205201.

(168) Gümüş, C.; Ulutaş, C.; Ufuktepe, Y. Optical and Structural Properties of Manganese Sulfide Thin Films. *Opt. Mater. (Amsterdam, Neth.)* **2007**, *29*, 1183−1187.

(169) Wang, L.; Sivananthan, S.; Sporken, R.; Caudano, R. Interface Properties and Valence-Band Discontinuity of MnS/ZnSe Hetero-structures. *Phys. Rev. B: Condens. Matter Mater. Phys.* **1996**, *54*, 2718−2722.

(170) Pathan, H. M.; Kale, S. S.; Lokhande, C. D.; Han, S. H.; Joo, O. S. Preparation and Characterization of Amorphous Manganese Sulfide Thin Films by SILAR Method. *Mater. Res. Bull.* **2007**, *42*, 1565−1569.

(171) Heikens, H. H.; Van Bruggen, C. F.; Haas, C. Electrical Properties of α-MnS. *J. Phys. Chem. Solids* **1978**, *39*, 833−840.

(172) Pramanik, P.; Akhter, M. A.; Basu, P. K. A Solution Growth Technique for the Deposition of Manganese Sulphide Thin Film. *Thin Solid Films* **1988**, *158*, 271−275.

(173) Kim, D. S.; Lee, J. Y.; Na, C. W.; Yoon, S. W.; Kim, S. Y.; Park, J.; Jo, Y.; Jung, M. H. Synthesis and Photoluminescence of Cd-Doped α-MnS Nanowires. *J. Phys. Chem. B* **2006**, *110*, 18262−18266.

(174) Murray, R. M.; Forbes, B. C.; Heyding, R. D. The Preparation and Paramagnetic Susceptibility of β-MnSe. *Can. J. Chem.* **1972**, *50*, 4059−4061.

(175) Kan, S.; Felner, I.; Banin, U. Synthesis, Characterization, and Magnetic Properties of A-MnS Nanocrystals. *Isr. J. Chem.* **2001**, *41*, 55−62.

(176) Ishibe, I.; Nabetani, Y.; Kato, T.; Matsumoto, T. MBE Growth and RHEED Characterization of MnSe/ZnSe Superlattices on GaAs (100) Substrates. *J. Cryst. Growth* **2000**, *214*, 172−177.

(177) Sines, I. T.; Misra, R.; Schiffer, P.; Schaak, R. E. Colloidal Synthesis of Non-Equilibrium Wurtzite-Type MnSe. *Angew. Chem., Int. Ed.* **2010**, *49*, 4638−4640.

(178) Durbin, S. M.; Han, J.; O, S.; Kobayashi, M.; Menke, D. R.; Gunshor, R. L.; Fu, Q.; Pelekanos, N.; Nurmikko, A. V.; Li, D.; et al. Zinc Blende MnTe: Epilayers and Quantum Well Structures. *Appl. Phys. Lett.* **1989**, *55*, 2087−2089.

(179) Siol, S.; Han, Y.; Mangum, J.; Schulz, P.; Holder, A. M.; Klein, T. R.; van Hest, M. F. A. M.; Gorman, B.; Zakutayev, A. Stabilization of Wide Band-Gap p-Type Wurtzite MnTe Thin Films on Amorphous Substrates. *J. Mater. Chem. C* **2018**, *6*, 6297−6304.

(180) Thomas, D. G.; Hopfield, J. J.; Power, M. Excitons and the Absorption Edge of Cadmium Sulfide. *Phys. Rev.* **1960**, *119*, 570−574.

(181) Tell, B.; Damen, T.; Porto, S. Raman Effect in Cadmium Sulfide. *Phys. Rev.* **1966**, *144*, 771−774.

(182) Böer, K. W. Cadmium Sulfide Enhances Solar Cell Efficiency. In *Energy Conversion and Management*; 2011; Vol. *52*, pp 426−430.

(183) Lee, S.; Lee, E. S.; Kim, T. Y.; Cho, J. S.; Eo, Y. J.; Yun, J. H.; Cho, A. Effect of Annealing Treatment on CdS/CIGS Thin Film Solar Cells Depending on Different CdS Deposition Temperatures. *Sol. Energy Mater. Sol. Cells* **2015**, *141*, 299−308.

(184) Cortes, A.; Gómez, H.; Marotti, R. E.; Riveros, G.; Dalchiele, E. A. Grain Size Dependence of the Bandgap in Chemical Bath Deposited CdS Thin Films. *Sol. Energy Mater. Sol. Cells* **2004**, *82*, 21−34.

(185) Batlogg, B.; Jayaraman, A.; Van Cleve, J. E.; Maines, R. G. Optical Absorption, Resistivity, and Phase Transformation in CdS at High Pressure. *Phys. Rev. B: Condens. Matter Mater. Phys.* **1983**, *27*, 3920−3923.

(186) Pal, U.; Silva-González, R.; Martínez-Montes, G.; Gracia-Jiménez, M.; Vidal, M. A.; Torres, S. Optical Characterization of Vacuum Evaporated Cadmium Sulfide Films. *Thin Solid Films* **1997**, *305*, 345−350.

(187) Bicknell, R. N.; Giles, N. C.; Schetzina, J. F. Growth of High Mobility N-Type CdTe by Photoassisted Molecular Beam Epitaxy. *Appl. Phys. Lett.* **1986**, *49*, 1095−1097.

(188) Broser, I.; Broser, R.; Birkicht, E. Optical and Electrical Properties of Heavily Indium-Doped CdS around the Semiconductor-Metal Phase Transition. *J. Cryst. Growth* **1990**, *101*, 497−501.

(189) Yang, J.; Liu, R.; Huang, S.; Shao, Y.; Huang, Y.; Yu, Y. Enhanced Photocatalytic Activity and Stability of Interstitial Ga-Doped CdS: Combination of Experiment and Calculation. *Catal. Today* **2014**, *224*, 104−113.

(190) Afify, H. H.; El Zawawi, I. K.; Battisha, I. K. Photoelectronic Properties of (Cu, Fe, Al) Incorporated CdS Thin Films. *J. Mater. Sci.: Mater. Electron.* **1999**, *10*, 497−502.

(191) Wu, C.; Jie, J.; Wang, L.; Yu, Y.; Peng, Q.; Zhang, X.; Cai, J.; Guo, H.; Wu, D.; Jiang, Y. Chlorine-Doped n-Type CdS Nanowires with Enhanced Photoconductivity. *Nanotechnology* **2010**, *21*, 505203.

(192) Sebastian, P. J. P-Type CdS Thin Films Formed by in Situ Cu Doping in the Chemical Bath. *Appl. Phys. Lett.* **1993**, *62*, 2956−2958.

(193) Kashiwaba, Y.; Kanno, I.; Ikeda, T. P-Type Characteristics of Cu-Doped CdS Thin Films. *Jpn. J. Appl. Phys.* **1992**, *31*, 1170−1175.

(194) Chernow, F.; Eldridge, G.; Ruse, G.; Wåhlin, L. High Conductivity P-Type CdS. *Appl. Phys. Lett.* **1968**, *12*, 339−341.

(195) Lade, S. J.; Uplane, M. D.; Lokhande, C. D. Photo-electrochemical Properties of CdX (X = S, Se, Te) Films Electro-deposited from Aqueous and Non-Aqueous Baths. *Mater. Chem. Phys.* **2001**, *68*, 36−41.

(196) Herndon, M. K.; Gupta, A.; Kaydanov, V.; Collins, R. T. Evidence for Grain-Boundary-Assisted Diffusion of Sulfur in Poly-crystalline CdS/CdTe Heterojunctions. *Appl. Phys. Lett.* **1999**, *75*, 3503−3505.

(197) McCandless, B. E.; Sites, J. R. Cadmium Telluride Solar Cells. *Handb. Photovolt. Sci. Eng.* **2011**, 600−641.

(198) Wald, F. V. Applications of CdTe. A Review. *Rev. Phys. Appl.* **1977**, *12*, 277−290.

(199) Lingg, M.; Buecheler, S.; Tiwari, A. N. Review of CdTe$_{1−x}$Se$_x$ Thin Films in Solar Cell Applications. *Coatings* **2019**, *9*, 520.

(200) Doumi, B.; Tadjer, A.; Dahmane, F.; Djedid, A.; Yakoubi, A.; Barkat, Y.; Ould Kada, M.; Sayede, A.; Hamada, L. First-Principles Investigation of Half-Metallic Ferromagnetism in V-Doped BeS, BeSe, and BeTe. *J. Supercond. Novel Magn.* **2014**, *27*, 293−300.

(201) Mokaddem, A.; Doumi, B.; Sayede, A.; Bensaid, D.; Tadjer, A.; Boutaleb, M. Investigations of Electronic Structure and Half-Metallic Ferromagnets in Cr-Doped Zinc-Blende BeS Semiconductor. *J. Supercond. Novel Magn.* **2015**, *28*, 157−164.

(202) Yim, W. M.; Dismukes, J. P.; Stofko, E. J.; Paff, R. J. Synthesis and Some Properties of BeTe, BeSe and BeS. *J. Phys. Chem. Solids* **1972**, *33*, 501−505.

(203) Wilmers, K.; Wethkamp, T.; Esser, N.; Cobet, C.; Richter, W.; Wagner, V.; Waag, A.; Lugauer, H.; Fischer, F.; Gerhard, T.; et al. VUV Ellipsometry on Beryllium Chalcogenides. *Phys. Status Solidi B* **1999**, *215*, 15−20.

(204) Lugauer, H. J.; Fischer, F.; Litz, T.; Waag, A.; Zehnder, U.; Ossau, W.; Gerhard, T.; Landwehr, G.; Becker, C.; Kruse, R.; et al. P-Type Doping of Beryllium Chalcogenides. *Mater. Sci. Eng., B* **1997**, *43*, 88−91.

(205) Kumar, V.; Singh, N.; Kumar, R.; Lochab, S. P. Synthesis and Characterization of Bismuth Doped Calcium Sulfide Nanocrystallites. *J. Phys.: Condens. Matter* **2006**, *18*, 5029−5036.

(206) Nagata, K.; Goto, K. S. Ionic Conductivity of Solid Calcium Sulfide at 650 to 1000° C. *Metall. Trans. A* **1974**, *5*, 899−903.

(207) Hu, Y.; Zhuang, W.; Ye, H.; Zhang, S.; Fang, Y.; Huang, X. Preparation and Luminescent Properties of (Ca$_{1-x}$,Sr$_x$)S:Eu2+ Red-Emitting Phosphor for White LED. *J. Lumin.* **2005**, *111*, 139−145.

(208) Sato, M.; Imanaka, N.; Adachi, G.; Shiokawa, J. Electrical Properties of La2S3-Doped Calcium Sulfide Solid Electrolyte. *Mater. Res. Bull.* **1981**, *16*, 215−222.

(209) Saum, G. A.; Hensley, E. B. Fundamental Optical Absorption in the IIA-VIB Compounds. *Phys. Rev.* **1959**, *113*, 1019−1022.

(210) Ha, V.-A.; Yu, G.; Ricci, F.; Dahliah, D.; van Setten, M. J.; Giantomassi, M.; Rignanese, G.-M.; Hautier, G. Computationally Driven High-Throughput Identification of CaTe and Li3Sb as Promising Candidates for High-Mobility p-Type Transparent Conducting Materials. *Phys. Rev. Mater.* **2019**, *3*, 34601.

(211) Banu, I. B. S.; Rajagopalan, M.; Palanivel, B.; Kalpana, G.; Shenbagaraman, P. Structural and Electronic Properties of SrS, SrSe, and SrTe Under Pressure. *J. Low Temp. Phys.* **1998**, *112*, 211−226.

(212) Egami, A.; Onoye, T.; Narita, K. Electrical Conductivities of Alkaline Earth Sulfides. *Trans. Jpn. Inst. Met.* **1981**, *22*, 399−409.

(213) Bacaksiz, E.; Tomakin, M.; Altunbaş, M.; Parlak, M.; Çolakoğlu, T. Structural, Optical and Magnetic Properties of Cd1-XCoxS Thin Films Prepared by Spray Pyrolysis. *Phys. B* **2008**, *403*, 3740−3745.

(214) Stevanović, V.; Zakutayev, A.; Lany, S. Composition Dependence of the Band Gap and Doping in Cu_2O-Based Alloys as Predicted by an Extension of the Dilute-Defect Model. *Phys. Rev. Appl.* **2014**, *2*, 044005.

(215) Zakutayev, A.; Stevanovic, V.; Lany, S. Non-Equilibrium Alloying Controls Optoelectronic Properties in Cu_2O Thin Films for Photovoltaic Absorber Applications. *Appl. Phys. Lett.* **2015**, *106*, 123903.

(216) Woods-Robinson, R.; Xu, X.; Ager, J. W. Low-Temperature Synthesized, p-Type Transparent Conducting Materials for Photovoltaic Devices. In *2015 IEEE 42nd Photovoltaic Specialist Conference (PVSC)*; 2015; pp 1−3.

(217) Woods-Robinson, R.; Han, Y.; Mangum, J. S.; Melamed, C. L.; Gorman, B. P.; Mehta, A.; Persson, K. A.; Zakutayev, A. Combinatorial Tuning of Structural and Optoelectronic Properties in $Cu_xZn_{1−x}S$. *Matter* **2019**, *1*, 862−880.

(218) Becker, J.; Xu, X.; Woods-Robinson, R.; Campbell, C.; Lassise, M.; Ager, J.; Zhang, Y.-H. CuZnS Hole Contacts on Monocrystalline CdTe Solar Cells. *Proc. 44th PVSC* **2017**, 3410.

(219) Jiang, T.; Ozin, G. A. New Directions in Tin Sulfide Materials Chemistry. *J. Mater. Chem.* **1998**, *8*, 1099−1108.

(220) Deshpande, N. G.; Sagade, A. A.; Gudage, Y. G.; Lokhande, C. D.; Sharma, R. Growth and Characterization of Tin Disulfide (SnS2) Thin Film Deposited by Successive Ionic Layer Adsorption and Reaction (SILAR) Technique. *J. Alloys Compd.* **2007**, *436*, 421−426.

(221) Thangaraju, B.; Kaliannan, P. Spray Pyrolytic Deposition and Characterization of SnS and SnS2 Thin Films. *J. Phys. D: Appl. Phys.* **2000**, *33*, 1054.

(222) Burton, L. a.; Colombara, D.; Abellon, R. D.; Grozema, F. C.; Peter, L. M.; Savenije, T. J.; Dennler, G.; Walsh, A. Synthesis, Characterization, and Electronic Structure of Single-Crystal SnS, Sn2S3, and SnS2. *Chem. Mater.* **2013**, *25*, 4908−4916.

(223) Lucovsky, G.; Mikkelsen, J. C., Jr; Liang, W. Y.; White, R. M.; Martin, R. M. Optical Phonon Anisotropies in the Layer Crystals SnS2 and SnSe2. *Phys. Rev. B* **1976**, *14*, 1663.

(224) Wold, A.; Dwight, K. Binary Sulfides. In *Solid State Chemistry*; 1993; pp 171−197.

(225) Kim, W.; Kim, C. Optical Energy Gaps of B-In2S3 Thin Films Grown by Spray Pyrolysis. *J. Appl. Phys.* **1986**, *60*, 2631−2633.

(226) Sandoval-Paz, M. G.; Sotelo-Lerma, M.; Valenzuela-Jáuregui, J. J.; Flores-Acosta, M.; Ramírez-Bon, R. Structural and Optical Studies on Thermal-Annealed In2S3 Films Prepared by the Chemical Bath Deposition Technique. *Thin Solid Films* **2005**, *472*, 5.

(227) Barreau, N.; Marsillac, S.; Albertini, D.; Bernede, J. C. Structural, Optical and Electrical Properties of β-In2S3−3xO3x Thin Films Obtained by PVD. *Thin Solid Films* **2002**, *403−404*, 331−334.

(228) Mathew, M.; Gopinath, M.; Kartha, C. S.; P. Vijayakumar, K.; Kashiwaba, Y.; Abe, T. Tin Doping in Spray Pyrolysed Indium Sulfide Thin Films for Solar Cell Applications. *Sol. Energy* **2010**, *84*, 888−897.

(229) Lontchi, J.; Khalfallah, B.; Abaab, M. Thermal Evaporated Undoped and Na-Doped CuInS2 with Copper Contact for Photovoltaic Applications. *Int. J. Renew. Energy Res.* **2016**, *6*, 520−526.

(230) Tapia, C.; Berglund, S. P.; Friedrich, D.; Dittrich, T.; Bogdanoff, P.; Liu, Y.; Levcenko, S.; Unold, T.; Conesa, J. C.; De Lacey, A. L.; et al. Synthesis and Characterization of V-Doped β-In2S3Thin Films on FTO Substrates. *J. Phys. Chem. C* **2016**, *120*, 28753−28761.

(231) Datta, A.; Gorai, S.; Chaudhuri, S. Synthesis and Characterization of Sol-Gel Derived Mn2+ Doped In2S3 Nanocrystallites Embedded in a Silica Matrix. *J. Nanopart. Res.* **2006**, *8*, 919−926.

(232) Kauer, E.; Rabenau, A. Zur Kenntnis Des Halbleiterverhaltens Der Chalkogenide Des Aluminiums Galliums Und Indiums. *Zeitschrift Naturforsch. Tl. A* **1958**, *13*, 531.

(233) Tredgold, R. H.; Clark, A. Hopping Conduction in Gallium Selenide Single Crystals. *Solid State Commun.* **1969**, *7*, 1519−1520.

(234) Siebentritt, S. Wide Gap Chalcopyrites: Material Properties and Solar Cells. *Thin Solid Films* **2002**, *403−404*, 1−8.

(235) Siebentritt, S.; Rau, U. *Wide-Gap Chalcopyrites*; Berlin, 2006.

(236) Shay, J. L.; Wernick, J. H. *Ternary Chalcopyrite Semiconductors: Growth, Electronic Properties, and Applications: International Series of Monographs in the Science of the Solid State*, Vol. 7.; Elsevier, 2017.

(237) Pamplin, B. R.; Kiyosawa, T.; Masumoto, K. Ternary Chalcopyrite Compounds. *Prog. Cryst. Growth Charact.* **1979**, *1*, 331−387.

(238) Jaffe, J. E.; Zunger, A. Theory of the Band-Gap Anomaly in ABC2 Chalcopyrite Semiconductors. *Phys. Rev. B: Condens. Matter Mater. Phys.* **1984**, *29*, 1882−1906.

(239) Zhang, Y.; Xi, L.; Wang, Y.; Zhang, J.; Zhang, P.; Zhang, W. Electronic Properties of Energy Harvesting Cu-Chalcogenides: P-d Hybridization and d-Electron Localization. *Comput. Mater. Sci.* **2015**, *108*, 239−249.

(240) Zhang, S. B.; Wei, S.-H.; Zunger, A.; Katayama-Yoshida, H. Defect Physics of the CuInSe2 Chalcopyrite Semiconductor. *Phys. Rev. B: Condens. Matter Mater. Phys.* **1998**, *57*, 9642.

(241) Persson, C.; Zunger, A. Compositionally Induced Valence-Band Offset at the Grain Boundary of Polycrystalline Chalcopyrites Creates a Hole Barrier. *Appl. Phys. Lett.* **2005**, *87*, 211904.

(242) Aksenov, I. A.; Makovetskaya, L. A.; Savchuk, V. A. Electrical Properties of Cadmium and Zinc Doped $CuAlS_2$. *Phys. Stat. Sol. (a)* **1988**, *108*, K63−65.

(243) Morita, Y.; Narusawa, T.; et al. Related Content Characterization of CuAlS2 Films Grown by Molecular Beam Epitaxy. *Jpn. J. Appl. Phys.* **1992**, *31*, L1396.

(244) Ghosh, B.; Pradhan, S. K. One-Step Fastest Method of Nanocrystalline CuAlS2 Chalcopyrite Synthesis, and Its Nanostructure Characterization. *J. Nanopart. Res.* **2011**, *13*, 2343−2350.

(245) Caglar, M.; Ilican, S.; Caglar, Y. Structural, Morphological and Optical Properties of CuAlS2 Films Deposited by Spray Pyrolysis Method. *Opt. Commun.* **2008**, *281*, 1615−1624.

(246) Shirakata, S.; Aksenov, I.; Sato, K.; Isomura, S. Photoluminescence Studies in CuAlS2 Crystals. *Jpn. J. Appl. Phys.* **1992**, *31*, L1071−L1074.

(247) Vahidshad, Y.; Ghasemzadeh, R.; Zad, A. I.; Mirkazemi, S. M. Solvothermal Synthesis of $CuMS_2$ (M = Al, In, Fe) Nanoparticles and Effect of Coordinating Solvent on the Crystalline Structure. *Sci. Iran. Trans. F Nanotechnol.* **2014**, *21*, 2468−2479.

(248) Liu, M. L.; Huang, F. Q.; Chen, L. D. P-Type Transparent Conductivity of Cu1-XAlS2 (x = 0 ∼ 0.08). *Key Eng. Mater.* **2008**, *368−372*, 666−668.

(249) Banguero, E.; Gordillo, G. Related Content CuAlS2 Thin-Films Prepared by Sulfurization of Metallic Precursors and Their Properties. *Jpn. J. Appl. Phys.* **2004**, *31*, L1396.

(250) Duclaux, L.; Donsanti, F.; Vidal, J.; Bouttemy, M.; Schneider, N.; Naghavi, N. Simulation and Growing Study of Cu-Al-S Thin Films Deposited by Atomic Layer Deposition. *Thin Solid Films* **2015**, *594*, 232−237.

(251) Huang, D.; Zhao, Y.; Tang, W.; Liang, X.; Zhou, W.; Li, C.; Yao, C.; Guo, J. Understanding the High P-Type Conductivity in Cu-Excess CuAlS2: A First-Principles Study. *Appl. Phys. Express* **2016**, *9*, 031202.

(252) Liu, M.-L.; Huang, F.-Q.; Chen, L.-D.; Wang, Y.-M.; Wang, Y.-H.; Li, G.-F.; Zhang, Q. P -Type Transparent Conductor : Zn-Doped CuAlS 2. *Appl. Phys. Lett.* **2007**, *90*, 072109.

(253) Liu, M.-L.; Huang, F.-Q.; Chen, L.-D. P-Type Electrical Conduction and Wide Optical Band Gap in Mg Doped CuAlS$_2$. *Scr. Mater.* **2008**, *58*, 1002−1005.

(254) Bettini, M. Reflection Measurements with Polarization Modulation: A Method to Investigate Bandgaps in Birefringent Materials like I-III-VI2 Chalcopyrite Compounds. *Solid State Commun.* **1973**, *13*, 599−602.

(255) Reddy, Y. B. K.; Raja, V. S. Effect of Cu/Al Ratio on the Properties of CuAlSe$_2$ Thin Films Prepared by Co-Evaporation. *Mater. Chem. Phys.* **2006**, *100*, 152−157.

(256) Jin, M.; Min, S.; Mei-zhen, G.; Yue-gang, C.; Yan-hua, W.; Ramanujam, J.; Singh, U. P.; Rubel, O.; Darbandi, A. Related Content Preparation and Properties of Single Crystal CuAlSe$_2$ Film. *Jpn. J. Appl. Phys.* **1991**, *30*, L1238.

(257) Barkat, L.; Morsli, M.; Amory, C.; Marsillac, S.; Khelil, A.; Bernede, J.C.; El Moctar, C. Study on the Fabrication of N-Type CuAlSe$_2$ Thin Films. *Thin Solid Films* **2003**, *431-432*, 99−104.

(258) Gombia, E.; Leccabue, F.; Pelosi, C. The CVD Growth of CuAlTe2 Single Crystals. *Mater. Lett.* **1984**, *2*, 429−431.

(259) Benchouk, K.; Benseddik, E.; El Moctar, C. O.; Bernède, J. C.; Marsillac, S.; Pouzet, J.; Khellil, A. New Buffer Layers, Large Band Gap Ternary Compounds: CuAlTe$_2$. *Eur. Phys. J.: Appl. Phys.* **2000**, *10*, 9−14.

(260) El Assali, K.; Chahboun, N.; Bekkay, T.; Ameziane, E. L.; Boustani, M.; Khiara, A. Electrical Properties of CuAlTe$_2$ Thin Films and MoCuAlTe$_2$ Contact Prepared by Rf Sputtering. *Sol. Energy Mater. Sol. Cells* **1995**, *39*, 33−38.

(261) Chahboun, N.; El Assali, K.; Khiara, A.; Ameziane, E. L.; Bekkay, T. Growth of CuAlTe$_2$ Films by RF Sputtering. *Sol. Energy Mater. Sol. Cells* **1994**, *32*, 213−218.

(262) Bernède, J. C.; Zoaeter, M.; Marsillak, S.; Barreauk, N.; Oukld El Moctark, C.; Benchouk, K.; Khelil, A. Cd Free Buffer Layers for Solar Cells. 2000. *Mediterr. Conf. Environ. Solar, COMPLES 2000* **2000**, *00*, 13−16.

(263) Guillén, C.; Herrero, J. CuInS$_2$ and CuGaS$_2$ Thin Films Grown by Modulated Flux Deposition with Various Cu Contents. *Phys. Status Solidi A* **2006**, *203*, 2438−2443.

(264) Prabukanthan, P.; Dhanasekaran, R. Growth of CuGaS$_2$ Single Crystals by Chemical Vapor Transport and Characterization. *Cryst. Growth Des.* **2007**, *7*, 618−623.

(265) Yu, P. W.; Downing, D. L.; Park, Y. S. Electrical Properties of CuGaS$_2$ Single Crystals. *J. Appl. Phys.* **1974**, *45*, 5283−5288.

(266) Jeong, W.; Park, G. Structural and Electrical Properties of CuGaS$_2$ Thin Films by Electron Beam Evaporation. *Sol. Energy Mater. Sol. Cells* **2003**, *75*, 93−100.

(267) Abdullaev, N. A.; Aliguliyeva, K. V.; Aliyeva, L. N.; Qasimoglu, I.; Kerimova, T. G. Low-Temperature Conductivity in CuGaS$_2$ Single Crystals. *Semiconductors* **2015**, *49*, 428−431.

(268) Bailey, C. L.; Liborio, L.; Mallia, G.; Tomić, S.; Harrison, N. M. Defect Physics of CuGaS$_2$. *Phys. Rev. B: Condens. Matter Mater. Phys.* **2010**, *81*, 205214.

(269) Castellanos Águila, J. E.; Palacios, P.; Conesa, J. C.; Arriaga, J.; Wahnón, P. Theoretical Band Alignment in an Intermediate Band Chalcopyrite Based Material. *Appl. Surf. Sci.* **2017**, *424*, 132−136.

(270) Marsen, B.; Klemz, S.; Unold, T.; Schock, H. W. Investigation of the Sub-Bandgap Photoresponse in CuGaS$_2$: Fe for Intermediate Band Solar Cells. In *Progress in Photovoltaics: Research and Applications*; 2012; Vol. 20, pp 625−629.

(271) León, M.; Dìaz, R.; Rueda, F.; Berghol, M. A Comparative Study of Optical, Electrical and Structural Properties of CuGaSe2 and CuGaTe2 Thin Films. *Sol. Energy Mater. Sol. Cells* **1992**, *26*, 295−307.

(272) Kormath Madam Raghupathy, R.; Wiebeler, H.; Kühne, T. D.; Felser, C.; Mirhosseini, H. Database Screening of Ternary Chalcogenides for P-Type Transparent Conductors. *Chem. Mater.* **2018**, *30*, 6794−6800.

(273) Ho, C.; Pan, C. Optical Behavior and Structural Property of CuAlS$_2$ and AgAlS$_2$ Wide-Bandgap Chalcopyrites. *Appl. Opt.* **2014**, *53*, E7−13.

(274) Ho, C.; Pan, C. Surface Sensing Behavior and Band Edge Properties of AgAlS$_2$: Experimental Observations in Optical, Chemical, and Thermoreflectance Spectroscopy. *AIP Adv.* **2012**, *2*, 022123.

(275) Hellstrom, E. E.; Huggins, R. A. Silver Ionic and Electronic Conductivity in Ag9GaS6, Ag9AlS6, AgGaS2, AgAlS2, and AgAl5S8. *J. Solid State Chem.* **1980**, *35*, 207−214.

(276) Hussien, B. H. Study of Some Structural and Optical Properties of AgAlSe$_2$ Thin Films. *Ibn AL- Haitham Journal For Pure and Applied Science* **2016**, *29*, 41−51.

(277) Jiang, J.; Cen, X.; Dong, W.; Zhou, W.; Liang, X.; Liu, Y.; Guo, J.; Huang, D. Theoretical Design of the Absorber for Intermediate Band Solar Cells from Group-IV (Si, Ge, and Sn)-Doped AgAlSe2. *Phys. Status Solidi B* **2018**, *255*, 1800031.

(278) Uruno, A.; Usui, A.; Kobayashi, M. Structural and Optical Properties of AgAlTe2 Layers Grown on Sapphire Substrates by Closed Space Sublimation Method. *J. Appl. Phys.* **2014**, *116*, 183504.

(279) Karaagac, H.; Parlak, M. The Investigation of Structural, Electrical, and Optical Properties of Thermal Evaporated AgGaS2 Thin Films. *Thin Solid Films* **2011**, *519*, 2055−2061.

(280) Tell, B.; Shay, J. L.; Kasper, H. M. Room-Temperature Electrical Properties of Tenary I-III-VI2 Semiconductors. *J. Appl. Phys.* **1972**, *43*, 2469−2470.

(281) Yu, P. W.; Manthuruthil, J.; Park, Y. S. Some Electrical Properties of AgGaS$_2$. *J. Appl. Phys.* **1974**, *45*, 3694−3696.

(282) Campe, H. v. Growth and Electrical Properties of AgGaS$_2$ Thin Films. *Thin Solid Films* **1984**, *111*, 17−35.

(283) Bairamov, B. H.; Rud', V. Y.; Rud', Y. V. Properties of Dopants in ZnGeP$_2$, CdGeAs$_2$, AgGaS$_2$ and AgGaSe$_2$. *MRS Bull.* **1998**, *23*, 41−44.

(284) Korzun, B. V.; Fadzeyeva, A. A.; Bente, K.; Schmitz, W.; Kommichau, G. Phase Correlations in the CuAlSe$_2$-CuAlTe$_2$ System. *Phys. Status Solidi B* **2005**, *242*, 1581−1587.

(285) Wei, S. H.; Zunger, A. Band Offsets and Optical Bowings of Chalcopyrites and Zn-Based II-VI Alloys. *J. Appl. Phys.* **1995**, *78*, 3846−3856.

(286) Niiyama, Y.; Watanabe, M. BeMgZnSe-Based Ultraviolet Lasers. *Semicond. Sci. Technol.* **2005**, *20*, 1187−1197.

(287) Ogawa, A.; Sudo, R.; Gupta, A.; Shirakata, S.; Chichibu, S.; Matsumoto, S.; Isomura, S. Preparation and Characterization of Cu(Al, Ga)(s, Se)$_2$ Penternary Alloys. *Jpn. J. Appl. Phys.* **1993**, *32*, 588−589.

(288) Ahmad, S. M. Study of Structural and Optical Properties of. *Optik* **2016**, *127*, 10004−10013.

(289) Choi, I.-H.; Eom, S.-H.; Yu, P. Y. The Optical and Vibrational Properties of the Quaternary Chalcopyrite Semiconductor Alloy Ag$_x$Cu$_{1-x}$GaS$_2$. *J. Appl. Phys.* **2000**, *87*, 3815.

(290) Brik, M. G.; Ma, C. G. Tailoring the Electronic and Elastic Properties by Varying the Composition of the CuGa$_{1-x}$Al$_x$S$_2$ Chalcopyrite Semiconductor. *J. Phys. D: Appl. Phys.* **2013**, *46*, 285304.

(291) Tsuboi, N.; Kobayashi, S.; Kaneko, F.; Maruyama, T. Dependence of Energy Gap on x in CuAl$_x$Ga$_{1-x}$S$_2$ Mixed Crystal System. *Jpn. J. Appl. Phys.* **1988**, *27*, 972.

(292) Wen-Chen, Z.; Shao-Yi, W.; Bei-Jun, Z.; Shi-Fu, Z. Substitutional Sites of Co^{2+} ions in CuGa$_{1-x}$Al$_x$Se$_2$:Co$_2$$^+$ Crystals. *J. Phys. Chem. Solids* **2002**, *63*, 895−897.

(293) Jin, M. S.; Kim, W. T.; Yoon, C. S. Optical Properties of Undoped and Co-Doped CuGa$_{1-x}$Al$_x$Se$_2$ Single Crystals. *J. Phys. Chem. Solids* **1993**, *54*, 1509−1513.

(294) Reshak, A. H. Transport Properties of Mixed CuAl(S$_{1-x}$Se$_x$)$_2$ as Promising Thermoelectric Crystalline Materials. *J. Phys. Chem. Solids* **2015**, *78*, 46−52.

(295) Ning, C.-Z.; Dou, L.; Yang, P. Bandgap Engineering in Semiconductor Alloy Nanomaterials with Widely Tunable Compositions. *Nat. Rev. Mater.* **2017**, *2*, 17070.

(296) Iglesias, J. E.; Pachali, K. E.; Steinfink, H. Structural Chemistry of Ba$_2$CdS$_3$, Ba$_2$CdSe$_3$, BaCdS$_2$, BaCu$_2$S$_2$ and BaCu$_2$Se$_2$. *J. Solid State Chem.* **1974**, *9*, 6−14.

(297) Kurosaki, K.; Uneda, H.; Muta, H.; Yamanaka, S. Electrical Properties of β-BaCu$_2$S$_2$. *J. Alloys Compd.* **2004**, *385*, 312−315.

(298) Kurosaki, K.; Uneda, H.; Muta, H.; Yamanaka, S. Thermoelectric Properties of β-BaCu$_2$S$_2$. *J. Alloys Compd.* **2005**, *388*, 122−125.

(299) Park, S.; Keszler, D. A.; Valencia, M. M.; Hoffman, R. L.; Bender, J. P.; Wager, J. F. Transparent P-Type Conducting BaCu$_2$S$_2$ Films. *Appl. Phys. Lett.* **2002**, *80*, 4393−4394.

(300) Wang, Y.; Liu, M.; Huang, F.; Chen, L.; Li, H.; Lin, X.; Wang, W.; Xia, Y. Solution-Processed p-Type Transparent Conducting BaCu$_2$S$_2$ Thin Film. *Chem. Mater.* **2007**, *19*, 3102−3104.

(301) Liu, G. B.; Wang, X. Q.; Kuang, X. J.; He, A L. First-Principles Study on the Electronic Properties of BaCu$_2$S$_2$. *Phys. B* **2010**, *405*, 4582−4585.

(302) Krishnapriyan, A.; Barton, P. T.; Miao, M.; Seshadri, R. First-Principles Study of Band Alignments in the p-Type Hosts BaM2 × 2 (M = Cu, Ag; X = S, Se). *J. Phys.: Condens. Matter* **2014**, *26*, 155802.

(303) Ohtani, T.; Takeuchi, H.; Koh, K.; Kaneko, T. Electrical Properties and Phase Transitions of TlCu$_3$S$_2$ and BaCu$_2$S$_2$. *J. Alloys Compd.* **2001**, *317*, 201−207.

(304) McGuire, M. a.; May, A. F.; Singh, D. J.; Du, M.-H.; Jellison, G. E. Transport and Optical Properties of Heavily Hole-Doped Semiconductors BaCu$_2$Se$_2$ and BaCu$_2$Te$_2$. *J. Solid State Chem.* **2011**, *184*, 2744−2750.

(305) Kehoe, A. B.; Scanlon, O.; Watson, G. W. The Electronic Structure of Sulvanite Structured Cu$_3$MCh$_4$ (M = V, Nb, Ta; Ch = S, Se, Te): Prospects for Optoelectronic Applications. *J. Mater. Chem. C* **2015**, *3*, 12236−12244.

(306) Ricci, F.; Chen, W.; Aydemir, U.; Snyder, G. J.; Rignanese, G.-M.; Jain, A.; Hautier, G. An Ab Initio Electronic Transport Database for Inorganic Materials. *Sci. Data* **2017**, *4*, 170085.

(307) Hersh, P. A. *Wide Band Gap Semiconductors and Insulators: Synthesis, Processing and Characterization*; 2007.

(308) Chen, E. M.; Stoyko, S. S.; Aitken, J. A.; Poudeu, P. F. P. Tuning the Optical, Electronic and Thermal Properties of Cu$_3$NbS$_4$-XSe$_x$ through Chemical Substitution. *Inorg. Chem. Front.* **2017**, *4*, 1493−1500.

(309) Lu, Y.-J.; Ibers, J. A. Synthesis and Characterization of Cu3NbSe4 and KCu2TaSe4. *J. Solid State Chem.* **1993**, *107*, 58−62.

(310) Bramer-Escamilla, W.; Grima-Gallardo, P.; Silva, P.et al. Development and Characterization of a P-n Junction of Si-Cu$_3$NbSe$_4$. *Acta Científica Venezolana***2015**, *66*, 66−71.

(311) Arribart, H.; Sapoval, B.; Gorochov, O.; LeNagard, N. Fast Ion Transport at Room Temperature in the Mixed Conductor Cu3VS4. *Solid State Commun.* **1978**, *26*, 435−439.

(312) Petritis, D.; Martinez, G.; Levy-Clement, C.; Gorochov, O. Investigation of the Vibronic Properties of Cu3VS4, Cu3NbS4, and Cu3TaS4 Compounds. *Phys. Rev. B: Condens. Matter Mater. Phys.* **1981**, *23*, 6773.

(313) Pfitzner, A.; Reiser, S. Refinement of the Crystal Structures of Cu3PS4 and Cu3SbS4 and a Comment on Normal Tetrahedral Structures. *Z. Kristallogr. - Cryst. Mater.* **2002**, *217*, 51−54.

(314) Marzik, J. V.; Hsieh, A. K.; Dwight, K.; Wold, A. Photoelectronic Properties of Cu3PS4 and Cu3PS3Se Single Crystals. *J. Solid State Chem.* **1983**, *49*, 43−50.

(315) Ma, Z.; Yi, Z.; Sun, J.; Wu, K. Electronic and Photocatalytic Properties of Ag3PC4VI (C= O, S, Se): A Systemic Hybrid DFT Study. *J. Phys. Chem. C* **2012**, *116*, 25074−25080.

(316) Nagarajan, R.; Draeseke, A. D.; Sleight, A. W.; Tate, J. P-Type Conductivity in CuCr1-XMgxO2 Films and Powders. *J. Appl. Phys.* **2001**, *89*, 8022−8025.

(317) Yanagi, H.; Hase, T.; Ibuki, S.; Ueda, K.; Hosono, H. Bipolarity in Electrical Conduction of Transparent Oxide Semiconductor Delafossite Structure Bipolarity in Electrical Conduction of Transparent Oxide Semiconductor CuInO 2 with Delafossite Structure. *Appl. Phys. Lett.* **2001**, *78*, 1583−1585.

(318) Shannon, R. D.; Gillson, J. L.; Bouchard, R. J. Single Crystal Synthesis and Electrical Properties of CdSnO3, Cd2SnO4, In2TeO6 and Cdln2O4. *J. Phys. Chem. Solids* **1977**, *38*, 877−881.

(319) Kim, H. J.; Kim, U.; Kim, H. M.; Kim, T. H.; Mun, H. S.; Jeon, B.-G.; Hong, K. T.; Lee, W.-J.; Ju, C.; Kimy, K. H.; et al. High Mobility

(320) Huang, W.; Nechache, R.; Li, S.; Chaker, M.; Rosei, F. Electrical and Optical Properties of Transparent Conducting p -Type SrTiO 3 Thin Films. *J. Am. Ceram. Soc.* **2016**, *99*, 226−233.

(321) Zhang, K. H. L.; Du, Y.; Papadogianni, A.; Bierwagen, O.; Sallis, S.; Piper, L. F. J.; Bowden, M. E.; Shutthanandan, V.; Sushko, P. V.; Chambers, S. a. Perovskite Sr-Doped LaCrO3 as a New p-Type Transparent Conducting Oxide. *Adv. Mater.* **2015**, *27*, 5191−5195.

(322) Kuhar, K.; Crovetto, A.; Pandey, M.; Thygesen, K. S.; Seger, B.; Vesborg, P. C. K.; Hansen, O.; Chorkendorff, I.; Jacobsen, K. W. Sulfide Perovskites for Solar Energy Conversion Applications: Computational Screening and Synthesis of the Selected Compound LaYS $_3$. *Energy Environ. Sci.* **2017**, *10*, 2579−2593.

(323) Androulakis, J.; Peter, S. C.; Li, H.; Malliakas, C. D.; Peters, J. A.; Liu, Z.; Wessels, B. W.; Song, J.; Jin, H.; Freeman, A. J.; et al. *Dimensional Reduction : A Design Tool for New Radiation Detection Materials*; 2011; pp 4163−4167.

(324) Shi, H.; Saparov, B.; Singh, D. J.; Sefat, A. S.; Du, M.-H. Ternary Chalcogenides Cs2Zn3Se4 and Cs2Zn3Te4: Potential p-Type Transparent Conducting Materials. *Phys. Rev. B: Condens. Matter Mater. Phys.* **2014**, *90*, 184104.

(325) Johnsen, S.; Peter, S. C.; Nguyen, S. L.; Song, J.; Jin, H.; Freeman, A. J.; Kanatzidis, M. G. Tl$_2$Hg$_3$Q$_4$ (Q = S, Se, and Te): High-Density Wide-Band-Gap Semiconductors. *Chem. Mater.* **2011**, *23*, 4375−4383.

(326) Kehoe, A. B.; Temple, D. J.; Watson, G. W.; Scanlon, D. O. Cu3MCh3 (M = Sb, Bi; Ch = S, Se) as Candidate Solar Cell Absorbers: Insights from Theory. *Phys. Chem. Chem. Phys.* **2013**, *15*, 15477.

(327) Wang, M. X.; Yue, G. H.; Fan, X. Y.; Yan, P. X. Properties and Characterization of Cu3SbS3 Nanowires Synthesized by Solvothermal Route. *J. Cryst. Growth* **2008**, *310*, 3062−3066.

(328) Hiramatsu, H.; Ueda, K.; Takafuji, K.; Ohta, H.; Hirano, M.; Kamiya, T.; Hosono, H. Degenerate Electrical Conductive and Excitonic Photoluminescence Properties of Epitaxial Films of Wide Gap P-Type Layered Oxychalcogenides, LnCuOCh (Ln= La, Pr and Nd; Ch= S or Se). *Appl. Phys. A: Mater. Sci. Process.* **2004**, *79*, 1521−1523.

(329) Ueda, K.; Inoue, S.; Hirose, S.; Kawazoe, H.; Hosono, H. Transparent P-Type Semiconductor: LaCuOS Layered Oxysulfide. *Appl. Phys. Lett.* **2000**, *77*, 2701−2703.

(330) Hiramatsu, H.; Kamioka, H.; Ueda, K.; Hirano, M.; Hosono, H. Electrical and Photonic Functions Originating from Low-Dimensional Structures in Wide-Gap Semiconductors LnCuOCh (Ln = Lanthanide, Ch = Chalcogen): A Review. *J. Ceram. Soc. Japan* **2005**, *113*, 10−16.

(331) Ueda, K.; Hosono, H. Band Gap Engineering, Band Edge Emission, and p-Type Conductivity in Wide-Gap LaCuOS1−xSex Oxychalcogenides. *J. Appl. Phys.* **2002**, *91*, 4768−4770.

(332) Scanlon, D. O.; Buckeridge, J.; Catlow, C. R. A.; Watson, G. W. Understanding Doping Anomalies in Degenerate P-Type Semiconductor LaCuOSe. *J. Mater. Chem. C* **2014**, *2*, 3429−3438.

(333) Hiramatsu, H.; Ueda, K.; Ohta, H.; Hirano, M.; Kamiya, T.; Hosono, H. Wide Gap P-Type Degenerate Semiconductor: Mg-Doped LaCuOSe. *Thin Solid Films* **2003**, *445*, 304−308.

(334) Hiramatsu, H.; Kamiya, T.; Tohei, T.; Ikenaga, E.; Mizoguchi, T.; Ikuhara, Y.; Kobayashi, K.; Hosono, H. Origins of Hole Doping and Relevant Optoelectronic Properties of Wide Gap P-Type Semiconductor, LaCuOSe. *J. Am. Chem. Soc.* **2010**, *132*, 15060−15067.

(335) Ueda, K.; Hosono, H.; Hamada, N. Energy Band Structure of LaCuOCh (Ch= S, Se and Te) Calculated by the Full-Potential Linearized Augmented Plane-Wave Method. *J. Phys.: Condens. Matter* **2004**, *16*, 5179.

(336) Liu, M. L.; Wu, L. B.; Huang, F. Q.; Chen, L. D.; Ibers, J. A. Syntheses, Crystal and Electronic Structure, and Some Optical and Transport Properties of LnCuOTe (Ln= La, Ce, Nd). *J. Solid State Chem.* **2007**, *180*, 62−69.

(337) Ijjaali, I.; Haynes, C. L.; McFarland, A. D.; Van Duyne, R. P.; Ibers, J. A. Synthesis, Structure, and Optical Properties of the New

Lanthanum Copper Oxysulfide La3CuO2S3. *J. Solid State Chem.* **2003**, *172*, 257−260.

(338) Yanagi, H.; Tate, J.; Park, S.; Park, C.-H.; Keszler, D. A. P-Type Conductivity in Wide-Band-Gap BaCuQF (Q= S, Se). *Appl. Phys. Lett.* **2003**, *82*, 2814−2816.

(339) Kykyneshi, R.; McIntyre, D. H.; Tate, J.; Park, C.-H.; Keszler, D. A. Electrical and Optical Properties of Epitaxial Transparent Conductive BaCuTeF Thin Films Deposited by Pulsed Laser Deposition. *Solid State Sci.* **2008**, *10*, 921−927.

(340) Zakutayev, A.; McIntyre, D. H.; Schneider, G.; Kykyneshi, R.; Keszler, D. A.; Park, C.-H.; Tate, J. Tunable Properties of Wide-Band Gap p-Type BaCu(Ch$_{1−x}$Ch$'_x$)F (Ch = S, Se, Te) Thin-Film Solid Solutions. *Thin Solid Films* **2010**, *518*, 5494−5500.

(341) Kabbour, H.; Cario, L.; Jobic, S.; Corraze, B. P-Type Transparent Conductors Sr1−xNaxFCuS and SrF1−xOxCuS: Design, Synthesis and Physical Properties. *J. Mater. Chem.* **2006**, *16*, 4165−4169.

(342) Boudiaf, K.; Bouhemadou, A.; Al-Douri, Y.; Khenata, R.; Bin-Omran, S.; Guechi, N. Electronic and Thermoelectric Properties of the Layered BaFAgCh (Ch = S, Se and Te): First-Principles Study. *J. Alloys Compd.* **2018**, *759*, 32−43.

(343) Jaffe, J. E.; Kaspar, T. C.; Droubay, T. C.; Varga, T.; Bowden, M. E.; Exarhos, G. J. Electronic and Defect Structures of CuSCN. *J. Phys. Chem. C* **2010**, *114*, 9111−9117.

(344) Perera, V. P. S.; Senevirathna, M. K. I.; Pitigala, P.; Tennakone, K. Doping CuSCN Films for Enhancement of Conductivity: Application in Dye-Sensitized Solid-State Solar Cells. *Sol. Energy Mater. Sol. Cells* **2005**, *86*, 443−450.

(345) Pattanasattayavong, P.; Ndjawa, G. O. N.; Zhao, K.; Chou, K. W.; Yaacobi-Gross, N.; O'Regan, B. C.; Amassian, A.; Anthopoulos, T. D. Electric Field-Induced Hole Transport in Copper (I) Thiocyanate (CuSCN) Thin-Films Processed from Solution at Room Temperature. *Chem. Commun.* **2013**, *49*, 4154−4156.

(346) Sankapal, B. R.; Goncalves, E.; Ennaoui, A.; Lux-Steiner, M. C. Wide Band Gap P-Type Windows by CBD and SILAR Methods. *Thin Solid Films* **2004**, *451*, 128−132.

(347) Lévy-Clément, C.; Tena-Zaera, R.; Ryan, M. A.; Katty, A.; Hodes, G. CdSe-Sensitized P-CuSCN/Nanowire N-ZnO Heterojunctions. *Adv. Mater.* **2005**, *17*, 1512−1515.

(348) Tennakone, K.; Wijayanayake, R. H. Semiconducting Properties of Silver Thiocyanate. *J. Phys. D: Appl. Phys.* **1983**, *16*, L79.

(349) Fiorani, M.; Magno, F. A Study of Ag/Ag2S and Ag/AgSCN Electrodes: Coulometric Production of Sulphide and Thiocyanate Ions. *Anal. Chim. Acta* **1967**, *39*, 285−291.

(350) Soofivand, F.; Salavati-Niasari, M.; Mohandes, F. AgSCN Micro/Nanostructures: Facile Sonochemical Synthesis, Characterization, and Photoluminescence Properties. *J. Ind. Eng. Chem.* **2014**, *20*, 3780−3788.

(351) Setyawan, W.; Gaume, R. M.; Lam, S.; Feigelson, R. S.; Curtarolo, S. High-Throughput Combinatorial Database of Electronic Band Structures for Inorganic Scintillator Materials. *ACS Comb. Sci.* **2011**, *13*, 382−390.

(352) Hirose, H.; Ueda, K.; Kawazoe, H.; Hosono, H. Electronic Structure of Sr2Cu2ZnO2S2 Layered Oxysulfide with CuS Layers. *Chem. Mater.* **2002**, *14*, 1037−1041.

(353) Ueda, K.; Hirose, S.; Kawazoe, H.; Hosono, H. Electrical and Optical Properties of Layered Oxysulfides with CuS Layers: Sr− Cu− M− O− S System (M= Zn, Ga, In). *Chem. Mater.* **2001**, *13*, 1880−1883.

(354) Liu, M.-L.; Wu, L.-B.; Huang, F.-Q.; Chen, L.-D.; Chen, I.-W. A Promising P-Type Transparent Condcting Material: Layered Oxysulfide [Cu2S2][Sr3Sc2O5]. *J. Appl. Phys.* **2007**, *102*, 116108.

(355) Adachi, S.; Ito, K. Physical Properties: Compiled Experimental Data. In *Copper Zinc Tin Sulfide-Based Thin-Film Solar Cells*; Wiley Online Library, 2015; pp 149−179.

(356) Rosmus, K. A.; Brant, J. A.; Wisneski, S. D.; Clark, D. J.; Kim, Y. S.; Jang, J. I.; Brunetta, C. D.; Zhang, J.-H.; Srnec, M. N.; Aitken, J. A. Optical Nonlinearity in Cu2CdSnS4 and *α/β*-Cu2ZnSiS4: Diamond-

like Semiconductors with High Laser-Damage Thresholds. *Inorg. Chem.* **2014**, *53*, 7809−7811.

(357) Wu, P.; Christuk, A. E.; Ibers, J. A. New Quaternary Chalcogenides BaLnMQ3 (Ln = Rare Earth or Sc; M = Cu, Ag; Q= S, Se): II. Structure and Property Variation vs Rare-Earth Element. *J. Solid State Chem.* **1994**, *110*, 337−344.

(358) Sikerina, N. V.; Andreev, O. V. Crystal Structures of SrLnCuS3 (Ln= Gd, Lu). *Russ. J. Inorg. Chem.* **2007**, *52*, 581−584.

(359) Schevciw, O.; White, W. B. The Optical Absorption Edge of Rare Earth Sesquisulfides and Alkaline Earth - Rare Earth Sulfides. *Mater. Res. Bull.* **1983**, *18*, 1059−1068.

(360) Mitchell, K.; Haynes, C. L.; McFarland, A. D.; Van Duyne, R. P.; Ibers, J. A. Tuning of Optical Band Gaps: Syntheses, Structures, Magnetic Properties, and Optical Properties of CsLnZnSe3 (Ln= Sm, Tb, Dy, Ho, Er, Tm, Yb, and Y). *Inorg. Chem.* **2002**, *41*, 1199−1204.

(361) Butler, S. Z.; Hollen, S. M.; Cao, L.; Cui, Y.; Gupta, J. A.; Gutiérrez, H. R.; Heinz, T. F.; Hong, S. S.; Huang, J.; Ismach, A. F.; et al. Progress, Challenges, and Opportunities in Two-Dimensional Materials beyond Graphene. *ACS Nano* **2013**, *7*, 2898−2926.

(362) Wang, Q. H.; Kalantar-Zadeh, K.; Kis, A.; Coleman, J. N.; Strano, M. S. Electronics and Optoelectronics of Two-Dimensional Transition Metal Dichalcogenides. *Nat. Nanotechnol.* **2012**, *7*, 699.

(363) Choi, W.; Choudhary, N.; Han, G. H.; Park, J.; Akinwande, D.; Lee, Y. H. Recent Development of Two-Dimensional Transition Metal Dichalcogenides and Their Applications. *Mater. Today* **2017**, *20*, 116−130.

(364) Geim, A. K.; Grigorieva, I. V. Van Der Waals Heterostructures. *Nature* **2013**, *499*, 419.

(365) Osada, M.; Sasaki, T. Two-Dimensional Dielectric Nanosheets: Novel Nanoelectronics From Nanocrystal Building Blocks. *Adv. Mater.* **2012**, *24*, 210−228.

(366) Beal, A. R.; Knights, J. C.; Liang, W. Y. Transmission Spectra of Some Transition Metal Dichalcogenides. II. Group VIA: Trigonal Prismatic Coordination. *J. Phys. C: Solid State Phys.* **1972**, *5*, 3540.

(367) Robertson, J. Electronic Structure of GaSe, GaS, InSe and GaTe. *J. Phys. C: Solid State Phys.* **1979**, *12*, 4777.

(368) Du, K.; Wang, X.; Liu, Y.; Hu, P.; Utama, M. I. B.; Gan, C. K.; Xiong, Q.; Kloc, C. Weak Van Der Waals Stacking, Wide-Range Band Gap, and Raman Study on Ultrathin Layers of Metal Phosphorus Trichalcogenides. *ACS Nano* **2016**, *10*, 1738−1743.

(369) Zhao, W.; Ghorannevis, Z.; Chu, L.; Toh, M.; Kloc, C.; Tan, P.-H.; Eda, G. Evolution of Electronic Structure in Atomically Thin Sheets of WS2 and WSe2. *ACS Nano* **2013**, *7*, 791−797.

(370) Radisavljevic, B.; Kis, A. Mobility Engineering and a Metal−Insulator Transition in Monolayer MoS2. *Nat. Mater.* **2013**, *12*, 815.

(371) Kam, K. K.; Parkinson, B. A. Detailed Photocurrent Spectroscopy of the Semiconducting Group VIB Transition Metal Dichalcogenides. *J. Phys. Chem.* **1982**, *86*, 463−467.

(372) Kuc, A.; Zibouche, N.; Heine, T. Influence of Quantum Confinement on the Electronic Structure of the Transition Metal Sulfide TS2. *Phys. Rev. B: Condens. Matter Mater. Phys.* **2011**, *83*, 245213−245213a.

(373) Gutiérrez, H. R.; Perea-López, N.; Elías, A. L.; Berkdemir, A.; Wang, B.; Lv, R.; López-Urías, F.; Crespi, V. H.; Terrones, H.; Terrones, M. Extraordinary Room-Temperature Photoluminescence in Triangular WS2Monolayers. *Nano Lett.* **2013**, *13*, 3447−3454.

(374) Tonti, D.; Varsano, F.; Decker, F.; Ballif, C.; Regula, M.; Remŝkar, M. Preparation and Photoelectrochemistry of Semiconducting WS2 Thin Films. *J. Phys. Chem. B* **1997**, *101*, 2485−2490.

(375) Zhang, W.; Huang, Z.; Zhang, W.; Li, Y. Two-Dimensional Semiconductors with Possible High Room Temperature Mobility. *Nano Res.* **2014**, *7*, 1731−1737.

(376) Cui, Y.; Xin, R.; Yu, Z.; Pan, Y.; Ong, Z.-Y.; Wei, X.; Wang, J.; Nan, H.; Ni, Z.; Wu, Y.; et al. High-Performance Monolayer WS2 Field-Effect Transistors on High-*κ* Dielectrics. *Adv. Mater.* **2015**, *27*, 5230−5234.

(377) Jiang, J.; Zhang, Q.; Wang, A.; Zhang, Y.; Meng, F.; Zhang, C.; Feng, X.; Feng, Y.; Gu, L.; Liu, H.; et al. A Facile and Effective Method

for Patching Sulfur Vacancies of WS2 via Nitrogen Plasma Treatment. *Small* **2019**, *15*, 1901791.

(378) Kang, K.; Xie, S.; Huang, L.; Han, Y.; Huang, P. Y.; Mak, K. F.; Kim, C.-J.; Muller, D.; Park, J. High-Mobility Three-Atom-Thick Semiconducting Films with Wafer-Scale Homogeneity. *Nature* **2015**, *520*, 656.

(379) Li, H.; Huang, J.; Shi, Y.; Li, L. Toward the Growth of High Mobility 2D Transition Metal Dichalcogenide Semiconductors. *Adv. Mater. Interfaces* **2019**, *6*, 1900220.

(380) Tedstone, A. A.; Lewis, D. J.; O'Brien, P. Synthesis, Properties, and Applications of Transition Metal-Doped Layered Transition Metal Dichalcogenides. *Chem. Mater.* **2016**, *28*, 1965−1974.

(381) Kobayashi, Y.; Yoshida, S.; Sakurada, R.; Takashima, K.; Yamamoto, T.; Saito, T.; Konabe, S.; Taniguchi, T.; Watanabe, K.; Maniwa, Y.; et al. Modulation of Electrical Potential and Conductivity in an Atomic-Layer Semiconductor Heterojunction. *Sci. Rep.* **2016**, *6*, 31223.

(382) Huang, P.; Wang, Z.; Liu, Y.; Zhang, K.; Yuan, L.; Zhou, Y.; Song, B.; Li, Y. Water-Soluble 2D Transition Metal Dichalcogenides as the Hole-Transport Layer for Highly Efficient and Stable p−i−n Perovskite Solar Cells. *ACS Appl. Mater. Interfaces* **2017**, *9*, 25323−25331.

(383) Kim, Y. G.; Kwon, K. C.; Le, Q. V.; Hong, K.; Jang, H. W.; Kim, S. Y. Atomically Thin Two-Dimensional Materials as Hole Extraction Layers in Organolead Halide Perovskite Photovoltaic Cells. *J. Power Sources* **2016**, *319*, 1−8.

(384) Lashgari, H.; Boochani, A.; Shekaari, A.; Solaymani, S.; Sartipi, E.; Mendi, R. T. Electronic and Optical Properties of 2D Graphene-like ZnS: DFT Calculations. *Appl. Surf. Sci.* **2016**, *369*, 76−81.

(385) Sabaghi, V.; Davar, F.; Fereshteh, Z. ZnS Nanoparticles Prepared via Simple Reflux and Hydrothermal Method: Optical and Photocatalytic Properties. *Ceram. Int.* **2018**, *44*, 7545−7556.

(386) Venkatachalam, S.; Agilan, S.; Mangalaraj, D.; Narayandass, S. K. Optoelectronic Properties of ZnSe Thin Films. *Mater. Sci. Semicond. Process.* **2007**, *10*, 128−132.

(387) Bacaksiz, C.; Senger, R. T.; Sahin, H. Ultra-Thin ZnSe: Anisotropic and Flexible Crystal Structure. *Appl. Surf. Sci.* **2017**, *409*, 426−430.

(388) Sun, Y.; Sun, Z.; Gao, S.; Cheng, H.; Liu, Q.; Piao, J.; Yao, T.; Wu, C.; Hu, S.; Wei, S.; et al. Fabrication of Flexible and Freestanding Zinc Chalcogenide Single Layers. *Nat. Commun.* **2012**, *3*, 1057.

(389) Li, L.; Li, P.; Lu, N.; Dai, J.; Zeng, X. C. Simulation Evidence of Hexagonal-to-Tetragonal ZnSe Structure Transition: A Monolayer Material with a Wide-Range Tunable Direct Bandgap. *Adv. Sci.* **2015**, *2*, 1500290.

(390) Gao, T.; Wang, T. Two-Dimensional Single Crystal CdS Nanosheets: Synthesis and Properties. *Cryst. Growth Des.* **2010**, *10*, 4995−5000.

(391) Son, J. S.; Park, K.; Kwon, S. G.; Yang, J.; Choi, M. K.; Kim, J.; Yu, J. H.; Joo, J.; Hyeon, T. Dimension-Controlled Synthesis of CdS Nanocrystals: From 0D Quantum Dots to 2D Nanoplates. *Small* **2012**, *8*, 2394−2402.

(392) Maiti, P. S.; Bar Sadan, M. Tuning the Surface Properties of Alloyed CdSxSe 1−x 2D Nanosheets. *RSC Adv.* **2015**, *5*, 100834−100837.

(393) Han, C.; Chen, Z.; Zhang, N.; Colmenares, J. C.; Xu, Y.-J. Hierarchically CdS Decorated 1D ZnO Nanorods-2D Graphene Hybrids: Low Temperature Synthesis and Enhanced Photocatalytic Performance. *Adv. Funct. Mater.* **2015**, *25*, 221−229.

(394) Bera, R.; Kundu, S.; Patra, A. 2D Hybrid Nanostructure of Reduced Graphene Oxide−CdS Nanosheet for Enhanced Photocatalysis. *ACS Appl. Mater. Interfaces* **2015**, *7*, 13251−13259.

(395) Zhang, N.; Zhang, Y.; Pan, X.; Fu, X.; Liu, S.; Xu, Y.-J. Assembly of CdS Nanoparticles on the Two-Dimensional Graphene Scaffold as Visible-Light-Driven Photocatalyst for Selective Organic Transformation under Ambient Conditions. *J. Phys. Chem. C* **2011**, *115*, 23501−23511.

(396) Ma, F.; Wu, Y.; Shao, Y.; Zhong, Y.; Lv, J.; Hao, X. 0D/2D Nanocomposite Visible Light Photocatalyst for Highly Stable and

Efficient Hydrogen Generation via Recrystallization of CdS on MoS2 Nanosheets. *Nano Energy* **2016**, *27*, 466−474.

(397) Ma, S.; Xie, J.; Wen, J.; He, K.; Li, X.; Liu, W.; Zhang, X. Constructing 2D Layered Hybrid CdS Nanosheets/MoS2 Heterojunctions for Enhanced Visible-Light Photocatalytic H2 Generation. *Appl. Surf. Sci.* **2017**, *391*, 580−591.

(398) Yang, H.; Li, J.; Yu, L.; Huang, B.; Ma, Y.; Dai, Y. A Theoretical Study on the Electronic Properties of In-Plane CdS/ZnSe Heterostructures: Type-II Band Alignment for Water Splitting. *J. Mater. Chem. A* **2018**, *6*, 4161−4166.

(399) Guo, Y.; Robertson, J. Band Structure, Band Offsets, Substitutional Doping, and Schottky Barriers of Bulk and Monolayer InSe. *Phys. Rev. Mater.* **2017**, *1*, 044004.

(400) Sun, C.; Xiang, H.; Xu, B.; Xia, Y.; Yin, J.; Liu, Z. Ab Initio Study of Carrier Mobility of Few-Layer InSe. *Appl. Phys. Express* **2016**, *9*, 035203.

(401) Bandurin, D. A.; Tyurnina, A. V.; Yu, G. L.; Mishchenko, A.; Zólyomi, V.; Morozov, S. V.; Kumar, R. K.; Gorbachev, R. V.; Kudrynskyi, Z. R.; Pezzini, S.; et al. High Electron Mobility, Quantum Hall Effect and Anomalous Optical Response in Atomically Thin InSe. *Nat. Nanotechnol.* **2017**, *12*, 223−227.

(402) Lei, S.; Ge, L.; Najmaei, S.; George, A.; Kappera, R.; Lou, J.; Chhowalla, M.; Yamaguchi, H.; Gupta, G.; Vajtai, R.; et al. Evolution of the Electronic Band Structure and Efficient Photo-Detection in Atomic Layers of InSe. *ACS Nano* **2014**, *8*, 1263−1272.

(403) Tamalampudi, S. R.; Lu, Y.-Y.; Kumar U, R.; Sankar, R.; Liao, C.-D.; Moorthy B, K.; Cheng, C.-H.; Chou, F. C.; Chen, Y.-T. High Performance and Bendable Few-Layered InSe Photodetectors with Broad Spectral Response. *Nano Lett.* **2014**, *14*, 2800−2806.

(404) Hu, P.; Wang, L.; Yoon, M.; Zhang, J.; Feng, W.; Wang, X.; Wen, Z.; Idrobo, J. C.; Miyamoto, Y.; Geohegan, D. B.; et al. Highly Responsive Ultrathin GaS Nanosheet Photodetectors on Rigid and Flexible Substrates. *Nano Lett.* **2013**, *13*, 1649−1654.

(405) Ma, Y.; Dai, Y.; Guo, M.; Yu, L.; Huang, B. Tunable Electronic and Dielectric Behavior of GaS and GaSe Monolayers. *Phys. Chem. Chem. Phys.* **2013**, *15*, 7098−7105.

(406) Minder, R.; Ottaviani, G.; Canali, C. Charge Transport in Layer Semiconductors. *J. Phys. Chem. Solids* **1976**, *37*, 417−424.

(407) Carey, B. J.; Ou, J. Z.; Clark, R. M.; Berean, K. J.; Zavabeti, A.; Chesman, A. S. R.; Russo, S. P.; Lau, D. W. M.; Xu, Z.-Q.; Bao, Q.; et al. Wafer-Scale Two-Dimensional Semiconductors from Printed Oxide Skin of Liquid Metals. *Nat. Commun.* **2017**, *8*, 14482.

(408) Late, D. J.; Liu, B.; Luo, J.; Yan, A.; Matte, H. S. S. R.; Grayson, M.; Rao, C. N. R.; Dravid, V. P. GaS and GaSe Ultrathin Layer Transistors. *Adv. Mater.* **2012**, *24*, 3549−3554.

(409) Li, F.; Liu, X.; Wang, Y.; Li, Y. Germanium Monosulfide Monolayer: A Novel Two-Dimensional Semiconductor with a High Carrier Mobility. *J. Mater. Chem. C* **2016**, *4*, 2155−2159.

(410) Ji, Y.; Yang, M.; Dong, H.; Hou, T.; Wang, L.; Li, Y. Two-Dimensional Germanium Monochalcogenide Photocatalyst for Water Splitting under Ultraviolet, Visible to near-Infrared Light. *Nanoscale* **2017**, *9*, 8608−8615.

(411) Zhang, S.; Wang, N.; Liu, S.; Huang, S.; Zhou, W.; Cai, B.; Xie, M.; Yang, Q.; Zeng, H.; et al. Two-Dimensional GeS with Tunable Electronic Properties via External Electric Field and Strain. *Nanotechnology* **2016**, *27*, 274001.

(412) Ma, S.; Yuan, D.; Wang, Y.; Jiao, Z. Monolayer GeS as a Potential Candidate for NO2 Gas Sensors and Capturers. *J. Mater. Chem. C* **2018**, *6*, 8082−8091.

(413) Karmakar, S.; Chowdhury, C.; Datta, A. Noble-Metal-Supported GeS Monolayer as Promising Single-Atom Catalyst for CO Oxidation. *J. Phys. Chem. C* **2018**, *122*, 14488−14498.

(414) Gu, D.; Tao, X.; Chen, H.; Zhu, W.; Ouyang, Y.; Peng, Q. Enhanced Photocatalytic Activity for Water Splitting of Blue-Phase GeS and GeSe Monolayers via Biaxial Straining. *Nanoscale* **2019**, *11*, 2335−2342.

(415) Williams, R. H.; Murray, R. B.; Govan, D. W.; Thomas, J. M.; Evans, E. L. Band Structure and Photoemission Studies of SnS2 and SnSe2. I. Experimental. *J. Phys. C: Solid State Phys.* **1973**, *6*, 3631.

(416) Price, L. S.; Parkin, I. P.; Hardy, A. M. E.; Clark, R. J. H.; Hibbert, T. G.; Molloy, K. C. Atmospheric Pressure Chemical Vapor Deposition of Tin Sulfides (SnS, Sn2S3, and SnS2) on Glass. *Chem. Mater.* **1999**, *11*, 1792−1799.

(417) Gonzalez, J. M.; Oleynik, I. I. Layer-Dependent Properties of SnS2 and SnSe2 Two-Dimensional Materials. *Phys. Rev. B: Condens. Matter Mater. Phys.* **2016**, *94*, 125443.

(418) Song, H. S.; Li, S. L.; Gao, L.; Xu, Y.; Ueno, K.; Tang, J.; Cheng, Y. B.; Tsukagoshi, K. High-Performance Top-Gated Monolayer SnS2 Field-Effect Transistors and Their Integrated Logic Circuits. *Nanoscale* **2013**, *5*, 9666−9670.

(419) Huang, Y.; Sutter, E.; Sadowski, J. T.; Cotlet, M.; Monti, O. L. A.; Racke, D. A.; Neupane, M. R.; Wickramaratne, D.; Lake, R. K.; Parkinson, B. A.; et al. Tin Disulfide—An Emerging Layered Metal Dichalcogenide Semiconductor: Materials Properties and Device Characteristics. *ACS Nano* **2014**, *8*, 10743−10755.

(420) Asikainen, T.; Ritala, M.; Leskelä, M. Growth of In2S3 Thin Films by Atomic Layer Epitaxy. *Appl. Surf. Sci.* **1994**, *82−83*, 122−125.

(421) Acharya, S.; Sarkar, S.; Pradhan, N. Subnanometer Thin β-Indium Sulfide Nanosheets. *J. Phys. Chem. Lett.* **2012**, *3*, 3812−3817.

(422) Tian, Y.; Wang, L.; Tang, H.; Zhou, W. Ultrathin Two-Dimensional β-In2S3 Nanocrystals: Oriented-Attachment Growth Controlled by Metal Ions and Photoelectrochemical Properties. *J. Mater. Chem. A* **2015**, *3*, 11294−11301.

(423) Huang, W.; Gan, L.; Yang, H.; Zhou, N.; Wang, R.; Wu, W.; Li, H.; Ma, Y.; Zeng, H.; Zhai, T. Controlled Synthesis of Ultrathin 2D β-In2S3 with Broadband Photoresponse by Chemical Vapor Deposition. *Adv. Funct. Mater.* **2017**, *27*, 1702448.

(424) Mamedov, S.; Drichko, N. Characterization of 2D As2S3 Crystal by Raman Spectroscopy. *MRS Adv.* **2018**, *3*, 385−390.

(425) Katayama, S.; Kashida, S.; Hori, T. Structural Instability and Photoconduction of Tl1+(Tl3+S22-). *Jpn. J. Appl. Phys.* **1993**, *32*, 639.

(426) Panich, A. M. Electronic Properties and Phase Transitions in Low-Dimensional Semiconductors. *J. Phys.: Condens. Matter* **2008**, *20*, 293202.

(427) Hanias, M. P.; Anagnostopoulos, A. N.; Kambas, K.; Spyridelis, J. Electrical and Optical Properties of As-Grown TlInS2, TlGaSe2 and TlGaS2 Single Crystals. *Mater. Res. Bull.* **1992**, *27*, 25−38.

(428) Yang, S.; Wu, M.; Wang, H.; Cai, H.; Huang, L.; Jiang, C.; Tongay, S. Ultrathin Ternary Semiconductor TlGaSe 2 Photo-transistors with Broad-Spectral Response. *2D Mater.* **2017**, *4*, 035021.

(429) Wei, J.; Wang, C.; Zhang, T.; Dai, C.-M.; Chen, S. High-Throughput Screening and Classification of Layered Di-Metal Chalcogenides. *Nanoscale* **2019**, *11*, 13924−13933.

(430) Liu, J.; Li, X.-B.; Wang, D.; Lau, W.-M.; Peng, P.; Liu, L.-M. Diverse and Tunable Electronic Structures of Single-Layer Metal Phosphorus Trichalcogenides for Photocatalytic Water Splitting. *J. Chem. Phys.* **2014**, *140*, 054707.

(431) Li, X.; Wu, X.; Yang, J. Half-Metallicity in MnPSe3 Exfoliated Nanosheet with Carrier Doping. *J. Am. Chem. Soc.* **2014**, *136*, 11065−11069.

(432) Zhang, X.; Zhao, X.; Wu, D.; Jing, Y.; Zhou, Z. MnPSe3Monolayer: A Promising 2D Visible-Light Photohydrolytic Catalyst with High Carrier Mobility. *Adv. Sci.* **2016**, *3*, 1600062.

(433) Sang, L.; Liao, M.; Sumiya, M. A Comprehensive Review of Semiconductor Ultraviolet Photodetectors: From Thin Film to One-Dimensional Nanostructures. *Sensors* **2013**, *13*, 10482−10518.

(434) Haase, M. A.; Qiu, J.; DePuydt, J. M.; Cheng, H. Blue-Green Laser Diodes. *Appl. Phys. Lett.* **1991**, *59*, 1272−1274.

(435) Cheng, P. C.; Pan, S. J.; Shih, A.; Kim, K. S.; Liou, W. S.; Park, M. S. Highly Efficient Upconverters for Multiphoton Fluorescence Microscopy. *J. Microsc.* **1998**, *189*, 199−212.

(436) Weber, M. J. Inorganic Scintillators: Today and Tomorrow. *J. Lumin.* **2002**, *100*, 35−45.

(437) Gas'kov, A. M.; Rumyantseva, M. N. Materials for Solid-State Gas Sensors. *Inorg. Mater.* **2000**, *36*, 293−301.

(438) Sootsman, J. R.; Chung, D. Y.; Kanatzidis, M. G. New and Old Concepts in Thermoelectric Materials. *Angew. Chem., Int. Ed.* **2009**, *48*, 8616−8639.

(439) Chung, D. Y.; Lordanidis, L.; Choi, K. S.; Kanatzidis, M. G. Complex Chalcogenides as Thermoelectric Materials: A Solid State Chemistry Approach. *Bull. Korean Chem. Soc.* **1998**, *19*, 1283−1293.

(440) Rauh, R. D. Electrochromic Windows: An Overview. *Electrochim. Acta* **1999**, *44*, 3165−3176.

(441) Runnerstrom, E. L.; Llordés, A.; Lounis, S. D.; Milliron, D. J. Nanostructured Electrochromic Smart Windows: Traditional Materials and NIR-Selective Plasmonic Nanocrystals. *Chem. Commun.* **2014**, *50*, 10555−10572.

(442) Rashid, M. H. *Power Electronics Handbook*; 2007.

(443) Dye, N.; Granberg, H. *Radio Frequency Transistors: Principles and Practical Applications*, 2nd ed.; Elsevier: Wobern, MA, 2001.

(444) Perrenoud, J. C. *Low Temperature Grown CdTe Thin Film Solar Cells for the Application on Flexible Substrates*; ETH Zurich, 2012.

(445) Azimi, H.; Hou, Y.; Brabec, C. J. Towards Low-Cost, Environmentally Friendly Printed Chalcopyrite and Kesterite Solar Cells. *Energy Environ. Sci.* **2014**, *7*, 1829−1849.

(446) P.S, S. *Introduction to Organic Electronic Materials*; 2014.

(447) Shafarman, W. N.; Siebentritt, S.; Stolt, L. Cu (InGa) Se2 Solar Cells. *Handb. Photovolt. Sci. Eng.* **2011**, *2*, 546−599.

(448) Green, M. A.; Dunlop, E. D.; Levi, D. H.; Hohl-Ebinger, J.; Yoshita, M.; Ho-Baillie, A. W. Y. Solar Cell Efficiency Tables (Version 54). *Prog. Photovoltaics* **2019**, *27*, 565.

(449) Triboulet, R.; Siffert, P. *CdTe and Related Compounds; Physics, Defects, Hetero-and Nano-Structures, Crystal Growth, Surfaces and Applications: Physics, CdTe-Based Nanostructures, CdTe-Based Semimagnetic Semiconductors, Defects*; Elsevier, 2009.

(450) Coutts, T. J.; Wu, X.; Mulligan, W. P.; Webb, J. M. High-Performance, Transparent Conducting Oxides Based on Cadmium Stannate. *J. Electron. Mater.* **1996**, *25*, 935−943.

(451) Wu, X.; Mulligan, W. P.; Coutts, T. J. Recent Developments in RF Sputtered Cadmium Stannate Films. *Thin Solid Films* **1996**, *286*, 274−276.

(452) Chu, T. L.; Chu, S. S.; Ferekides, C.; Wu, C. Q.; Britt, J.; Wang, C. 13.4% Efficient Thin-film CdS/CdTe Solar Cells. *J. Appl. Phys.* **1991**, *70*, 7608−7612.

(453) Britt, J.; Ferekides, C. Thin-Film CdS/CdTe Solar Cell with 15.8% Efficiency. *Appl. Phys. Lett.* **1993**, *62*, 2851−2852.

(454) Durose, K.; Edwards, P. R.; Halliday, D. P. Materials Aspects of CdTe/CdS Solar Cells. *J. Cryst. Growth* **1999**, *197*, 733−742.

(455) Wu, X. High-Efficiency Polycrystalline CdTe Thin-Film Solar Cells. *Sol. Energy* **2004**, *77*, 803−814.

(456) Yun, J. H.; Kim, K. H.; Lee, D. Y.; Ahn, B. T. Back Contact Formation Using Cu2Te as a Cu-Doping Source and as an Electrode in CdTe Solar Cells. *Sol. Energy Mater. Sol. Cells* **2003**, *75*, 203−210.

(457) Song, T.; Moore, A.; Sites, J. R. Te Layer to Reduce the CDTE Back-Contact Barrier. *IEEE J. Photovoltaics* **2018**, *8*, 293−298.

(458) Song, T.; Kanevce, A.; Sites, J. R. Emitter/Absorber Interface of CdTe Solar Cells. *J. Appl. Phys.* **2016**, *119*, 233104.

(459) Ablekim, T.; Perkins, C.; Zheng, X.; Reich, C.; Swanson, D.; Colegrove, E.; Duenow, J. N.; Albin, D.; Nanayakkara, S.; Reese, M. O.; et al. Tailoring MgZnO/CdSeTe Interfaces for Photovoltaics. *IEEE J. Photovoltaics* **2019**, *9*, 888−892.

(460) Fritsche, J.; Klein, A.; Jaegermann, W. Thin Film Solar Cells: Materials Science at Interfaces. *Adv. Eng. Mater.* **2005**, *7*, 914−920.

(461) Wei, S.-H.; Zhang, S. B.; Zunger, A. First-Principles Calculation of Band Offsets, Optical Bowings, and Defects in CdS, CdSe, CdTe, and Their Alloys. *J. Appl. Phys.* **2000**, *87*, 1304−1311.

(462) Santos-Cruz, J.; Torres-Delgado, G.; Castanedo-Pérez, R.; Jiménez-Sandoval, S.; Márquez-Marín, J.; Zelaya-Angel, O. Au−Cu/p−CdTe/n−CdO/Glass-Type Solar Cells. *Sol. Energy Mater. Sol. Cells* **2006**, *90*, 2272−2279.

(463) Uda, H.; Ikegami, S.; Sonomura, H. Annealing Effect of Cu2Te/ Au Contact to Evaporated CdTe Film on Photovoltaic Properties of CdS/CdTe Solar Cell. *Sol. Energy Mater. Sol. Cells* **1998**, *50*, 141−146.

(464) Gessert, T. A.; Mason, A. R.; Sheldon, P.; Swartzlander, A. B.; Niles, D.; Coutts, T. J. Development of Cu-doped ZnTe as a Back-contact Interface Layer for Thin-film CdS/CdTe Solar Cells. *J. Vac. Sci. Technol., A* **1996**, *14*, 806−812.

(465) Guo, D.; Brinkman, D.; Shaik, A. R.; Ringhofer, C.; Vasileska, D. Metastability and Reliability of CdTe Solar Cells. *J. Phys. D: Appl. Phys.* **2018**, *51*, 153002.

(466) Hsiao, K.; Sites, J. R. Electron Reflector to Enhance Photovoltaic Efficiency: Application to Thin-film CdTe Solar Cells. *Prog. Photovoltaics* **2012**, *20*, 486−489.

(467) Continenza, A.; Massidda, S. Electronic Properties and Valence-Band Offset of Strained ZnTe/CdTe (001) Superlattices. *Phys. Rev. B: Condens. Matter Mater. Phys.* **1994**, *50*, 11949.

(468) Niles, D. W.; Höchst, H.; Rioux, D. Valence Band Discontinuity at the ZnTe/CdTe Interface: Making Ohmic Contact to P-type CdTe. In *AIP Conference Proceedings*; AIP, 1992; Vol. *268*, pp 279−284.

(469) John, V. S.; Mahalingam, T.; Chu, J. P. Synthesis and Characterization of Copper Doped Zinc Telluride Thin Films. *Solid-State Electron.* **2005**, *49*, 3−7.

(470) Baron, T.; Saminadayar, K.; Magnea, N. Nitrogen Doping of Te-Based II−VI Compounds during Growth by Molecular Beam Epitaxy. *J. Appl. Phys.* **1998**, *83*, 1354.

(471) Strevel, N.; Trippel, L.; Kotarba, C.; Khan, I. Improvements in CdTe Module Reliability and Long-Term Degradation through Advances in Construction and Device Innovation. *Photovoltaics International* **2014**, *22*, 1−8.

(472) Zhao, Y.; Boccard, M.; Liu, S.; Becker, J.; Zhao, X. H.; Campbell, C. M.; Suarez, E.; Lassise, M. B.; Holman, Z.; Zhang, Y. H. Monocrystalline CdTe Solar Cells with Open-Circuit Voltage over 1 v and Efficiency of 17%. *Nat. Energy* **2016**, *1*, 16067.

(473) Boyle, J. H.; McCandless, B. E.; Shafarman, W. N.; Birkmire, R. W. Structural and Optical Properties of (Ag,Cu)(In,Ga)Se2 Polycrystalline Thin Film Alloys. *J. Appl. Phys.* **2014**, *115*, 223504.

(474) Mohan, R.; Paulose, R. Brief Review on Copper Indium Gallium Diselenide (CIGS) Solar Cells. *Photoenergy Thin Film Mater.* **2019**, 157−192.

(475) Ong, K. H.; Ramasamy, A.; Arnou, P.; Maniscalco, B.; Bowers, J. W.; Bte Marsadek, M.; et al. Formation of MoOx Barrier Layer under Atmospheric Based Condition to Control MoSe2 Formation in CIGS Thin Film Solar Cell. *Mater. Technol.* **2018**, *33*, 723−729.

(476) Wei, S.-H.; Zhang, S. B.; Zunger, A. Effects of Ga Addition to CuInSe2 on Its Electronic, Structural, and Defect Properties. *Appl. Phys. Lett.* **1998**, *72*, 3199−3201.

(477) Schulmeyer, T.; Hunger, R.; Klein, A.; Jaegermann, W.; Niki, S. Photoemission Study and Band Alignment of the CuInSe2(001)/CdS Heterojunction. *Appl. Phys. Lett.* **2004**, *84*, 3067−3069.

(478) Zhang, S. B.; Wei, S.-H.; Zunger, A. A Phenomenological Model for Systematization and Prediction of Doping Limits in II−VI and I−III−VI2 Compounds. *J. Appl. Phys.* **1998**, *83*, 3192−3196.

(479) Schulmeyer, T.; Kniese, R.; Hunger, R.; Jaegermann, W.; Powalla, M.; Klein, A. Influence of Cu(In,Ga)Se 2 Band Gap on the Valence Band Offset with CdS. *Thin Solid Films* **2004**, *451*, 420−423.

(480) Mezher, M.; Garris, R.; Mansfield, L. M.; Horsley, K.; Weinhardt, L.; Duncan, D. A.; Blum, M.; Rosenberg, S. G.; Bär, M.; Ramanathan, K.; et al. Electronic Structure of the Zn(O,S)/Cu(In,Ga)Se2 Thin-Film Solar Cell Interface. *Prog. Photovoltaics* **2016**, *24*, 1142−1148.

(481) Naghavi, N.; Spiering, S.; Powalla, M.; Cavana, B.; Lincot, D. High-Efficiency Copper Indium Gallium Diselenide (CIGS) Solar Cells with Indium Sulfide Buffer Layers Deposited by Atomic Layer Chemical Vapor Deposition (ALCVD). *Prog. Photovoltaics* **2003**, *11*, 437−443.

(482) Bernède, J. C.; Barreau, N.; Marsillac, S.; Assmann, L. Band Alignment at β-In2S3/TCO Interface. *Appl. Surf. Sci.* **2002**, *195*, 222−228.

(483) Abou-Ras, D.; Kostorz, G.; Strohm, A.; Schock, H.-W.; Tiwari, A. N. Interfacial Layer Formations between Cu(In,Ga)Se2 and InxSy Layers. *J. Appl. Phys.* **2005**, *98*, 123512.

(484) Gall, S.; Barreau, N.; Harel, S.; Bernede, J. C.; Kessler, J. Material Analysis of PVD-Grown Indium Sulphide Buffer Layers for Cu(In,Ga)Se 2-Based Solar Cells. *Thin Solid Films* **2005**, *480*, 138−141.

(485) Bär, M.; Allsop, N.; Lauermann, I.; Fischer, C.-H. Deposition of In2S3 on Cu(In,Ga)(S,Se)2 Thin Film Solar Cell Absorbers by Spray Ion Layer Gas Reaction: Evidence of Strong Interfacial Diffusion. *Appl. Phys. Lett.* **2007**, *90*, 132118.

(486) Kamada, R.; Yagioka, T.; Adachi, S.; Handa, A.; Tai, K. F.; Kato, T.; Sugimoto, H. New World Record Cu(In, Ga)(Se, S)2thin film Solar Cell Efficiency beyond 22%. In *2016 IEEE 43rd Photovoltaic Specialists Conference (PVSC)*; 2016; pp 1287−1291.

(487) Goto, H.; Hashimoto, Y.; Ito, K. Efficient Thin Film Solar Cell Consisting of TCO/CdS/CuInS2/CuGaS2 Structure. *Thin Solid Films* **2004**, *451*, 552−555.

(488) Rondiya, S.; Rokade, A.; Sharma, P.; Chaudhary, M.; Funde, A.; Jadhav, Y.; Haram, S.; Pathan, H.; Jadkar, S. CZTS/CdS: Interface Properties and Band Alignment Study towards Photovoltaic Applications. *J. Mater. Sci.: Mater. Electron.* **2018**, *29*, 4201−4210.

(489) Boutebakh, F. Z.; Zeggar, M. L.; Attaf, N.; Aida, M. S. Electrical Properties and Back Contact Study of CZTS/ZnS Heterojunction. *Optik (Munich, Ger.)* **2017**, *144*, 180−190.

(490) Guitouni, S.; Khammar, M.; Messaoudi, M.; Attaf, N.; Aida, M. S. Electrical Properties of Cu 4 ZnSnS 2/ZnS Heterojunction Prepared by Ultrasonic Spray Pyrolysis. *J. Semicond.* **2016**, *37*, 122001.

(491) Katagiri, H.; Jimbo, K.; Maw, W. S.; Oishi, K.; Yamazaki, M.; Araki, H.; Takeuchi, A. Development of CZTS-Based Thin Film Solar Cells. *Thin Solid Films* **2009**, *517*, 2455−2460.

(492) DeWolf, S.; Descoeudres, A.; Holman, Z. C.; Ballif, C. High-Efficiency Silicon Heterojunction Solar Cells: A Review. *Green* **2012**, *2*, 7−24.

(493) Bullock, J.; Hettick, M.; Geissbühler, J.; Ong, A. J.; Allen, T.; Sutter-Fella, C. M.; Chen, T.; Ota, H.; Schaler, E. W.; De Wolf, S.; et al. Efficient Silicon Solar Cells with Dopant-Free Asymmetric Heterocontacts. *Nat. Energy* **2016**, *1*, 15031.

(494) Battaglia, C.; Cuevas, A.; De Wolf, S. High-Efficiency Crystalline Silicon Solar Cells: Status and Perspectives. *Energy Environ. Sci.* **2016**, *9*, 1552−1576.

(495) Xu, X.; Bullock, J.; Schelhas, L. T.; Stutz, E. Z.; Fonseca, J. J.; Hettick, M.; Pool, V. L.; Tai, K. F.; Toney, M. F.; Fang, X.; et al. Chemical Bath Deposition of P-Type Transparent, Highly Conducting (CuS)x:(ZnS)1-x Nanocomposite Thin Films and Fabrication of Si Heterojunction Solar Cells. *Nano Lett.* **2016**, *16*, 1925−1932.

(496) Juarez-Perez, E. J.; Wußler, M.; Fabregat-Santiago, F.; Lakus-Wollny, K.; Mankel, E.; Mayer, T.; Jaegermann, W.; Mora-Sero, I. Role of the Selective Contacts in the Performance of Lead Halide Perovskite Solar Cells. *J. Phys. Chem. Lett.* **2014**, *5*, 680−685.

(497) Arora, N.; Dar, M. I.; Hinderhofer, A.; Pellet, N.; Schreiber, F.; Zakeeruddin, S. M.; Grätzel, M. Perovskite Solar Cells with CuSCN Hole Extraction Layers Yield Stabilized Efficiencies Greater than 20%. *Science (Washington, DC, U. S.)* **2017**, *358*, 768−771.

(498) Qin, P.; Tanaka, S.; Ito, S.; Tetreault, N.; Manabe, K.; Nishino, H.; Nazeeruddin, M. K.; Grätzel, M. Inorganic Hole Conductor-Based Lead Halide Perovskite Solar Cells with 12.4% Conversion Efficiency. *Nat. Commun.* **2014**, *5*, 3834.

(499) Wu, Q.; Xue, C.; Li, Y.; Zhou, P.; Liu, W.; Zhu, J.; Dai, S.; Zhu, C.; Yang, S. Kesterite Cu2ZnSnS4 as a Low-Cost Inorganic Hole-Transporting Material for High-Efficiency Perovskite Solar Cells. *ACS Appl. Mater. Interfaces* **2015**, *7*, 28466−28473.

(500) Jung, M.; Kim, Y. C.; Jeon, N. J.; Yang, W. S.; Seo, J.; Noh, J. H.; Il Seok, S. Thermal Stability of CuSCN Hole Conductor-Based Perovskite Solar Cells. *ChemSusChem* **2016**, *9*, 2592−2596.

(501) Park, N. G. Perovskite Solar Cells: An Emerging Photovoltaic Technology. *Mater. Today* **2015**, *18*, 65−72.

(502) Philipps, S. P.; Dimroth, F.; Bett, A. W. High-Efficiency III−V Multijunction Solar Cells. In *McEvoy's Handbook of Photovoltaics: Fundamentals and Applications*; 2017.

(503) Okada, Y.; Ekins-Daukes, N. J.; Kita, T.; Tamaki, R.; Yoshida, M.; Pusch, A.; Hess, O.; Phillips, C. C.; Farrell, D. J.; Yoshida, K.; et al. Intermediate Band Solar Cells: Recent Progress and Future Directions. *Appl. Phys. Rev.* **2015**, *2*, 021302.

(504) Huang, D.; Jiang, J.-W.; Guo, J.; Zhao, Y.-J.; Chen, R.; Persson, C. Group-IV (Si, Ge, and Sn)-Doped AgAlTe 2 for Intermediate Band

Solar Cell from First- Principles Study. *Semicond. Sci. Technol.* **2017**, *32*, 065007.

(505) Mitzi, D. B.; Kosbar, L. L.; Murray, C. E.; Copel, M.; Afzali, A. High-Mobility Ultrathin Semiconducting Films Prepared by Spin Coating. *Nature* **2004**, *428*, 299−303.

(506) Shin, K. Y.; Tak, Y. J.; Kim, W.-G.; Hong, S.; Kim, H. J. Improvement of Electrical Characteristics and Stability of Amorphous Indium Gallium Zinc Oxide Thin Film Transistors Using Nitrocellulose Passivation Layer. *ACS Appl. Mater. Interfaces* **2017**, *9*, 13278−13285.

(507) Spinulescu-Carnaru, I. ZnTe and InSb Thin-Film Transistors. *Electron. Lett.* **1967**, *3*, 268−269.

(508) Bowen, W. E.; Wang, W.; Phillips, J. D. Complementary Thin-Film Electronics Based on n-Channel ZnO and p-Channel ZnTe. *IEEE Electron Device Lett.* **2009**, *30*, 1314−1316.

(509) Voss, C.; Subramanian, S.; Chang, C.-H. Cadmium Sulfide Thin-Film Transistors Fabricated by Low-Temperature Chemical-Bath Deposition. *J. Appl. Phys.* **2004**, *96*, 5819−5823.

(510) Salas-Villasenor, A. L.; Mejia, I.; Hovarth, J.; Alshareef, H. N.; Cha, D. K.; Ramirez-Bon, R.; Gnade, B. E.; Quevedo-Lopez, M. A. Impact of Gate Dielectric in Carrier Mobility in Low Temperature Chalcogenide Thin Film Transistors for Flexible Electronics. *Electrochem. Solid-State Lett.* **2010**, *13*, H313−H316.

(511) Shallcross, F. V. Cadmium Selenide Thin-Film Transistors. *Proc. IEEE* **1963**, *51*, 851.

(512) Morales-Fernández, I. E.; Medina-Montes, M. I.; González, L. A.; Gnade, B.; Quevedo-López, M. A.; Ramírez-Bon, R. Electrical Behavior of P-Type PbS-Based Metal-Oxide-Semiconductor Thin Film Transistors. *Thin Solid Films* **2010**, *519*, 512−516.

(513) Carrillo-Castillo, A.; Salas-Villasenor, A.; Mejia, I.; Aguirre-Tostado, S.; Gnade, B. E.; Quevedo-López, M. A. P-Type Thin Films Transistors with Solution-Deposited Lead Sulfide Films as Semiconductor. *Thin Solid Films* **2012**, *520*, 3107−3110.

(514) Mitzi, D. B.; Copel, M.; Murray, C. E. High-Mobility P-Type Transistor Based on a Spin-Coated Metal Telluride Semiconductor. *Adv. Mater.* **2006**, *18*, 2448−2452.

(515) Yabuta, H.; Sano, M.; Abe, K.; Aiba, T.; Den, T.; Kumomi, H.; Nomura, K.; Kamiya, T.; Hosono, H. High-Mobility Thin-Film Transistor with Amorphous In Ga Zn O 4 Channel Fabricated by Room Temperature Rf-Magnetron Sputtering. *Appl. Phys. Lett.* **2006**, *89*, 112123.

(516) Myeonghun, U.; Han, Y. J.; Song, S. H.; Cho, I. T.; Lee, J. H.; Kwon, H. I. High Performance P-Type SnO Thin-Film Transistor with SiOx Gate Insulator Deposited by Low-Temperature PECVD Method. *J. Semicond. Technol. Sci.* **2014**, *14*, 666−672.

(517) Bolton, J. R.; Strickler, S. J.; Connolly, J. S. Limiting and Realizable Efficiencies of Solar Photolysis of Water. *Nature* **1985**, *316*, 495.

(518) Tsuji, I.; Kato, H.; Kudo, A. Photocatalytic Hydrogen Evolution on ZnS−CuInS2−AgInS2 Solid Solution Photocatalysts with Wide Visible Light Absorption Bands. *Chem. Mater.* **2006**, *18*, 1969−1975.

(519) Zhao, M.; Huang, F.; Lin, H.; Zhou, J.; Xu, J.; Wu, Q.; Wang, Y. CuGaS2−ZnS p−n Nanoheterostructures: A Promising Visible Light Photo-Catalyst for Water-Splitting Hydrogen Production. *Nanoscale* **2016**, *8*, 16670−16676.

(520) Wei, L.; Chen, Y.; Lin, Y.; Wu, H.; Yuan, R.; Li, Z. MoS2 as Non-Noble-Metal Co-Catalyst for Photocatalytic Hydrogen Evolution over Hexagonal ZnIn2S4 under Visible Light Irradiations. *Appl. Catal., B* **2014**, *144*, 521−527.

(521) Kudo, A.; Nagane, A.; Tsuji, I.; Kato, H. H2 Evolution from Aqueous Potassium Sulfite Solutions under Visible Light Irradiation over a Novel Sulfide Photocatalyst NaInS2 with a Layered Structure. *Chem. Lett.* **2002**, *31*, 882−883.

(522) Sun, J.; Chen, G.; Xiong, G.; Pei, J.; Dong, H. Hierarchical Microarchitectures of AgGa1− XInxS2: Long Chain Alcohol Assisted Synthesis, Band Gap Tailoring and Photocatalytic Activities of Hydrogen Generation. *Int. J. Hydrogen Energy* **2013**, *38*, 10731−10738.

(523) Yu, X.; An, X.; Shavel, A.; Ibanez, M.; Cabot, A. The Effect of the Ga Content on the Photocatalytic Hydrogen Evolution of CuIn1−xGaxS2 Nanocrystals. *J. Mater. Chem. A* **2014**, *2*, 12317−12322.

(524) Zhou, M.; Xiao, K.; Jiang, X.; Huang, H.; Lin, Z.; Yao, J.; Wu, Y. Visible-Light-Responsive Chalcogenide Photocatalyst Ba2ZnSe3: Crystal and Electronic Structure, Thermal, Optical, and Photocatalytic Activity. *Inorg. Chem.* **2016**, *55*, 12783−12790.

(525) Sathish, M.; Viswanath, R. P. Photocatalytic Generation of Hydrogen over Mesoporous CdS Nanoparticle: Effect of Particle Size, Noble Metal and Support. *Catal. Today* **2007**, *129*, 421−427.

(526) Li, C.; Yuan, J.; Han, B.; Shangguan, W. Synthesis and Photochemical Performance of Morphology-Controlled CdS Photocatalysts for Hydrogen Evolution under Visible Light. *Int. J. Hydrogen Energy* **2011**, *36*, 4271−4279.

(527) Xu, Y.; Zhao, W.; Xu, R.; Shi, Y.; Zhang, B. Synthesis of Ultrathin CdS Nanosheets as Efficient Visible-Light-Driven Water Splitting Photocatalysts for Hydrogen Evolution. *Chem. Commun.* **2013**, *49*, 9803−9805.

(528) Kudo, A.; Miseki, Y. Heterogeneous Photocatalyst Materials for Water Splitting. *Chem. Soc. Rev.* **2009**, *38*, 253−278.

(529) Karunadasa, H. I.; Montalvo, E.; Sun, Y.; Majda, M.; Long, J. R.; Chang, C. J. A Molecular MoS2 Edge Site Mimic for Catalytic Hydrogen Generation. *Science (Washington, DC, U. S.)* **2012**, *335*, 698−702.

(530) Yan, Y.; Xia, B.; Li, N.; Xu, Z.; Fisher, A.; Wang, X. Vertically Oriented MoS2 and WS2 Nanosheets Directly Grown on Carbon Cloth as Efficient and Stable 3-Dimensional Hydrogen-Evolving Cathodes. *J. Mater. Chem. A* **2015**, *3*, 131−135.

(531) Miller, E. L.; Marsen, B.; Paluselli, D.; Rocheleau, R. Optimization of Hybrid Photoelectrodes for Solar Water-Splitting. *Electrochem. Solid-State Lett.* **2005**, *8*, A247−A249.

(532) Gaillard, N.; Prasher, D.; Chong, M.; DeAngelis, A. D.; Horsley, K.; Ishii, H. A.; Bradley, J.; Varley, J. B.; Ogitsu, T. Wide-Bandgap Cu (In, Ga) S2 Photocathodes Integrated on Transparent Conductive F: SnO2 Substrates for Chalcopyrite-Based Water Splitting Tandem Devices. *ACS Appl. Energy Mater.* **2019**, *2*, 5515−5524.

(533) Iwase, A.; Ng, Y. H.; Amal, R.; Kudo, A. Solar Hydrogen Evolution Using a CuGaS2 Photocathode Improved by Incorporating Reduced Graphene Oxide. *J. Mater. Chem. A* **2015**, *3*, 8566−8570.

(534) Kaga, H.; Tsutsui, Y.; Nagane, A.; Iwase, A.; Kudo, A. An Effect of Ag (i)-Substitution at Cu Sites in CuGaS 2 on Photocatalytic and Photoelectrochemical Properties for Solar Hydrogen Evolution. *J. Mater. Chem. A* **2015**, *3*, 21815−21823.

(535) Moriya, M.; Minegishi, T.; Kumagai, H.; Katayama, M.; Kubota, J.; Domen, K. Stable Hydrogen Evolution from CdS-Modified CuGaSe2 Photoelectrode under Visible-Light Irradiation. *J. Am. Chem. Soc.* **2013**, *135*, 3733−3735.

(536) Zhang, L.; Minegishi, T.; Nakabayashi, M.; Suzuki, Y.; Seki, K.; Shibata, N.; Kubota, J.; Domen, K. Durable Hydrogen Evolution from Water Driven by Sunlight Using (Ag, Cu)GaSe2 Photocathodes Modified with CdS and CuGa3Se5. *Chem. Sci.* **2015**, *6*, 894−901.

(537) Gunawan; Septina, W.; Harada, T.; Nose, Y.; Ikeda, S. Investigation of the Electric Structures of Heterointerfaces in Pt-and In2S3-Modified CuInS2 Photocathodes Used for Sunlight-Induced Hydrogen Evolution. *ACS Appl. Mater. Interfaces* **2015**, *7*, 16086−16092.

(538) GUNAWAN, G.; Haris, A.; dri Widiyan iyan dari, H.; Septina, W.; Higeru Ikeda, S. Investigation on Stability of Electroplated-Sulfurized CuInS2-Based Photocathode Modified with an In2S3 Layer for H2 Evolution under Various PH Conditions. *Orient. J. Chem.* **2017**, *33*, 556−561.

(539) Yokogawa, T.; Taguchi, T.; Fujita, S.; Satoh, M. Intense Blue-Emission Band and the Fabrication of Blue Light Emitting Diodes in I-Doped and Ag-Ion-Implanted Cubic ZnS. *IEEE Trans. Electron Devices* **1983**, *30*, 271−277.

(540) Li, J. J.; Wang, Y. A.; Guo, W.; Keay, J. C.; Mishima, T. D.; Johnson, M. B.; Peng, X. Large-Scale Synthesis of Nearly Monodisperse CdSe/CdS Core/Shell Nanocrystals Using Air-Stable Reagents via Successive Ion Layer Adsorption and Reaction. *J. Am. Chem. Soc.* **2003**, *125*, 12567−12575.

(541) Deepak Kumar, N.; Joshi, M. P.; Friend, C. S.; Prasad, P. N.; Burzynski, R. Organic−Inorganic Heterojunction Light Emitting

Diodes Based on Poly (p-Phenylene Vinylene)/Cadmium Sulfide Thin Films. *Appl. Phys. Lett.* **1997**, *71*, 1388−1390.

(542) Kim, C.; Nguyen, T. P.; Le, Q. V.; Jeon, J.-M.; Jang, H. W.; Kim, S. Y. Performances of Liquid-Exfoliated Transition Metal Dichalcogenides as Hole Injection Layers in Organic Light-Emitting Diodes. *Adv. Funct. Mater.* **2015**, *25*, 4512−4519.

(543) Yanagi, H.; Kikuchi, M.; Kim, K.-B.; Hiramatsu, H.; Kamiya, T.; Hirano, M.; Hosono, H. Low and Small Resistance Hole-Injection Barrier for NPB Realized by Wide-Gap p-Type Degenerate Semiconductor, LaCuOSe:Mg. *Org. Electron.* **2008**, *9*, 890−894.

(544) Zakutayev, A.; Tate, J.; Platt, H. A. S.; Keszler, D. A.; Hein, C.; Mayer, T.; Klein, A.; Jaegermann, W. Electronic Properties of BaCuChF (Ch = S,Se,Te) Surfaces and BaCuSeF/ZnPc Interfaces. *J. Appl. Phys.* **2010**, *107*, 103713.

(545) Zhang, Q.; Guo, H.; Feng, Z.; Lin, L.; Zhou, J.; Lin, Z. N-ZnO Nanorods/p-CuSCN Heterojunction Light-Emitting Diodes Fabricated by Electrochemical Method. *Electrochim. Acta* **2010**, *55*, 4889−4894.

(546) Wijeyasinghe, N.; Anthopoulos, T. D. Copper(I) Thiocyanate (CuSCN) as a Hole-Transport Material for Large-Area Opto/Electronics. *Semicond. Sci. Technol.* **2015**, *30*, 104002.

(547) Ohno, T.; Kurisu, K.; Taguchi, T. Growth of High-Quality Cubic ZnS Crystals and Their Application to MIS Blue Light-Emitting Diodes. *J. Cryst. Growth* **1990**, *99*, 737−742.

(548) Dabbousi, B. O.; Rodriguez-Viejo, J.; Mikulec, F. V.; Heine, J. R.; Mattoussi, H.; Ober, R.; Jensen, K. F.; Bawendi, M. G. (CdSe) ZnS Core− Shell Quantum Dots: Synthesis and Characterization of a Size Series of Highly Luminescent Nanocrystallites. *J. Phys. Chem. B* **1997**, *101*, 9463−9475.

(549) Colvin, V. L.; Schlamp, M. C.; Alivisatos, A. P. Light-Emitting Diodes Made from Cadmium Selenide Nanocrystals and a Semiconducting Polymer. *Nature* **1994**, *370*, 354.

(550) Tanaka, T.; Kume, Y.; Nishio, M.; Guo, Q.; Ogawa, H.; Yoshida, A. Fabrication of ZnTe Light-Emitting Diodes Using Bridgman-Grown Substrates. *Jpn. J. Appl. Phys.* **2003**, *42*, L362.

(551) Miao, M. S.; Yarbro, S.; Barton, P. T.; Seshadri, R. Electron Affinities and Ionization Energies of Cu and Ag Delafossite Compounds: A Hybrid Functional Study. *Phys. Rev. B: Condens. Matter Mater. Phys.* **2014**, *89*, 045306.